FACULTY OF SCIENCE
UNIVERSITY OF COPENHAGEN

Long-distance distribution of discrete and continuous variable entanglement with atomic ensembles

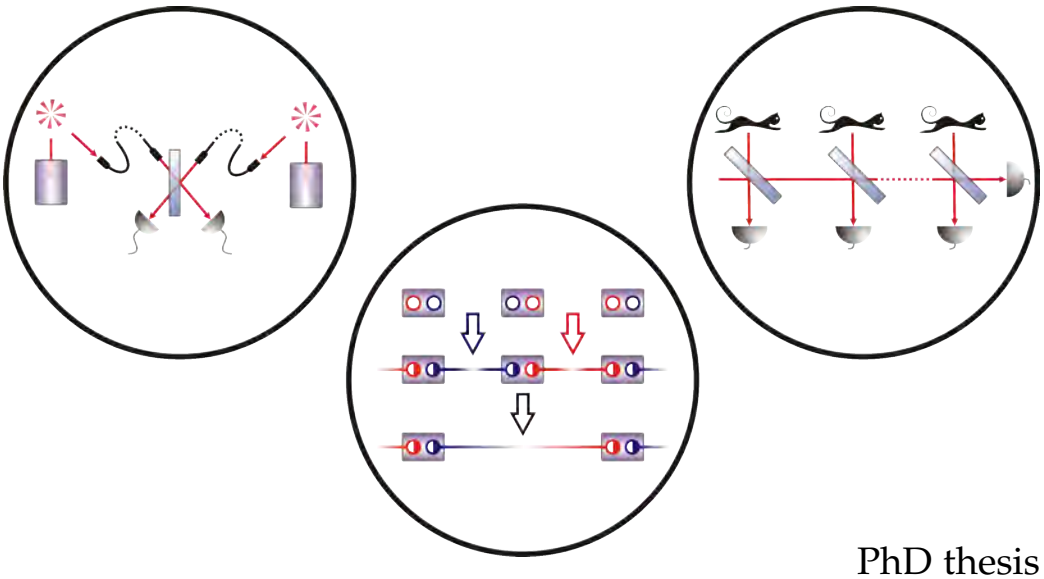

PhD thesis

Jonatan Bohr Brask

The PhD School of Science

Theoretical Quantum Optics Group
QUANTOP – Danish National Research Foundation Centre for Quantum Optics
Niels Bohr Institute

Academic supervisor: Anders S. Sørensen

April, 2010

Long-distance distribution of discrete and continuous variable entanglement with atomic ensembles

Jonatan Bohr Brask

This thesis is submitted in partial fulfilment of the requirements
for the Ph.D. degree at the University of Copenhagen.

Abstract

This thesis is concerned with the study and theoretical development of methods for generating entangled states between objects at distant locations. Entanglement is one of the most fascinating and counterintuitive phenomena in quantum physics, and a central topic in debates about the interpretation of quantum mechanics. Within the past three decades it has been realised that, in addition to being of interest for the foundations of quantum theory, entanglement can be harnessed for a variety of applications in information technology and communication, including quantum teleportation which allows quantum states to be transferred between entangled systems via exchange of only classical signals, and highly secure cryptography schemes based on quantum key distribution. There is therefore much interest in distributing entanglement between separated spatial locations.

Quantum states are fragile creatures which are easily degraded by interactions with a noisy environment. The most viable carrier of quantum states over long distances is light, because it moves fast and couples relatively weakly to its surroundings, but even light travelling e.g. in optical fibres is subject to losses which grow exponentially with distance. The associated attenuation length in standard telecom fibre is about 20km, and hence direct transmission quickly becomes unfeasible for distances of more than a few hundred kilometres. For classical communication this problem is solved by amplification, but for quantum signals the so-called no-cloning theorem, which stipulates that an unknown quantum state cannot be copied, implies that noiseless amplification is impossible. Instead, the problem can be solved by a more involved approach based on first generating entanglement over short distances and then "swapping" the entanglement to longer distances via quantum teleportation. Schemes which implement this approach are known as quantum repeaters.

Here we describe three studies of quantum repeater protocols. First, we develop a detailed analysis of how memory imperfections affect the performance of quantum repeaters based on atomic-ensemble quantum memories in a simple architecture. Next, we develop two new proposals for quantum repeater schemes with the aim of achieving higher communication rates by improving the success probability of entanglement swapping. The first scheme, like a number of pre-

vious proposals, is based on discrete entanglement in the form of spin-waves in atomic ensembles generated by Raman scattering. However, unlike previous proposals it allows multiple spin-waves to be stored within a single atomic ensemble. This makes it possible to perform entanglement swapping without having to retrieve the spin-waves. Instead, swapping is performed by means of fluorescence measurement of atomic level populations, which can have very high efficiencies. The second scheme employs a different type of entangled states known as coherent state superpositions, or 'Schrödinger cat states'. Basing the repeater on such states makes it possible to perform entanglement swapping by means of homodyne detection of light, which with current technology is significantly more efficient than the single-photon counting required in protocols based on discrete entanglement. Generating cat states however is non-trivial, and we device a protocol for growing them from entangled states of delocalised single photons. We also demonstrate that near-deterministic entanglement swapping can be implemented for the cat states with only linear optics and homodyne measurements.

Dansk resumé

Denne Ph.D. afhandling omhandler metoder med hvilke objekter, som befinder sig langt fra hinanden, kan bringes i en ikke-separabel (også kaldet 'sammenfiltret') kvantetilstand. Ikke-separabilitet er et fascinerende kvantefysisk fænomen, som strider overraskende imod intuition fra hverdagserfaringer og spiller en central rolle i fortolkninger af kvantemekanikken. Indenfor de seneste 30 år er det blevet klart at ikke-separabilitet, udover at være af fundamental vigtighed for kvantemekanikken som teori, også kan finde anvendelse indenfor en række nye informations- og kommunikationsteknologier, bl.a. kvanteteleportation – som tillader overførsel af kvantetilstande mellem adskilte systemer i en ikke-separabel tilstand uden udveksling af nogen form for kvantefysisk signal – og ubrydelige krypteringsprotokoller hvis sikkerhed er baseret på grundlæggende naturlove.

Kvantetilstande er skrøbelige størrelser, som nemt kan ødelægges ved vekselvirkninger med andre systemer. Den bedste og mest oplagte måde at transportere kvantetilstande på er via lys, fordi lyset bevæger sig hurtigt og vekselvirker relativt svagt med omgivelserne, men selv lys som f.eks. løber igennem en optisk fiber vil efterhånden blive absorberet eller spredes og dermed gå tabt. Tabet stiger eksponentielt med fiberens længde. Absorptionslængden i moderne telekommunikationsfibre er ca. 20km, og for afstande over 100km bliver tabet derfor hurtigt en uoverstigelig barriere. For klassiske signaler kan tab modvirkes ved at forstærke lyspulserne med jævne mellemrum, men for kvantesignaler umuliggøres en sådan forstærkning af det kvantemekaniske kloningsforbud, ifølge hvilket det er umuligt at kopiere en vilkårligt given kvantetilstand. Problemet kan i stedet løses v.h.a. en struktur, kaldet et "kvanterelæ", hvor ikke-separable tilstande først skabes over kortere afstande og derefter forbindes via kvanteteleportation.

I denne afhandling beskrives tre studier af kvanterelæer. Vi præsenterer først en detaljeret analyse af, hvilken indflydelse imperfektioner i kvantehukommelser baseret på atomare hukommelser har i et kvanterelæ med en simpel arkitektur. Derefter udvikler vi to nye kvanterelæer med det formål at opnå en højere kommunikationsrate ved at øge sandsynligheden for succesfuld kvanteteleportation. Den første protokol er, i lighed med flere tidligere protokoller, baseret

på diskret ikke-separabilitet i form af spin-bølger i atomare ensembler skabt via Ramanspredning, men i modsætning til tidligere protokoller lagres flere spin-bølger i det samme ensemble. Dette gør det muligt at implementere teleportation v.h.a. fluorescensmålinger, som kan have høj effektivitet. Den anden protokol er baseret på en anden type ikke-separable tilstande kaldet "Schrödinger-kat-tilstande". Ved at basere protokollen på denne type tilstande bliver det muligt at implementere teleportation v.h.a. homodyn detektion, der med nuværende teknologi har betydeligt højere effektivitet end enkeltfotondetektorer, som benyttes i protokoller baseret på diskret ikke-separabilitet. Det er imidlertid ikke trivielt at skabe kat-tilstande, og vi udvikler en metode, der gør det muligt at opdyrke dem fra ikke-separable enkelt-foton tilstande. Vi viser også, at nærdeterministisk kvanteteleportation for kat-tilstandene kan implementeres udelukkende v.h.a. lineær optik of homodyn detektion.

Acknowledgments

This thesis concludes three years (plus epsilon!) of ph.d. studies carried out at the Danish National Research Foundation Centre for Quantum Optics (QUANTOP) at the Niels Bohr Institute, University of Copenhagen. It has been three enjoyable years in a highly international environment and with many travels abroad – both for research and personal reasons. Naturally many people have contributed to fill this time with pleasant and memorable experiences.

First of all, I would like to thank my supervisor Prof. Anders S. Sørensen. I started working under Anders' guidance already during my master project and continued into the ph.d. During these years he has been very generous with his time, always keeping an open door, ready to talk physics. This informal attitude has been a great benefit for me. I have also had helpful discussions with other past and present QUANTOP members and visitors, in particular Martijn Wubs, Dirk Witthaut, Eran Kot, and Christine Muschik. Jörg Helge Müller has enlightened me on many issues concerning laboratory experiments. Reaching a bit further back in time, my first encounter with quantum mechanics as an undergraduate student brought me into contact with Ole Ulfbeck. I owe a good part of my interest in 'quantum stuff' to captivating discussions with him, and also with Aage Bohr, on the counter-intuitive nature of quantum mechanics and their efforts to resolve its apparent paradoxes.

During my time in QUANTOP, there has always been a very warm and inclusive atmosphere and a truly international constellation of people. There is good interaction between the experimental group, headed by Centre leader Prof. Eugene S. Polzik, and the theory branches, both research-wise and socially. The members of the new theory group of Prof. Michael Wolf who joined the Centre halfway through my project have all added to this pleasant environment. My thanks go to everyone in the group for contributing to a great working environment as well as numerous outings, social events, and abundant cake at coffee breaks!

Almost six months of my studies were spent as a visitor in the group of Prof. Mikhail D. Lukin at Harvard University, USA – a visit that I very much enjoyed – and I would like to thank Misha for giving me the opportunity to experience research across the Atlantic, as well as for his ingenious input to the project I

worked on there. At Harvard it was a pleasure to work with Liang Jiang and Alexey Gorshkov, who were not only my inspiring collaborators and mentors but also great hosts, welcoming me both in the research group and into their social lives. My visit certainly wouldn't have been the same without our regular 1 am discussions in their office! I also wish to acknowledge good discussions with Sebastian Hofferberth and Sofia Magkiriadou on experimental implementations of our ideas.

Finally, I extend my warmest thanks to my family and friends for all the good times I have shared with them these past years, both at home and abroad. In particular, I am grateful to Ana Olenina for hosting me when I first arrived at Harvard, and to everyone in Regensen for welcoming me back to a wonderfully lively and inspiring base.

List of publications

The main results presented in this thesis have been published in the following papers (one of which is in review at *Physical Review Letters*):

- J. B. Brask and A. S. Sørensen, "Memory imperfections in atomic-ensemble-based quantum repeaters", *Physical Review A* **78**, 012350 (2008).
- J. B. Brask, L. Jiang, A. V. Gorshkov, V. Vuletic, A. S. Sørensen, and M. D. Lukin, "Fast Entanglement Distribution with Atomic Ensembles and Fluorescent Detection", *Physical Review A* **81**, 020303(R) (2010).
- J. B. Brask, I. Rigas, E. S. Polzik, U. L. Andersen, and A. S. Sørensen, "A Hybrid Long-Distance Entanglement Distribution Protocol", *arXiv* **quant-ph**, 1004.0083 (2010).

I have also presented the results at the following conferences, meetings and schools:

- QIPC 2009, International Conference on Quantum Information Processing and Communication, Rome, Italy, September 2009 (talk).
- Atomic Physics Gordon Conference, Tilton, NH, USA, June 2009 (poster).
- Condensed Matter Theory (CMT) Kids' Seminar, Harvard University, Cambridge, MA, USA, February 2009 (talk).
- Quantum and Non-Linear Optics (Q&NLO) Summer School, Hven, Sweden, August 2008 (poster).
- EYSCQI, First European Young Scientists' Conference on Quantum Information, Vienna, Austria, August 2007 (poster).
- QUROPE Winter School, Obergurgl, Austria, February 2007 (poster).

Contents

Chapter 1

Introduction

Entanglement is one of the most curious and surprising phenomena of quantum physics – often popularized but hard to grasp, its history as a topic of research and controversy goes back almost to the founding years of quantum mechanics itself at the beginning of the 20th century. The word was first introduced by Erwin Schrödinger (in its german form "Verschränkung") in a 1935 response [116] to a now-famous paper by Einstein, Podolsky and Rosen (EPR), published earlier the same year, where it was argued that quantum mechanics must be an incomplete theory [42]. Einstein and his co-authors had observed that quantum mechanics allows for a peculiar type of states in which two non-interacting objects are correlated in such a manner that, following a measurement on one of them, the outcome of a similar measurement on the other can be predicted with certainty. Such a correlation in itself is nothing paradoxical – think for example of the colour of socks[1]. Observing the colour of a person's left sock and knowing the conventions of clothing, we can predict with a high degree of certainty the colour of the right sock[2]. What EPR found was that the correlations hold even for quantities such as position $\hat{X}$ and momentum $\hat{P}$ which do not commute. In quantum mechanics noncommutative quantities must obey the Heisenberg uncertainty principle which stipulates that they cannot be simultaneously known with arbitrary precision. But in an EPR state, a measurement of either $\hat{X}$ or $\hat{P}$ on one particle allows one to predict the outcome of a similar measurement on the other particle. For particles that do not interact, EPR assumed that a measurement on one cannot change the state of the other and they concluded that the second particle must posses simultaneous values of $\hat{X}$ and $\hat{P}$. Since quantum mechanics does not allow assignment of such values, they argued that the theory must be incomplete and should be replaced by a more fundamental, underlying theory.

The original paper of EPR did not offer any obvious way to test this claim, since the underlying 'hidden variable theory' had to reproduce the correlations of the

[1] as suggested by John Bell in his excellent essay "Bertlmanns' socks and the nature of reality" [5].

[2] In Bell's essay, Bertlmann always wears socks of different colour and the observer is assumed to know this. Here we consider someone with a less peculiar dresscode!

quantum theory, but in 1964 this picture was changed in a seminal paper by Bell [6]. He showed that a hidden variable theory which precludes any direct influence of distant systems on each other (a 'local' theory) can never reproduce the quantum correlations for all possible settings of the measurement apparatus. The correlations of the hidden variable theory are restricted by what is now know as Bell's inequality. This spurred groundbreaking experiments in the 1970s and 80s, testing Bell's inequalities with both radiation from positronium annihilation and with protons, but mainly with entangled photons of visible light [2, 34, 99]. The experiments provided strong evidence for the validity of quantum mechanics, and the results were further corroborated by experiments in the 90s [132, 137]. As it turns out, these experiments were also precursors to emerging communication technologies.

In the 1980s and 90s several discoveries led to the realisation that the departure of quantum mechanics from classical physics opens up new possibilities in information processing and communication. These discoveries marked the birth of quantum computing, quantum communication and quantum information theory as new research fields. In the paradigm of these fields, in addition to being a distinguishing feature of quantum physics with philosophical implications for our understanding of nature, entanglement can be viewed as a powerful resource for information technology.

One direction of thought, pioneered by Landauer and others, emphasised the physical nature of computation. In the words of Richard Feynman, speaking on simulations: "[...] I'm not happy with all the analyses that go with just the classical theory, because nature isn't classical, dammit, and if you want to make a simulation of nature, you'd better make it quantum mechanical, and by golly it's a wonderful problem, because it doesn't look so easy. Thank you." [46]. It is common to distinguish between problems which can be solved using an amount of time and resources which scales as a polynomial in the size of the input, and problems which require superpolynomial time or resources. The first kind of problems are considered 'easy' or tractible whereas the other kind is considered 'hard' or intractible. Simulating quantum systems on classical computers is hard, because the dimension of the state space of such systems grows exponentially with the particle number. For example, just writing down a general state of N electrons requires 2^N complex numbers, which for $N = 300$ far exceeds the number of neurons in the human brain or even the estimated number of atoms in the observable universe. On the other hand, if the bits in the classical computer are replaced by two-level systems which themselves behave according to the laws of quantum mechanics, then the state of the electrons can be represented by just N of these quantum bits or 'qubits'. In 1982, Feynman conjectured that quantum computers based on qubits can efficiently simulate general quantum systems with local interactions. His conjecture was proved true by Lloyd in 1996 [81].

Related ideas more directly connected to computer science lead to the discovery of quantum algorithms which solve certain tasks qualitatively faster than any known classical algorithm [59, 118]. In particular Shor showed in 1994 that factorisation of a large number into its prime factors can be done in polynomial

time on a quantum computer [118]. The same problem is widely believed to be intractible on a classical computer, and Shor's discovery had some startling implications because the security of certain cryptosystems is based on this belief. The commonly used RSA cryptography scheme relies on the idea that given a product of two large primes, e.g. 1777×1801, if one of the factors is known the other can be quickly determined by simple division, but if none of the factors are known it is much more difficult to find them. Shor had proven that the last part is actually not true, if one has access to a quantum computer. At the same time, despite much effort, no definite proof has yet been obtained for the classical intractibility of factorisation, and Shor's discovery cast some doubt on whether such a proof exists.

Other cryptosystems in use today rely on similar unproven assumptions, and hence a breakthrough in mathematics or computer science could potentially render them useless [53]. In a third development it was found that quantum communication – communication based on the exchange of signals described by quantum states – offers a solution to this problem. In quantum mechanics, a measurement always perturbs the state of the system and hence an eavesdropper listening in on a secret signal can be detected. In addition, an eavesdropper cannot duplicate the signal because it follows from the laws of quantum mechanics that it is impossible to make a perfect copy of an unkown quantum state – the so-called 'no-cloning theorem' [39, 139]. These peculiar properties of quantum states can be harnessed to design cryptography protocols whose security rely not on assumptions about the computation power and degree of mathematical sofistication available to attackers but instead on our assumptions about the physical laws of nature. Roughly speaking, if the quantum description of nature holds – and there is strong experimental evidence that it does – then the security of quantum cryptography is guaranteed. Quantum cryptography schemes were proposed by Bennett and Brassard in 1984 [7] and by Ekert in 1991 [44]. The Ekert scheme relies directly on Bell's inequality to assert the security of the protocol, and thus a line can be drawn from the fundamental, philosophically motivated discussion in the EPR paper to the application of quantum theory in cutting-edge emerging technology. An excellent review of quantum cryptography can be found in Ref. [53]. Another notable discovery in the field of quantum communication came in 1993 and was dubbed 'quantum teleportation' [8]. If a pair of qubits share an entangled state, then an arbitrary state of a third qubit can be transferred from the location of the first qubit to the location of the second without the need for any quantum signal to be exchanged. This means that the general problem of quantum communication can be reduced to local operations and distribution of entangled states.

The discoveries in quantum information science spurred intensive effort to implement the ideas in practice and they still provide a driving force behind many current experiments in areas such as quantum optics, atomic physics, quantum electrodynamics, and solid state physics. In particular, much work is directed toward the goal of establishing entangled states over long distances. This will enable quantum cryptography and transfer of quantum states and will also allow tests of Bell's inequality on a larger scale, which may make it possible to close loopholes in previous experiments which ment that certain types of hidden-

variable theories could not be completely ruled out.

Entanglement can only be produced locally, and hence transmission of quantum states is necessary to distribute it to distant locations. Light is an ideal (in fact the only really viable) carrier of quantum states because it travels fast and interacts weakly with its surroundings, thus protecting the states from noise. However, distribution of entanglement by direct transmission cannot be scaled to arbitrarily large distances. Transmission losses for light travelling e.g. in optical fibres increase exponentially with distance and hence the time needed to distribute entanglement grows exponentially as well. A typical fibre attenuation legth at standard telecommunications wavelengths is about 20 km, which at a distance of 1000 km corresponds to a drop in transmission by a factor 10^{-22}. If we can produce entangled photons at a rate of 1 GHz (which is ambitious), this means we can expect to establish one entangled pair every 160,000 years! For classical communication, the problem can be solved by introducing repeater stations at regular intervals along the fibre which amplify the signal and remove noise. However for quantum signals such an approach is hampered by some of the very same physical laws that give quantum information its power: it follows from the no-cloning theorem that noiseless amplification is impossible for general quantum states. A different solution is therefore needed. It turns out scalable transmission can be achieved by an approach based on entanglement and teleportation. The communication channel is first divided into segments short enough for entanglement to be established directly. Given two adjacent entangled pairs, one end of the first pair can then be teleported to the far end of the second pair, effectively creating an entangled pair over twice the distance. This generalisation of teleportation to entangled input states is known as 'entanglement swapping' [146]. By iterating this swapping, doubling the distance every time, entanglement can be established across long channels and, crucially, this can be done at a rate which scales polynomially with the channel length and with polynomial resources. Such an approach is thus much more efficient than direct transmission at large distances. The construction was dubbed a 'quantum repeater' when first proposed by Briegel *et al.* who saw an analogy between the nodes of entangled pairs in their protocol and the repeater stations used in classical signal relay [19].

An essential requirement for the implementation of a quantum repeater is that the entangled states at each level of iteration can be stored. If the states cannot be stored, entanglement generation in two neighbouring segments has to succeed simultaneously for entanglement swapping to be possible. This applies at every level of iteration and hence the only way to create a final entangled pair is for all entanglement generation attemps to succeed simultaneously, but the probability for this to happen decreases exponentially with the number of segments. On the other hand, if entanglement in a segment can be stored while generation in the neighbouring segment is attempted then there is no requirement for simultaneity. A quantum repeater thus relies on memories for quantum states.

Other requirements include the ability to generate entanglement in the basic segments in a heralded fashion, and the ability to perform entanglement swapping. Deterministic entanglement swapping for qubits relies on a joint, projective mea-

surement of two qubits onto a basis of entangled states (a Bell measurement), which is a challenging task because it requires implementation of a controlled two-qubit gate – a major hurdle for quantum computation in general. In addition, to achieve entanglement distribution at arbitrary distances, the original proposal by Briegel *et al.* included a purification step nested with the entanglement swapping. Purification allows distillation of a few entangled pairs of high purity from a supply of lower-purity pairs and is necessary to counteract the decoherence introduced by imperfect operations during entanglement generation and swapping, which otherwise limits the distance over which entanglement can be distributed. Experimentally, the original protocol is rather difficult to realise because it requires implementation of Bell measurements and because of the significant resource overhead associated with purification. However, when distances are not too large it is possible to device a 'scaled-down' protocol which relies on only partial Bell-measurements, that succeed with non-unit probability, and omits the purification step in exchange for greatly relaxed experimental requirements.

In 2001, Duan, Lukin, Cirac and Zoller (DLCZ) published a seminal proposal for such a protocol based on atomic ensemble memories, linear optics and single-photon detection [41]. They found a simple way to entangle two spatially separated ensembles via Raman scattering and by making use of collectively enhanced coupling to light, they showed that the entanglement can efficiently be swapped to larger distances. The relatively simple ingredients of the DLCZ protocol makes it attractive from a practical point of view, and it has recieved a lot of attention in recent years, both experimentally and theoretically. Methods for trapping and controlling atomic ensembles in the laboratory are well established, and there has been impressive progress towards the implementation of entanglement generation and swapping, e.g. with the experiments [25, 30, 31, 43, 45, 77, 131, 133, 142] and [26, 78, 143]. At the same time, it has been realised that, although sub-exponential, the rate scaling of DLCZ is not good enough to allow a practical implementation over distances that cannot be reached by direct transmission, and multiple proposals for improved protocols inspired by DLCZ and based on similar ingredients have been published [13, 27, 72, 113, 114, 119, 145]. A recent review of this field of research can be found in Ref. [111]. The work described in this thesis is all to some degree related to and inspired by the DLCZ protocol. It falls in three parts, each of which concern quantum repeaters that can be implemented with atomic ensembles and linear optics.

The first part is an investigation of the impact of quantum memory imperfections on a protocol which can be seen as a generalised version of the DLCZ scheme. We develop an implementation-independent description of the memories in terms of harmonic oscillator modes and find the scaling of memory-induced errors in terms of the parameters of this model. Our results apply to memories governed by an interaction Hamiltonian quadratic in the mode operators, which includes most atomic ensemble memories. The initial motivation for this work was to see whether the DLCZ scheme could be implemented with a particular ensemble-based memory demonstrated in a 2004 experiment in Copenhagen [74]. We use our model to test this.

In the second part we present a new atomic-ensemble-based repeater protocol. Entanglement distribution rates for both the DLCZ scheme and later improved variants are limited by the low efficiency of single-photon detectors which are employed in the entanglement swapping operations. The new protocol aims to increase the efficiency of entanglement swapping by replacing detection of single photons by fluorescence measurements, in which the detected signal consists of many photons and which can be very efficient. The basic entanglement generation scheme of the DLCZ protocol is retained, but the need for retrieval of atomic excitations onto light is eliminated by storing multiple excitations in the same ensemble.

In the third part we move a bit further away from DLCZ and into the realm of continuous variables. It is common to identify two regimes for quantum information, known as 'discrete' and 'continuous' [18, 76]. By a classical analogue the first can be thought of as digital and the second as analog. In the discrete variable regime, systems are described in terms of qubits living in finite dimensions. E.g. for light in this regime, single photons are the carriers of information with qubits encoded in polarisation, frequency or spatial degrees of freedom, and measurements are performed by single-photon detection. In the continuous variable regime, information is encoded in continuous degrees of freedom which live in infinite dimensions, such as position and momentum as in the EPR argument. For light, the quantities corresponding to position and momentum operators are the quadratures of the electromagnetic field, which are measured via homodyne detection. Both regimes have advantages and drawbacks. On the one hand, single photons are good for heralding events across lossy channels since their discrete nature implies that no partial loss can take place. Either the photon makes it through the channel or it doesn't. Entanglement generation in the DLCZ protocol is based on this. On the other hand, certain tasks can be accomplished unconditionally with linear optics in the continuous regime while not in the discrete one. For example, deterministic teleportation, which for qubits requires the implementation of a Bell measurement, can be implemented with a simple beam splitter and homodyne detectors (using in fact the exact same entangled state as in the EPR paper) [17]. In addition, with present technology homodyne measurements can be implemented with much higher efficiency than single-photon detection. Motivated by these considerations we device a repeater which combines discrete variable entanglement generation as in the DLCZ protocol with entanglement swapping based on homodyning, in an attempt to take advantage of the best of two worlds.

The three main parts of the thesis outlined above are presented in Chap. 3, 4, and 5. In Chap. 2 we recall some fundamental concepts from quantum mechanics, establish our notation, and introduce some basic features common to the different repeaters systems of the thesis. In Chap. 6 we conclude and discuss future directions of research.

Chapter 2

Fundamentals

In this chapter we will first recall some essential concepts and tools from quantum mechanics relevant to subsequent parts of the thesis. We then go on to introduce the basics of quantum repeaters, in particular repeaters based on atomic ensembles.

We are mostly concerned with the quantum states of light and atoms and though these physical systems have distinct properties, in much of what we will do it is possible and convenient to describe them in a common mathematical framework. Light is naturally described in terms of harmonic oscillators and, under suitable conditions, atomic ensembles fit into a similar description. Hence, our point of departure is the quantum mechanics of harmonic oscillators

2.1 The quantum harmonic oscillator

When describing light and atomic ensembles in terms of harmonic oscillators, the concept of modes is integral. A mode refers to a single degree of freedom of the electromagnetic field or atomic system, e.g. polarisation, frequency, atomic level, spin-wave, or spatial and temporal degrees of freedom. Each mode is described by an independent harmonic oscillator.

In quantum mechanics, a harmonic oscillator is described by the Hamiltonian

$$\hat{H} = \hbar\omega(\frac{1}{2} + \hat{a}^\dagger\hat{a}), \tag{2.1}$$

where $\hat{a}^\dagger$ and $\hat{a}$ are creation and annihilation operators which raise and lower the energy in quanta of $\hbar\omega$. Collectively we refer to them as ladder or mode operators. They obey the canonical commutator relation

$$[\hat{a}, \hat{a}^\dagger] = 1. \tag{2.2}$$

For a many-mode system we label the mode operators by an index $\hat{a}_i$, and operators acting on different modes commute

$$[\hat{a}_i, \hat{a}_j^\dagger] = \delta_{ij}, \qquad [\hat{a}_i, \hat{a}_j] = 0. \tag{2.3}$$

Modes can also be labelled by a continuous index such as a wave vector $\mathbf{k}$. The Kronecker delta in the commutator is then replaced by a Dirac delta function. Alternatively, a discrete set of modes can be constructed by introducing a complete set of orthonormal mode functions $u_i(\mathbf{k})$ and defining $\hat{a}_i = \int d\mathbf{k}\, u_i^*(\mathbf{k})\hat{a}(\mathbf{k})$ [61].

It is often useful to express operators on the system (e.g. the Hamiltonian above) in terms of ladder operators. Sometimes however, it is more convenient to work with the quadratures of the quantum harmonic oscillator. These are the analogues of the sine and cosine parts of the classical electromagnetic field or the position and momentum of the classical oscillator. Unlike the ladder operators, the quadrature operators are Hermitian and can be measured. In this thesis, they are defined by

$$\hat{X} = \frac{1}{\sqrt{2}}(\hat{a}^\dagger + \hat{a}), \qquad \hat{P} = \frac{i}{\sqrt{2}}(\hat{a}^\dagger - \hat{a}), \tag{2.4}$$

where we have chosen the normalisation such that their canonical commutator becomes

$$[\hat{X}, \hat{P}] = i. \tag{2.5}$$

The Hamiltonian can be expressed in terms of the quadratures as

$$\hat{H} = \frac{\hbar\omega}{2}(\hat{X}^2 + \hat{P}^2). \tag{2.6}$$

Since the quadrature operators do not commute, they are incompatible observables which cannot be jointly measured and they must obey the Heisenberg uncertainty relation. For an arbitrary state of the system ([52] p. 150)

$$\langle(\Delta\hat{X})^2\rangle\langle(\Delta\hat{P})^2\rangle \geq \frac{1}{4}|\langle[\hat{X}, \hat{P}]\rangle|^2 = \frac{1}{4}, \tag{2.7}$$

where $\langle(\Delta\hat{X})^2\rangle$ and $\langle(\Delta\hat{P})^2\rangle$ denote the variances of the operators.

2.1.1 Harmonic oscillator states

Fock states

The infinite Hilbert space corresponding to (2.1) is naturally described in the basis of number states, also called Fock states. These are energy eigenstates labelled by an integer n which fulfil

$$\hat{a}^\dagger\hat{a}|n\rangle = n|n\rangle, \tag{2.8}$$

and they are orthonormal $\langle n|m\rangle = \delta_{nm}$. When the harmonic oscillator describes an electromagnetic (light) field, $|n\rangle$ represents a state of the field with exactly n photons. The creation and annihilation operators create and destroy photons respectively

$$\hat{a}^\dagger|n\rangle = \sqrt{n+1}|n+1\rangle \tag{2.9}$$

$$\hat{a}|n\rangle = \sqrt{n}|n-1\rangle. \tag{2.10}$$

This is the reason for the term 'ladder operators'. The state $|0\rangle$ is the state of minimal energy, i.e. the ground state, of the quantum harmonic oscillator. It is known as the vacuum state, since it describes a vacuum of the electromagnetic field, and is also written as $|vac\rangle$. When working with multi-mode systems, the notation $|vac\rangle$ is often reserved to mean the collective vacuum for all the modes. That is, $|vac\rangle = |0\rangle_1 \otimes |0\rangle_2 \otimes \cdots$. Any Fock state can be constructed by repeatedly acting on $|vac\rangle$ with $\hat{a}^\dagger$

$$|n\rangle = \frac{1}{\sqrt{n}}(\hat{a}^\dagger)^2|vac\rangle. \tag{2.11}$$

In addition to Fock states, other important classes of states which we shall encounter include coherent states, squeezed states and Schrödinger cat states.

Coherent states

The uncertainty relation between $\hat{X}$ and $\hat{P}$ implies that in contrast to the classical case, a state of the quantum harmonic oscillator can never be a simple point in phase space. It always acquires some spread, to fulfil (2.7). The set of states that come closest to being phase space points are called the coherent states. These are the unique states of minimal uncertainty, in the sense that they equalise (2.7), with equal uncertainties in $\hat{X}$ and $\hat{P}$. Formally the coherent states can be labelled by a complex number α and are the right eigenstates of the annihilation operator

$$\hat{a}|\alpha\rangle = \alpha|\alpha\rangle. \tag{2.12}$$

Like the Fock states, the set of coherent states span the entire Hilbert space. However, unlike the Fock states the coherent states are not orthogonal, the overlap of two coherent states being ([52] p. 53)

$$\langle\alpha|\beta\rangle = e^{(\alpha\beta^* - \alpha^*\beta)/2}e^{-|\alpha-\beta|^2/2} = e^{i\,\mathrm{Im}(\alpha\beta^*)}e^{-|\alpha-\beta|^2/2}, \tag{2.13}$$

and they thus form an overcomplete basis. The expectation values of the quadrature operators in a coherent state are

$$\langle\alpha|\hat{X}|\alpha\rangle = \sqrt{2}\,\mathrm{Re}(\alpha), \qquad \langle\alpha|\hat{P}|\alpha\rangle = \sqrt{2}\,\mathrm{Im}(\alpha), \tag{2.14}$$

and the expectation value of the number operator is $\langle\alpha|\hat{a}^\dagger\hat{a}|\alpha\rangle = |\alpha|^2$. That is, for an electromagnetic field, $|\alpha|^2$ is the mean photon number in the coherent state. When the mean photon number becomes very large, the fixed uncertainties of $\hat{X}$ and $\hat{P}$ become negligible compared to the displacement from the origin of phase space given by (2.14), and the coherent state behaves like a classical phase space point. In the opposite limit, the coherent states and the Fock states coincide

$$|\alpha = 0\rangle = |n = 0\rangle = |vac\rangle. \tag{2.15}$$

All coherent states have the same phase space uncertainties as the vacuum, but non-zero mean values of the quadratures according to (2.14). They can therefore be described as vacuum states displaced from the origin of phase space

$$|\alpha\rangle = \hat{D}(\alpha)|vac\rangle, \tag{2.16}$$

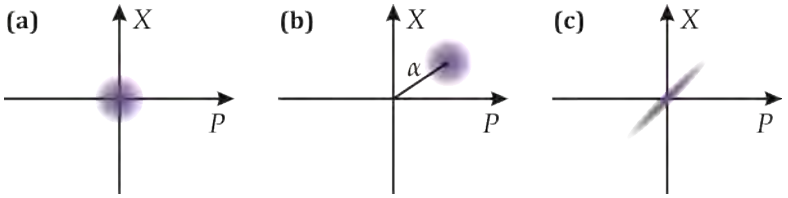

FIGURE 2.1: Schematic depiction of states in phase space. **(a)** Vacuum state. **(b)** Coherent state. **(c)** Squeezed vacuum state.

where $\hat{D}(\alpha)$ is the displacement operator, defined by

$$\hat{D}(\alpha) = \exp\left(\alpha^* \hat{a} + \alpha \hat{a}^\dagger\right) = \exp\left(\sqrt{2}\,\mathrm{Re}(\alpha)\hat{X} + \sqrt{2}\,\mathrm{Im}(\alpha)\hat{P}\right). \tag{2.17}$$

Coherent states provide a very good description of the output from lasers, which emit coherent, monochromatic light fields [52, 55].

Squeezed states

Another important class of states are the squeezed vacuum states $\hat{S}(\xi)|vac\rangle$, where the single-mode squeezing operator is

$$\hat{S}(\xi) = \exp\left(\frac{1}{2}\xi^* \hat{a}^2 - \frac{1}{2}\xi \hat{a}^{\dagger 2}\right). \tag{2.18}$$

Such states can be produced e.g. by degenerate parametric down conversion in a non-linear crystal where photons from a pump field are converted into pairs of identical photons of lower energy. They are squeezed in the sense that the uncertainty in one of their quadratures is below that of the vacuum state. For $\xi = re^{i\theta}$, the direction of squeezing in phase space is determined by θ and the amount by r. The largest suppression is found for the rotated quadrature $\cos(\theta/2)\hat{X} + \sin(\theta/2)\hat{P}$. In particular, for $\theta = 0$ the squeezing is strongest along $\hat{X}$ and we have

$$\langle(\Delta\hat{X})^2\rangle = \frac{1}{2}e^{-2r}, \qquad \langle(\Delta\hat{P})^2\rangle = \frac{1}{2}e^{+2r}. \tag{2.19}$$

The conjugate variable $\hat{P}$ is anti-squeezed since the Heisenberg uncertainty relation (2.7) must hold. A schematic depiction of the spread in phase space of a vacuum state, a coherent state, and a squeezed state is shown in Fig. 2.1.

In the remainder of this thesis we will only need to consider squeezing along the axes of phase space, which means that $\xi = r$ is real. In addition, although it is customary in text books and elsewhere [4, 52, 97] to express squeezing in terms of the parameter r, it will sometimes be more convenient to refer to the factor $s = e^{2r}$ by which the variance of the quadratures is squeezed. We therefore introduce the notation

$$\hat{S}(s) = \hat{S}(r). \tag{2.20}$$

In the experimental literature, squeezing is often measured in units of dB, defined as $10\log_{10}(s)$. A reduction in the variance by a factor of 2 corresponds

to about 3 dB of squeezing. States of light with squeezing up to 6 dB are routinely produced in today's labs, but squeezing much beyond 10 dB is difficult to obtain at present, the best reported numbers being in the range of 10-11.5 dB [40, 87, 128]. For squeezing of collective spin in atomic ensembles, the state of the art is 3-6 dB [1, 80, 127, 130].

Two-mode squeezed states

Two-mode squeezed states can be created by degenerate parametric down conversion where pump photons in a non-linear crystal are converted into pairs of photons with different frequencies or polarisations. Formally, two-mode squeezing is generated by the operator

$$\hat{\mathcal{S}}_{12}(\xi) = \exp\left(\xi^* \hat{a}_1 \hat{a}_2 - \xi \hat{a}_1^\dagger \hat{a}_2^\dagger\right) \tag{2.21}$$

where $\hat{a}_1$, $\hat{a}_2$ are the mode operators for the two modes. Acting on the vacuum, this operator generates a two-mode squeezed vacuum state $\hat{\mathcal{S}}_{12}(\xi)|vac\rangle$. What is squeezed by $\hat{\mathcal{S}}_{12}(\xi)$ are the sum and difference modes $\hat{a}_\pm = (a_1 \pm \hat{a}_2)/\sqrt{2}$. For $\xi = re^{i\theta}$, the squeezing is strongest along the rotated quadratures $\cos(\theta/2)\hat{X}_\pm + \sin(\theta/2)\hat{P}_\pm$. In particular, for $\theta = 0$ one has

$$\langle(\Delta\hat{X}_+)^2\rangle = \langle(\Delta\hat{P}_-)^2\rangle = \frac{1}{2}e^{-2r}, \tag{2.22}$$

$$\langle(\Delta\hat{P}_+)^2\rangle = \langle(\Delta\hat{X}_-)^2\rangle = \frac{1}{2}e^{+2r}, \tag{2.23}$$

in analogy with the single-mode case above. As in the single-mode case, we will use the notation $\hat{S}_{12}(s) = \hat{\mathcal{S}}_{12}(r)$ for $s = e^{2r}$. The operator $\hat{\mathcal{S}}_{12}(\xi)$ cannot be separated into a product of single-mode operators for the modes 1 and 2. However, it can be separated into single-mode squeezing of the superpositions modes ([4] p. 78)

$$\hat{\mathcal{S}}_{12}(\xi) = \hat{\mathcal{S}}_+(\xi)\hat{\mathcal{S}}_-(-\xi). \tag{2.24}$$

In the limit of infinite squeezing, the variances of $\hat{X}_+$ and $\hat{P}_-$ vanish and hence $\hat{X}_1 + \hat{X}_2 = x_0$ and $\hat{P}_1 - \hat{P}_2 = p_0$ for some fixed values x_0 and p_0. As mentioned in Chap. 1, such perfect (anti)correlation of position and momentum variables was used in the celebrated argument against the completeness of quantum mechanics by Einstein, Podolsky and Rosen [42]. For this reason two-mode squeezed vacuum states are also known as EPR states.

Schrödinger cat states

In Schrödinger's famous gedankenexperiment a cat is trapped in a box together with a device which will instantly kill the creature conditioned on the decay of an unstable atom [116]. Since the atom is a quantum mechanical system, prior to any measurement (such as opening the box) it exists in a superposition of being excited or having decayed. Consequentially the cat must be in a superposition of dead or alive. The cat here serves to emphasise the concept of superposition

by bringing it to a macroscopic level which is easier to relate to everyday experience. By analogy, it has become customary in quantum mechanics to refer to superposition states where the terms can in some way or other be thought of as macroscopically distinguishable rather loosely as "Schrödinger cat states". As we have seen above, coherent states are in some sense the most classical of light states, in particular when the amplitude is large. Also, they can be detected by homodyne measurements in which a macroscopic photocurrent is measured. Hence in quantum optics the term Schrödinger cat state usually refers to a superposition of coherent states with opposite phase

$$\mathcal{N}\left(e^{i\theta}|\alpha\rangle + e^{-i\theta}|-\alpha\rangle\right). \tag{2.25}$$

The normalisation factor is $\mathcal{N} = (2 + 2\cos(2\theta)e^{-2|\alpha|^2})^{-1/2}$. Whenever cat states are mentioned in this thesis, this is what we mean.

Schrödinger cat states are useful for a variety of tasks. They can form a resource in fault tolerant optical quantum computing [83, 107], they can be converted to two-mode cat states (see below) with applications in teleportation [103, 134] and violations of Bell inequalities [71, 124], and they can also help improve the precision of certain measurements [92]. Motivated by this and by the non-classical nature of the states which makes them fundamentally interesting, there has been much experimental effort to produce cat states. Cat states of light can be produced from coherent states by the Kerr and cross-Kerr effects in non-linear crystals [52, 144], however such non-linearities are typically very weak. Schrödinger 'kitten' states with small amplitudes α can be been generated by subtracting single photons from weakly squeezed vacuum states or equivalently by squeezing single-photon Fock states [37]. Experiments based on this technique have been quite successful, e.g. [50, 96, 102, 126], but it has proved very hard to create cat states with an average photon number $\langle \hat{a}^\dagger \hat{a} \rangle$ significantly larger than 1. Another scheme which allows a squeezed cat state to be generated from a higher-order Fock state by quadrature measurements has also been proposed and implemented [101]. The resulting states had an average photon number of 1.3. In Chap. 5 we present a protocol in which cat states are grown from single photons using linear optics and quadrature measurements.

Two-mode Schrödinger cat states

In analogy with the one-mode cat state (2.25), by a two-mode Schrödinger cat state we refer to a state of the form[1]

$$\mathcal{N}(e^{i\theta}|\alpha,\alpha\rangle + e^{-i\theta}|-\alpha,-\alpha\rangle), \tag{2.26}$$

where the normalisation factor is $\mathcal{N} = (2 + 2\cos(2\theta)e^{-4|\alpha|^2})^{-1/2}$. A two-mode cat can be generated from a one-mode cat by mixing it with a vacuum state on a balanced beam splitter. A balanced beam splitter (with an appropriate choice of

[1] We shall write product states $|\psi\rangle \otimes |\phi\rangle \otimes \cdots$ of multiple modes as $|\psi\rangle|\phi\rangle \ldots$ or $|\psi,\phi,\ldots\rangle$ as is more convenient.

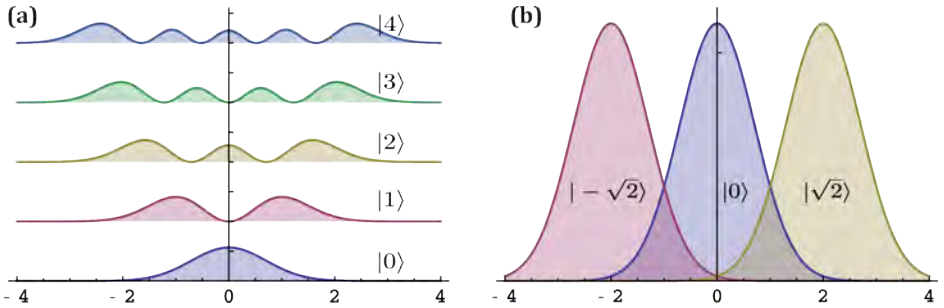

FIGURE 2.2: Probability distributions in $\hat{X}$-space. **(a)** The five lowest Fock states. The distributions are drawn to the same scale but displaced for clarity. **(b)** Coherent states $|\alpha\rangle$ for $\alpha = 0, \pm\sqrt{2}$. Note that the Fock state $|0\rangle$ and the coherent state with $\alpha = 0$ are the same state.

phases) takes $|\alpha\rangle|vac\rangle \rightarrow |\alpha/\sqrt{2}, \alpha/\sqrt{2}\rangle$ and hence transforms (2.25) into a two-mode cat state with amplitude $\alpha/\sqrt{2}$. However, to harness two-mode cats for quantum communication purposes it is desirable to prepare them remotely, since transmitting one output of the beam splitter over a long distance would imply heavy losses due to exponential attenuation. A scheme for preparing non-local two-mode cats by subtraction of a single photon from two local single-mode cats was demonstrated in Ref. [100]. In Chap. 5 we consider a quantum repeater based on two-mode cat states including a scheme for preparing non-local two-mode cats from non-local single-photon states.

2.1.2 Wavefunctions

Any pure state $|\psi\rangle$ of the quantum harmonic oscillator can be described in terms of wavefunctions, defined to be the overlap of $|\psi\rangle$ with the eigenstates of the quadrature operators. In $\hat{X}$-space the wavefunction is $\psi(x) = \langle x|\psi\rangle$. The number and coherent state wavefunctions will be useful later and are given by ([138] p.95, [52] p.50)

$$\psi_{|n\rangle}(x) = \langle x|n\rangle = \frac{1}{\sqrt{2^n n!\sqrt{\pi}}} H_n(x) e^{-x^2/2} \tag{2.27}$$

$$\psi_{|\alpha\rangle}(x) = \langle x|\alpha\rangle = \pi^{-1/4} e^{-|\alpha|^2/2} e^{-(x-\alpha/\sqrt{2})^2 + x^2/2}, \tag{2.28}$$

where H_n denotes the n'th Hermite polynomial. The corresponding $\hat{P}$-space wavefunctions are found by taking the Fourier transform. In a measurement of $\hat{X}$ or $\hat{P}$ the norm square of the appropriate wavefunction gives the distribution of outcomes. In Fig. 2.2 we plot the distributions $|\psi_{|n\rangle}(x)|^2$ for $n = 0, \ldots, 4$ and $|\psi_{|\alpha\rangle}(x)|^2$ for $\alpha = 0$ and $\pm\sqrt{2}$.

2.1.3 Bogoliubov transformations

It is often convenient to express evolution of multi-mode systems in terms of the mode operators in the Heisenberg picture. For example, the interaction of two

spatial light modes on a beam splitter with transmittance η is described by the interaction Hamiltonian $H = i\lambda(\hat{a}_1^\dagger \hat{a}_2 - \hat{a}_1 \hat{a}_2^\dagger)$, where $\cos(\lambda) = \sqrt{\eta}$. Under this Hamiltonian (absorbing the interaction time in λ), $\hat{a}_1$, $\hat{a}_2$ transform according to[2]

$$\begin{aligned} e^{iH}\hat{a}_1 e^{-iH} &= \sqrt{\eta}\hat{a}_1 + \sqrt{1-\eta}\hat{a}_2 \\ e^{iH}\hat{a}_2 e^{-iH} &= -\sqrt{1-\eta}\hat{a}_1 + \sqrt{\eta}\hat{a}_2. \end{aligned} \tag{2.29}$$

Similarly single- and two-mode squeezing is described by interaction Hamiltonians $H = i\frac{1}{2}(\xi \hat{a}^{\dagger 2} - \xi^* \hat{a})$ and $H = i(\xi \hat{a}_1^\dagger \hat{a}_2^\dagger - \xi^* \hat{a}_1 \hat{a}_2)$ as can be seen from (2.18) and (2.21). For squeezing along $\hat{X}$, we have $\xi = r$ real and the corresponding transformations are (see [4] pp. 69,77)

$$\hat{S}^\dagger(s)\hat{a}\hat{S}(s) = \cosh(r)\hat{a} - \sinh(r)\hat{a}^\dagger \tag{2.30}$$

and

$$\begin{aligned} \hat{\mathcal{S}}_{12}^\dagger(r)\hat{a}_1\hat{\mathcal{S}}_{12}(r) &= \cosh(r)\hat{a}_1 - \sinh(r)\hat{a}_2^\dagger \\ \hat{\mathcal{S}}_{12}^\dagger(r)\hat{a}_2\hat{\mathcal{S}}_{12}(r) &= \cosh(r)\hat{a}_2 - \sinh(r)\hat{a}_1^\dagger. \end{aligned} \tag{2.31}$$

More generally, any interaction Hamiltonian which is quadratic in the mode operators leads to linear Heisenberg equations [4]. Hence the evolution can be described by a linear, unitary transformation relating the input and output mode operators, referred to as a 'Bogoliubov transformation'. Denoting output operators by a prime, the most general Bogoliubov transformation U is

$$\hat{a}_j' = U^\dagger \hat{a}_j U = \sum_k b_{jk}\hat{a}_k + c_{jk}\hat{a}_k^\dagger. \tag{2.32}$$

Unitarity ensures that the output operators obey the canonical commutation relations and requires the complex coefficients to fulfil the relation

$$\mathbf{b}\mathbf{b}^\dagger - \mathbf{c}\mathbf{c}^\dagger = \mathbb{1}, \tag{2.33}$$

where $\mathbf{b}$ and $\mathbf{c}$ are matrices with elements b_{jk} and c_{jk}. Bogoliubov transformations are handy for computing expectation values by rewriting them as vacuum expectations. Given a state, such as a squeezed or coherent state, generated from the vacuum $|\psi\rangle = U|vac\rangle$ by some U, the expectation value of an arbitrary function f of the mode operators can be written $\langle\psi|f(\hat{a}_1, \hat{a}_1^\dagger, \ldots)|\psi\rangle = \langle vac|f(\hat{a}_1', \hat{a}'^\dagger, \ldots)|vac\rangle$, where the $\hat{a}_j'$ denote the transformed operators under the Bogoliubov transformation generated by U. We make use of Bogoliubov transformations in Chap. 3 in particular.

2.1.4 Light and atomic ensembles

From the quantisation of the electromagnetic field, we know that modes of light are well described in quantum mechanics by harmonic oscillators. Under suitable conditions, ensembles of atoms with a large ground state population admit an analogous description. In a simple picture we consider atoms with a ground

[2] This may be checked easily using the Baker-Hausdorff lemma, see Ref. [109] p. 96.

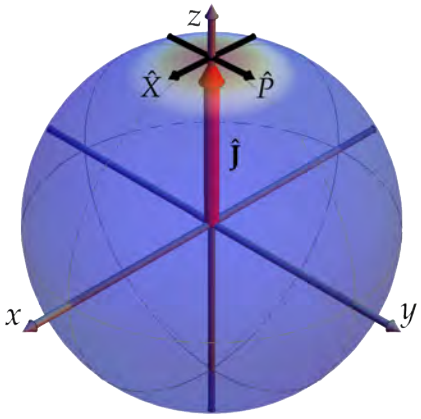

FIGURE 2.3: When the collective atomic spin is strongly polarised, the angular momentum algebra can be approximated by a harmonic oscillator algebra.

state $|g\rangle$ and another stable level $|s\rangle$. These could for example be different hyperfine levels of the electronic ground state in an alkali atom. One can associate angular momentum operators with the j'th atom, defined by [63]

$$\hat{J}_{z,j} = \frac{1}{2}(|g\rangle_j\langle g| - |s\rangle_j\langle s|) \qquad \hat{J}_{x,j} + i\hat{J}_{y,j} = |g\rangle_j\langle s|, \tag{2.34}$$

where we have chosen z as our quantisation axis. It is not hard to verify that these operators obey the usual angular momentum commutation relations $[J_{x,j}, J_{y,j}] = iJ_{z,j}$ etc. As a consequence, so do the collective operators defined by

$$\hat{J}_k = \sum_j \hat{J}_{k,j}, \quad k = x, y, z. \tag{2.35}$$

The collective total angular momentum $\hat{\mathbf{J}}$ can be visualised as a vector living on a sphere, as depicted in Fig. 2.3. The state with all atoms in $|g\rangle$ is an eigenstate of both $\hat{\mathbf{J}}$ and $\hat{J}_z$ with maximal eigenvalue and hence corresponds to the z-pole of the sphere. For small deviations away from the pole – that is, as long as all but a few atoms remain in the ground state – the spherical geometry can effectively be regarded as flat and the angular momentum algebra can be replaced by a harmonic oscillator algebra via the Holstein-Primakoff approximation [66]. Formally, we replace $\hat{J}_z$ by its expectation value and define new operators

$$\hat{X} = \hat{J}_x / \sqrt{\langle \hat{J}_z \rangle}, \qquad \hat{P} = \hat{J}_y / \sqrt{\langle \hat{J}_z \rangle}. \tag{2.36}$$

These operators obey the canonical commutator $[\hat{X}, \hat{P}] = i$. Ladder operators can be defined as $\hat{a} = (\hat{X} + i\hat{P})/\sqrt{2}$, and the corresponding "vacuum" state is the state with all atoms in $|g\rangle$. From (2.34) and (2.35) we see that $\hat{a}^\dagger$ transfers one atom from $|g\rangle$ to $|s\rangle$ but delocalised over the entire ensemble. The excitations generated by $\hat{a}^\dagger$ are referred to as 'spin waves'.

As long as the ensemble remains polarised, light-atom interactions can be conveniently described in terms of the mode operators for light and atomic spin

waves, making it possible e.g. to formulate the input-output relations for atomic-ensemble quantum memories in terms of Bogoliubov transformations, as we do in Chap. 3. The formalism is quite versatile and can describe a number of different interaction schemes, also for multilevel atoms. This is covered in much detail in Ref. [63]. In Chap. 3, we will make use of Bogoliubov transformations for atomic-ensemble memories derived elsewhere, but we defer any further discussion of light-atom interactions to Chap. 4, where we briefly review generation of atomic spin-waves by Raman scattering.

2.2 Entanglement, teleportation, and fidelity

Recall that a state $\hat{\rho}$ of a multipartite quantum system is said to be entangled whenever it cannot be written as a product of states for each subsystem. In particular a system consisting of modes $1, 2, \ldots$ is entangled when $\hat{\rho} \neq \hat{\rho}_1 \otimes \hat{\rho}_2 \otimes \cdots$. A state may be entangled for some divisions of the total system into subsystems and not for others.

We have already seen several examples of entangled states. Two-mode squeezed states display strong correlations between the quadrature variables of the modes and are entangled. The entanglement is also clearly exhibited in the Fock state basis, where

$$\hat{\mathcal{S}}_{12}(r)|vac\rangle = \frac{1}{\cosh r}\sum_n (\tanh r)^n |n,n\rangle. \tag{2.37}$$

Note that the excitation numbers in the two modes are perfectly correlated – the two-mode squeezing operation produces excitations in pairs. In Sec. 2.4.2 we will see how this property of two-mode squeezing is useful for heralded generation of entanglement between distant locations. The two-mode cat states are also entangled. For large α, the coherent states $|\alpha\rangle$ and $|-\alpha\rangle$ are far separated in phase space and hence measurements of the quadrature variables for each mode will show strong correlations for the state (2.26). In the limit of large α, where $|\alpha\rangle$ and $|-\alpha\rangle$ are nearly orthogonal, the two-mode cat states resemble a third, important type of entangled states. For two two-level systems, i.e. two qubits, with basis states $|0\rangle$ and $|1\rangle$, the joint states

$$|\Psi^{\pm}\rangle = \frac{1}{\sqrt{2}}\left(|0,1\rangle \pm |1,0\rangle\right) \qquad |\Phi^{\pm}\rangle = \frac{1}{\sqrt{2}}\left(|0,0\rangle \pm |1,1\rangle\right), \tag{2.38}$$

are commonly referred to as Bell states. They play an important role in many quantum information protocols. For example experiments violating Bell's inequalities have been implemented with Bell states of photon pairs, encoding the qubit states in horizontal and vertical linear polarisation of the photons $|0\rangle = |H\rangle$, $|1\rangle = |V\rangle$ [2, 137].

As an example of how entanglement is harnessed for quantum information protocols we outline how quantum teleportation works. Entanglement swapping whereby two entangled pairs are combined to create one pair over a longer distance is an integral step in any quantum repeater protocol and can be viewed as a generalisation of quantum teleportation to entangled input states.

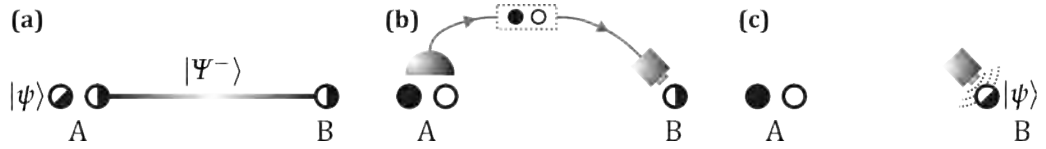

FIGURE 2.4: Quantum teleportation. **(a)** Alice and Bob share an entangled state, and Alice is given a third qubit in an unknown state. **(b)** Alice performs a joint Bell measurement on her qubits and communicates the result to Bob via a classical channel. **(c)** Bob performs a feedback on his qubit and recovers the input state.

2.2.1 Teleportation

Let us assume that two separated parties – in the quantum information community they go by the names Alice (A) and Bob (B) – each possess one qubit, and let us further assume that they have somehow managed to prepare their qubits in the joint singlet state $|\Psi^-\rangle$. As we now show, Alice and Bob can harness the entanglement in this state to transmit an arbitrary, unknown state $|\psi\rangle_{A'} = a|0\rangle_{A'} + b|1\rangle_{A'}$ of a third qubit from A to B using only local operations and classical communication. The process is illustrated in Fig. 2.4. The four Bell states form a basis for the two-qubit Hilbert space, and the joint state of all three qubits can be written in terms of Bell states of Alice's qubits as

$$\begin{aligned} |\psi\rangle_{A'}|\Psi^-\rangle_{AB} &= \frac{1}{\sqrt{2}}\left(a|0\rangle_{A'} + b|1\rangle_{A'}\right)\left(|0,1\rangle_{AB} - |1,0\rangle_{AB}\right) \\ &= \frac{1}{2}\left(|\psi\rangle_B|\Psi^+\rangle_{AA'} + \sigma_z|\psi\rangle_B|\Psi^-\rangle_{AA'} + \sigma_x|\psi\rangle_B|\Phi^+\rangle_{AA'} + \sigma_x\sigma_z|\psi\rangle_B|\Phi^-\rangle_{AA'}\right) \end{aligned} \tag{2.39}$$

where the σ's are Pauli operators acting on Bob's qubit

$$\sigma_x|0\rangle = |1\rangle, \qquad \sigma_x|1\rangle = |0\rangle, \qquad \sigma_z|1\rangle = |0\rangle, \qquad \sigma_z|1\rangle = -|1\rangle. \tag{2.40}$$

That is, σ_x exchanges $|1\rangle$ and $|0\rangle$ (a bit-flip) and σ_z changes the sign of $|1\rangle$ (a phase-flip). If Alice can implement a Bell measurement – that is, a joint, projective measurement of her qubits onto the Bell states – and Bob can implement the two Pauli operators on his qubit, then they can finish the teleportation protocol. Alice measures and sends the classical information about which Bell state she found to Bob. Bob then knows which Pauli operator to apply to his qubit to recover the state $|\psi\rangle$ (since $\sigma_x^2 = \sigma_z^2 = 1$). As a result, they have achieved perfectly faithful transfer of $|\psi\rangle$ from Alice to Bob without the need to exchange any quantum signal and by transmitting just two classical bits. This is a remarkable feat and relies crucially on the shared entanglement. Without any entanglement, all Alice could do would be to send a classical description of $|\psi\rangle$ to Bob who should then attempt to reconstruct it. But since any measurement perturbs the state there is no way for Alice to obtain full information about the coefficients a and b from only a single copy of $|\psi\rangle$ – and even if she did have this information, it would take many classical bits to specify a and b with reasonable precision.

The crux of the teleportation protocol is the preparation of a Bell state and the execution of the Bell measurement, which Alice did in order to obtain information about which Pauli gate Bob should apply to recover the state. Usually the states

$|0\rangle$, $|1\rangle$ correspond to some single-qubit basis in which one can readily measure – e.g. horizontal and vertical polarisation for qubits encoded in photons. The Bell measurement requires a transformation between the basis of entangled Bell states to a basis of product states. This is highly non-trivial to implement, especially for photonic qubits where it turns out that linear optics is insufficient for a deterministic Bell measurement (see Sec. 2.4 below). For ease of implementation, it can be desirable to instead perform a probabilistic measurement which distinguishes some, but not all, of the four Bell states. E.g. a protocol where $|\Psi^{\pm}\rangle$ are correctly identified but $|\Phi^{\pm}\rangle$ lead to a 'not sure' answer indicating that the protocol has failed.

2.2.2 Fidelity

The amount of entanglement contained in a state can be measured by a variety of different measures. For pure states, most of the measures reduce to the so-called entropy of entanglement. We define this measure and use it to compute the amount of entanglement in a two-mode cat state in App. C.1. One can show that the Bell states above maximise this measure, and hence we will sometimes refer to them as 'maximally entangled'. Another measure which is also applicable for mixed states is the Bell parameter, which measures how much a given state violates some Bell inequality. This measure was employed in Ref. [15] on which Chap. 3 is based and we define it in App. A.3. In the main body of this thesis however, we will not make use of entanglement measures.

In the context of quantum repeaters, the goal of a protocol is to distribute entangled states which approach some known, pure target state, for example a Bell state. In this case, it is useful to measure the quality of the output states by how closely they resemble the target. A very common choice for such a measure is the fidelity, which for a given output state $\hat{\rho}$ is defined with respect to a target $|\psi\rangle$ as the overlap

$$F = \mathrm{tr}\left[\hat{\rho}|\psi\rangle\langle\psi|\right] = \langle\psi|\hat{\rho}|\psi\rangle. \tag{2.41}$$

It is not difficult to see that

$$0 \leq F \leq 1, \tag{2.42}$$

with $F = 0$ if and only if the support of $\hat{\rho}$ is on a subspace orthogonal to $|\psi\rangle$ and $F = 1$ if and only if $\hat{\rho} = |\psi\rangle\langle\psi|$.

To gauge the performance of an experimental implementation of a protocol such as quantum teleportation or a quantum repeater, one can compare the average fidelity of the output states with the best possible fidelity which can be obtained by classical means, i.e. by local measurements, local state preparation, and classical communication. For quantum repeaters which distribute Bell states, the classical benchmark is $1/2$ since with classical means one can only prepare a mixture of product states, and the overlap of a Bell state with any product state is at most $1/2$. For teleportation experiments one needs to be careful about which assumptions are made about the distribution of input states. In the discrete variable regime, the classical benchmark for teleportation of a qubit is $2/3$, assuming that all possible states of a single qubit are equally likely inputs [86].

In the continuous variable regime, the benchmark for teleportation of coherent states, assuming a flat input distribution, is 1/2 [16, 62]. However in a realistic setting not all coherent states are equally likely – if not for other reasons then simply because the total available energy is limited – and the bound has to be adjusted for this. For a discussion see [62].

In the context of constructing quantum repeater schemes, the concern is not so much with the classical bound on fidelity. The bound of course needs to be attained to enable quantum communication, but the ambition is for something more. In the introductory chapter, the purpose of a quantum repeater was said to be scalable distribution of entangled states. More precisely what we mean by this is that the rate should scale sub-exponentially with distance for a fixed minimum fidelity of the output states with respect to the target. That is, to judge the performance of our repeater, we fix a value, say 90%, and then determine the maximum rate at which the repeater can deliver states with at least this fidelity as a function of distance.

2.3 Detection of light

All measurements in the quantum communication schemes we will consider are measurements of light. Sometimes the light is used to convey information about atomic states in a quantum memory, at other times we are simply interested in the state of light itself. In either case, we need to model optical detection.

2.3.1 Ideal single photon detection and homodyning

Photodetectors measure the intensity of incoming light, that is they effectively measure $\hat{a}^\dagger\hat{a}$ of some mode $\hat{a}$. Detectors employed at high intensities do not resolve individual photons, but at very low intensities detectors that can resolve single photons from the vacuum are used. An ideal photon counting detector can be modelled as performing a projective measurement onto the Fock states for the detected light mode. That is, a projective measurement with measurement operators $P_n = |n\rangle\langle n|$ where $n = 0, 1, 2, \ldots$ is the photon number. Often, detectors that are sensitive to single photons are only able to distinguish between absence and presence of light but not between one or multiple photons. Such detectors are sometimes referred to as 'bucket' detectors. An ideal bucket detector can be modelled by a projective measurement with projectors $P_{dark} = |vac\rangle\langle vac|$ and $P_{light} = \mathbb{1} - |vac\rangle\langle vac|$.

Phase information is not directly accessible in optical measurements, because all photodetectors measure the intensity and not the field. It is possible however to perform measurements that are sensitive to phase, by interfering the light to be detected with a beam of controllable amplitude and phase in a mode matched to overlap the incoming mode. In particular, it is possible to measure any field quadrature $\cos(\theta)\hat{X} + \sin(\theta)\hat{P}$ by so-called balanced homodyne detection. The setup is shown in Fig. 2.5. The mode to be measured, denoted 'signal', is mixed on a 50/50 beam splitter with a strong coherent state $|\alpha\rangle$, referred to as the 'local

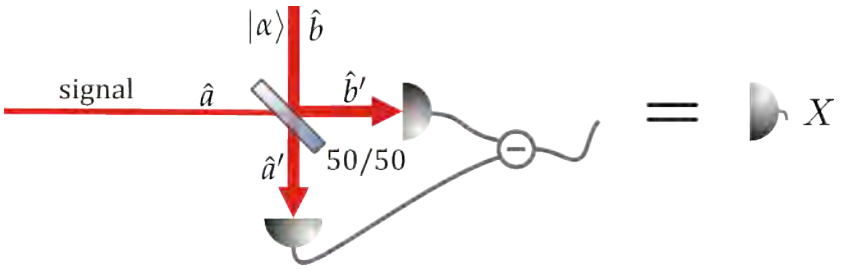

FIGURE 2.5: Balanced homodyne detection. The signal field is mixed with a local oscillator in a coherent state. The difference current of the detectors is proportional to a quadrature of the signal field determined by the phase of the local oscillator.

oscillator'. The intensities at each output are measured by regular photodetectors, and the difference is recorded. For an appropriate choice of phases, the output and input modes of the beam splitter are related by $\hat{a}' = (\hat{a} + \hat{b})/\sqrt{2}$ and $\hat{b}' = (\hat{a} - \hat{b})/\sqrt{2}$, and the currents produced by the two photodetectors are proportional to $\langle \hat{a}'^{\dagger}\hat{a}' \rangle$ and $\langle \hat{b}'^{\dagger}\hat{b}' \rangle$. Denoting the phase of the local oscillator by θ, such that $\alpha = |\alpha|e^{i\theta}$, the difference current is therefore

$$\begin{aligned} I \propto \langle \hat{a}'^{\dagger}\hat{a}' - \hat{b}'^{\dagger}\hat{b} \rangle &= \langle \hat{a}^{\dagger}\hat{b} + \hat{b}^{\dagger}\hat{a} \rangle = \langle \alpha\hat{a}^{\dagger} + \alpha^{*}\hat{a} \rangle = |\alpha| \langle e^{i\theta}\hat{a}^{\dagger} + e^{-i\theta}\hat{a} \rangle \\ &= 2\sqrt{2}|\alpha| \langle \cos(\theta)\hat{X} + \sin(\theta)\hat{P} \rangle. \end{aligned} \tag{2.43}$$

We note, that the signal field quadrature is amplified by the amplitude of the local oscillator. This enables quadrature measurements of very weak fields. Because of the local oscillator, the power impinging on the photodetectors is significant even for weak fields, which allows detectors with good quantum efficiency (see below) to be used. Homodyning can have very high efficiency even for fields which cannot be reliably measured by direct intensity detection, with signal-to-noise ratios at the standard quantum limit, i.e. limited only by the inherent quantum noise of the detected light fields.

As indicated in Fig. 2.5, we will picture homodyning by a single detector in our figures. One should keep in mind though that a local oscillator is always present and that a common phase reference is typically required across all measurements to make it meaningful to talk about quadrature measurements in the same phase-space coordinate frame [18].

2.3.2 Losses and dark counts

In the laboratory, optical detectors convert the intensity of incoming light to electric current which can then be processed by an electronic circuit. Most commonly photodiodes are employed, but various other types of detectors are also in use. An important number characterising an optical detector is it's quantum efficiency, which is the intrinsic probability that an incoming photon will be detected by the detector, not regarding coupling losses. In the case of a diode, it is the fraction of incoming photons for which an electron-hole pair is produced. Regular diodes in the near infrared range can have very high quantum efficiencies, well above 90%, and so give accurate intensity measurements. However,

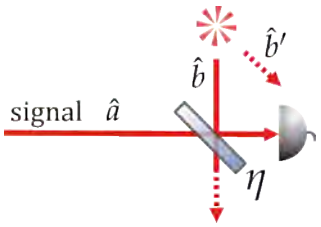

Figure 2.6: Modelling loss and dark counts by mixing with a thermal state on a fictitious beam splitter. The thermal state can be generated from a fictitious two-mode squeezed state.

they are not useful for very low intensity inputs because the signal drowns in electronic noise. Typically, powers on the order of microwatts are needed for reliable detection. To detect single photons, detectors with internal gain are used. For example avalanche photodiodes and photomultiplier tubes which can measure very low intensities because each single-photon detection event creates an avalanche leading to a signal above the electronic noise floor. However, the quantum efficiency of such single-photon detectors is usually limited to about 60% or less and they mostly do not discriminate between events where a single or several photons hit the detector [60]. At present, promising new technologies which attain high efficiencies and photon number resolution are emerging but are not yet widely available or applicable[3]. In addition to quantum efficiency, another quantity characterising imperfect detectors is the dark count rate or dark current. A dark count is a spurious event in which the detector outputs a signal although no light is present in the measured mode, e.g. due to thermal creation of electron-hole pairs in a diode. Dark counts are particularly troublesome for single-photon detection, and typical rates lie in the 10-100Hz regime [60].

Imperfect detectors can be modelled as ideal detectors preceded by fictitious optical elements inserted in the path of the measured light. A detector with sub-unity efficiency η is typically modelled by a fictitious beam splitter with transmittance η placed in front of an ideal detector. In Chap. 3 we also model detector dark counts (internal as well as background noise) by injecting a state with a non-zero mean photon number in the other port of the fictitious beam splitter. The setup is illustrated in Fig. 2.6. Denoting the signal mode $\hat{a}$, the fictitious mode $\hat{b}$, and the state of the fictitious mode $\hat{\rho}_b$, the initial, joint state $\hat{\rho}$ of mode $\hat{a}$ and any other physical modes of our system is transformed to

$$\hat{\rho}' = \mathrm{tr}_b \left[U^\dagger(\eta) \left(\hat{\rho} \otimes \hat{\rho}_b \right) U(\eta) \right], \tag{2.44}$$

where the fictitious mode has been traced out and $U(\eta)$ denotes the beam-splitter transformation (2.29). Following a measurement outcome corresponding to projector P_i, where i may stand for either photon number or dark/light in the cases of photon counting or bucket detectors respectively, the normalised output state becomes

$$\hat{\rho}_{out} = \frac{\mathrm{tr}_a \left[P_i^\dagger \hat{\rho}' P_i \right]}{\mathrm{tr} \left[P_i^\dagger \hat{\rho}' P_i \right]}. \tag{2.45}$$

[3]These include superconducting transition-edge sensors and solid-state photomultipliers operated at low temperatures. See Ref. [60] for an overview of contemporary single-photon detectors.

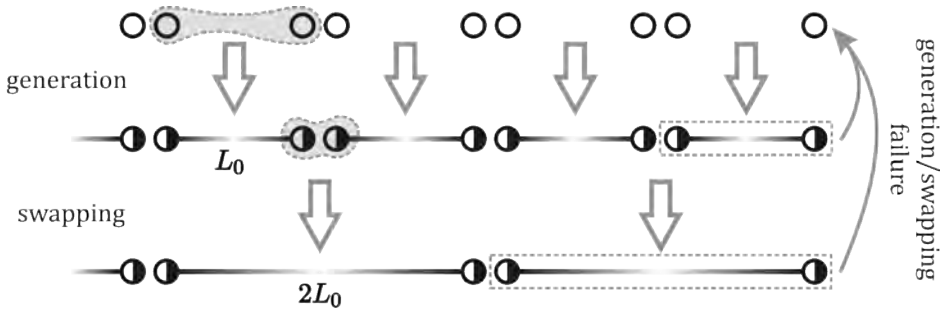

FIGURE 2.7: Repeater structure. A channel is divided into multiple segments of length L_0. In the first step of the protocol, neighbouring nodes are entangled. In subsequent steps adjacent segments are connected by entanglement swapping at every other node. This is repeated until one pair spans the entire channel. Each step is probabilistic. When a step fails, the affected segments are reinitialised.

Since the dark count noise is incoherent, the state ρ_b should be a mixture with a suitable distribution of photon numbers. In Chap. 3 we use a thermal distribution, which we generate from the vacuum by two-mode squeezing (it should become clear later why this is convenient). Tracing out one mode of a two-mode squeezed state one finds

$$\mathrm{tr}_{b'}\,\hat{S}_{bb'}(s)|vac\rangle = \frac{1}{\cosh^2(r)}\sum \tanh^{2n}(r)|n\rangle_b\langle n| \tag{2.46}$$

which is exactly a thermal distribution with mean photon number $\bar{n} = \sinh^2(r)$, related to the temperature T by $e^{-\hbar\omega/k_BT} = \bar{n}/(\bar{n}+1)$.

2.4 Quantum repeaters with probabilistic operations

Here we describe the general structure of quantum repeaters and some features which are common to the systems that will be considered in the next three chapters. As explained in the introductory chapter, the goal of a quantum repeater is to establish entanglement between two separated parties in a scalable manner, i.e. at a rate which scales polynomially (or at least sub-exponentially) with distance.

The repeaters we consider all have the basic structure illustrated in Fig. 2.7. A channel of length L is divided into 2^n segments of length L_0. Entanglement is initially generated over these shorter segments and stored in quantum memories at the nodes. Entanglement swapping is then used to double the length of the entangled pairs. The swapping is achieved by performing measurements at every other node and communicating the measurement results to the nodes which are now entangled. This process is iterated n times, generating an entangled pair of length $L = 2^n L_0$. Both the entanglement generation and entanglement connection steps are probabilistic and when they fail the protocol must be restarted for all affected segments. The use of quantum memories ensures that entanglement in unaffected segments is not lost.

A probabilistic approach to entanglement connection is motivated by ease of experimental implementation. In particular, linear optics and single photon detection are well-established, attractive technologies. However, it turns out to be impossible to implement a deterministic Bell measurement using only these means as proven by Lütkenhaus, Calsamiglia and Suominen [84] and later generalised by van Loock and Lütkenhaus [136]. Thus any entanglement swapping scheme based on linear optics and detection of single photons must be probabilistic. Furthermore, in the spirit of the original DLCZ proposal, one can think of the probabilistic nature of both entanglement generation and swapping as providing a kind of 'built in purification' of errors. By designing the generation and connection steps appropriately, it is possible to trade success probability or equivalently time for higher fidelity entangled states. That is, successful generation or connection attempts herald the creation of states with good fidelity, but this comes at the cost of a decreased probability of success i.e. a decrease in rate.

2.4.1 Rate

For any repeater with the general structure in Fig. 2.7, the rate is determined by the probabilities for successful generation, connection, and (when necessary) postselection which we shall denote respectively by p_0, p_i with $i = 1, \ldots, n$, and p_{ps}. How these probabilities vary with L and n will depend on the particular protocol at hand, but we can devise a general expression for the rate in terms of them. The rate will also be influenced by how quickly generation attempts can be repeated, the time spent on local operations and measurements during swapping, and the time required for classical communication. When an entanglement swapping (or generation) attempt is made at level i of the protocol, classical information about the outcome must be communicated over a distance $2^i L_0$ before the protocol can proceed. We will make an assumption which is common in the quantum repeater literature[4], namely that any local operations at the repeater nodes are fast compared with the time it takes to send a classical signal between neighbouring nodes, given by $\tau = L_0/c$ where c is the speed of light. With this assumption, the average time t_n needed to create an entangled pair of length L obeys the recursion equation

$$t_{n+1} = p_{n+1}^{-1}(\tau 2^n + t'_n) \tag{2.47}$$

where t'_n is the average time it takes to create two neighbouring entangled pairs of length L. A simple expression for the repeater rate can be obtained by solving this equation replacing t'_n by t_n, i.e. by approximating the waiting time for two pairs by that of a single pair. However, such an estimate turns out to considerably overshoot the actual rate as found by stochastic simulation. A much better approximation is found by moving the approximation one step lower, i.e. by instead taking the recurrence for t'_n to be

$$t'_{n+1} = \nu_{n+1}(\tau 2^n + t'_n). \tag{2.48}$$

[4]See e.g. [111, 112, 135]. For the repeaters in this thesis a typical segment length is $L_0 \sim 100\,\mathrm{km}$ corresponding to about 0.5 ms and hence the timescale of local operations, in particular mapping into and out of the quantum memories, needs to be much smaller than this.

Here ν_n is the average number of tries needed for two independent binomial events (generation or connection), each with probability p_n, to both succeed. It is given by

$$\nu_n = \frac{3 - 2p_n}{(2 - p_n)p_n}, \tag{2.49}$$

and the recurrence has the solution

$$t'_n = \tau(2^{n-1}\nu_n + \cdots + 2^0\nu_n \ldots \nu_1 + \nu_n \ldots \nu_1\nu_0). \tag{2.50}$$

For the protocols we shall look at, the success probability for entanglement generation is small, $p_0 \ll 1$. When at the same time the connection probabilities are also less than one-half[5] $p_i < 1/2$, the expression (2.50) can then be simplified since

$$\frac{2^{n-1}\nu_n + \cdots + \nu_n \ldots \nu_1}{\nu_n \ldots \nu_1\nu_0} \leq \frac{1}{\nu_0}\left[1 + \cdots + \left(\frac{3}{4}\right)^{n-1}\right] \leq \frac{4}{\nu_0} \leq 4p_0, \tag{2.51}$$

and thus

$$t'_n \approx \tau\nu_n \ldots \nu_1\nu_0. \tag{2.52}$$

Taking into account a final postselection step, this leads to the following expression for the rate[6]

$$R = t_n^{-1} = \tau^{-1}p_{ps}\nu_n^{-1} \ldots \nu_0^{-1} \approx \tau^{-1}\left(\frac{2}{3}\right)^{n+1} p_{ps}p_n \ldots p_0 \tag{2.53}$$

Equivalent expressions are given in the review Ref. [111], in Refs. [113, 114, 119], and (2.53) also agrees with the empirical estimate found in Ref. [72]. The final simplification $\nu_i^{-1} \approx 2p_i/3$ is exact in the limit of small p_i and leads to a deviation of the rate by at most a factor 1.125^n which is less than ~ 2.5 for the n's relevant to us. We have found that stochastic simulation of the rate for given p_i shows good agreement with (2.53).

2.4.2 Heralded entanglement from two-mode squeezing

The schemes treated in the three main Chapters 3, 4 and 5 all make use of some form of two-mode squeezing combined with single-photon detection to produce entanglement, and we therefore describe the process here. The idea of entangling remote quantum systems by interference and detection of single photons was first introduced in 1999 by Cabrillo *et al.* [22] and extended to teleportation by Bose et al. [10] (although no squeezing was employed in these proposals). It has since been used in a number of theoretical proposals, notably the DLCZ scheme[7] and all the schemes that build on it [41, 111], and has also been implemented in experiment, e.g. [90, 100, 143].

[5] This has to be the case for linear optical entanglement swapping in the discrete regime without auxiliary states [23].

[6] It appears that to date, no exact closed-form expression for the rate has been obtained [111]. The rate problem can be given a compact formulation in terms of stochastic variables, distribution functions and probability generating functions, but a solution has so far escaped this author...

[7] The equivalence between the entanglement generation process of the DLCZ protocol and general two-mode squeezing followed by storage was mentioned in Refs. [12, 119].

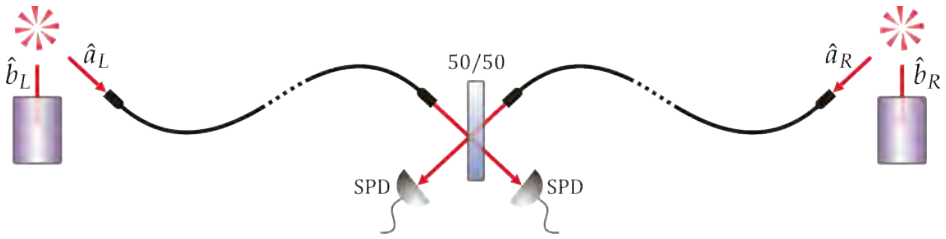

FIGURE 2.8: Entanglement generation with pair sources. Two sources each produce pairs of excitations in a storage mode and a photonic mode, which is transmitted to the central beam splitter. After mixing on the beam splitter, the photonic modes are measured by single-photon detectors. Generation is successful when exactly one click is registered.

The generic setup is depicted in Fig. 2.8. Two identical sources are positioned some distance apart. Each source randomly produces pairs of excitations in a photonic mode $\hat{a}$ and a storage mode $\hat{b}$, which may be photonic but could also be different in nature, e.g. an atomic spin-wave mode. The photonic modes are brought to overlap at a balanced beam splitter positioned halfway between the sources and then measured by single-photon detectors. The idea of the entanglement process is now very simple. If the probability for producing more than a single pair is very small, then the detection of a photon unambiguously heralds the creation of a single excitation in the local modes. Since the beam splitter makes it impossible to distinguish from which source the photon came, the result is an entangled state. The process can be seen as an application of entanglement swapping. The photonic modes $\hat{a}_L$, $\hat{a}_R$ are initially entangled with their stored counterparts $\hat{b}_L$, $\hat{b}_R$, where the subscripts refer to the left- and right-hand sides. By a measurement on the photonic modes, the entanglement is then swapped to modes $\hat{b}_L$, $\hat{b}_R$. Crucially, the setup works even if the channels connecting the detectors to the sources are very lossy. Loss may decrease the probability that a photon is detected, but it does not degrade the state created when detection does happen.

For our purposes, the states produced by the sources are two-mode squeezed states. The joint state of the two sources can be written, c.f. (2.37)

$$\left[\frac{1}{\cosh r}\sum_n \frac{(\tanh r)^n}{n!}(\hat{a}_L^\dagger \hat{b}_L^\dagger)^n\right]\left[\frac{1}{\cosh r}\sum_n \frac{(\tanh r)^n}{n!}(\hat{a}_R^\dagger \hat{b}_R^\dagger)^n\right]|vac\rangle. \tag{2.54}$$

When the squeezing is weak, this reduces to

$$\left[1+\sqrt{p}\,(\hat{a}_L^\dagger \hat{b}_L^\dagger + \hat{a}_R^\dagger \hat{b}_R^\dagger) + O(p)\right]|vac\rangle, \tag{2.55}$$

where $p \ll 1$ is the probability (per source) to create a pair of excitations. The beam splitter takes $\hat{a}_L \to (\hat{a}_L + \hat{a}_R)/\sqrt{2}$ and $\hat{a}_R \to (\hat{a}_L - \hat{a}_R)/\sqrt{2}$. Taking into account a phase difference ϕ between the left and right arms and ignoring losses for the present, the state right before the measurements is

$$\left[1+\sqrt{p}\,\hat{a}_L^\dagger \frac{\hat{b}_L^\dagger + e^{i\phi}\hat{b}_R^\dagger}{\sqrt{2}} + \sqrt{p}\,\hat{a}_R^\dagger \frac{\hat{b}_L^\dagger - e^{i\phi}\hat{b}_R^\dagger}{\sqrt{2}} + O(p)\right]|vac\rangle. \tag{2.56}$$

From this expression we see that, to lowest order in p, a detector click projects the storage modes to a maximally entangled state

$$|\psi_\phi^\pm\rangle = \frac{1}{\sqrt{2}}(\hat{b}_L^\dagger \pm e^{i\phi}\hat{b}_R^\dagger)|vac\rangle = \frac{1}{\sqrt{2}}(|10\rangle \pm e^{i\phi}|01\rangle), \tag{2.57}$$

where the sign is defined by which detector clicks. This ideal state is obtained even for lossy channels since, to lowest order in p, at most one photon is emitted and hence a detector click implies that no loss took place. We remark that a known phase ϕ can easily be removed. As discussed below, even if it is unknown a static phase can be eliminated by postselection while fluctuating phases lead to decoherence.

Contributions from multiple excitations – i.e. the $O(p)$ terms in (2.55) – degrade the final state, thus forcing one to work with low success probability for the entanglement generation. When channel losses are low, such errors can be mitigated by using photon counting detectors and discarding events with multiple detector clicks. However, one often desires to entangle sources separated by many channel attenuation lengths. In that case, even when multiple excitations are created, the probability for more than one photon to reach the detectors is very low and there is therefore no benefit to counting. To see how the final state is affected by multiple excitations, we compute the contribution from the next-order term in (2.55). The term is given by

$$p\left[\hat{a}_L^\dagger\hat{b}_L^\dagger\hat{a}_R^\dagger\hat{b}_R^\dagger + \frac{1}{2}(\hat{a}_L^\dagger\hat{b}_L^\dagger)^2 + \frac{1}{2}(\hat{a}_R^\dagger\hat{b}_R^\dagger)^2\right]|vac\rangle \tag{2.58}$$

We assume both channels to have the same transmission η_c and the detectors to have efficiency η_d. The losses in each arm of the setup are modelled by fictitious beam splitters of transmission $\eta = \eta_c\eta_d$. Dropping p, taking $\phi = 0$ for simplicity, and evolving the term up to the measurements we get

$$\begin{aligned}&\hat{b}_L^\dagger\hat{b}_R^\dagger(\sqrt{\frac{\eta}{2}}(\hat{a}_L^\dagger + \hat{a}_R^\dagger) + \sqrt{1-\eta}\hat{c}_L^\dagger)(\sqrt{\frac{\eta}{2}}(\hat{a}_L^\dagger - \hat{a}_R^\dagger) + \sqrt{1-\eta}\hat{c}_R^\dagger)\\ &+ \frac{1}{2}\hat{b}_L^{\dagger 2}(\sqrt{\frac{\eta}{2}}(\hat{a}_L^\dagger + \hat{a}_R^\dagger) + \sqrt{1-\eta}\hat{c}_L^\dagger)^2 + \frac{1}{2}\hat{b}_R^{\dagger 2}(\sqrt{\frac{\eta}{2}}(\hat{a}_L^\dagger - \hat{a}_R^\dagger) + \sqrt{1-\eta}\hat{c}_R^\dagger)^2,\end{aligned} \tag{2.59}$$

where the fictitious beam splitter modes are denoted by $\hat{c}$. We now imagine that the left detector clicks. If we take it to be a bucket detector and trace out the fictitious modes, we get a mixed state for the storage modes

$$\begin{aligned}&\eta(1-\eta)\left(\left[\frac{1}{\sqrt{2}}|11\rangle + |20\rangle\right]\otimes h.c. + \left[\frac{1}{\sqrt{2}}|11\rangle + |02\rangle\right]\otimes h.c.\right)\\ &+\eta^2\left(\left[\frac{1}{\sqrt{2}}|11\rangle + \frac{1}{2}|20\rangle + \frac{1}{2}|02\rangle\right]\otimes h.c.\right),\end{aligned} \tag{2.60}$$

where $h.c.$ stands for hermitian conjugate. This expression gives us the error introduced by double excitations. The first line corresponds to a situation where one photon reaches the detector, while the second photon is lost. The second line corresponds to both photons reaching the detector. For a typical configuration

with low channel transmissivity $\eta \ll 1$, the second line can be dropped, and the normalised final state becomes

$$\rho = (1-3p)|\psi_0^+\rangle\langle\psi_0^+| + 3p\,\rho_p, \tag{2.61}$$

where

$$\rho_p = \frac{1}{2}\left(\left[\sqrt{\frac{1}{3}}|11\rangle + \sqrt{\frac{2}{3}}|20\rangle\right] \otimes h.c. + \left[\sqrt{\frac{1}{3}}|11\rangle + \sqrt{\frac{2}{3}}|02\rangle\right] \otimes h.c.\right) \tag{2.62}$$

The fidelity of the output state with respect to the maximally entangled state is simply

$$F = \langle\psi_0^+|\rho|\psi_0^+\rangle = 1-3p. \tag{2.63}$$

We thus see that the quality of the entangled state generated by the setup in Fig. 2.8 is determined solely by the pair production probability p. This is the reason that p must be kept small.

2.4.3 Single- versus dual-rail entanglement

The entangled state (2.57) which consists of a single excitation delocalised between two separated modes can be viewed as an entangled state of two qubits, each encoded in the vacuum $|0\rangle = |vac\rangle$ and one-excitation $|1\rangle = \hat{a}^\dagger|vac\rangle$ Fock states. A qubit encoded in this way is said to be encoded 'single-rail'. Single-rail entanglement as-is is of limited use because it is difficult to perform measurements of a single-rail qubit in any basis other than that of the Fock states, which is insufficient for most interesting applications. For example an implementation of the Ekert cryptography scheme or a test of Bell's inequality requires measurements in a rotated basis such as $(|0\rangle \pm |1\rangle)/\sqrt{2}$. In a single-rail encoding, the transformation

$$|0\rangle \to \frac{1}{\sqrt{2}}\left(|0\rangle + |1\rangle\right), \qquad |1\rangle \to \frac{1}{\sqrt{2}}\left(|0\rangle - |1\rangle\right), \tag{2.64}$$

known in quantum computing terminology as a Hadamard gate, changes the energy of the state and thus cannot be implemented by passive operations (e.g. linear optics). Instead of encoding qubits single-rail one can use two modes $\hat{a}$, $\hat{b}$ and qubit basis states $|0\rangle = \hat{a}|vac\rangle$ and $|1\rangle = \hat{b}|vac\rangle$. Such an encoding is referred to as 'dual-rail'. For a dual-rail encoding using two modes of light, the Hadamard gate becomes a simple beam-splitter operation, and indeed any single-qubit rotation can be implemented with linear optics. Dual-rail entanglement is thus much more directly useful.

With this concern in mind, it is not completely obvious that the states given by (2.57) are useful at all in the context of quantum communication. However, they can be used to construct dual-rail entanglement via postselection.

Postselection

As proposed in Ref. [41], two entangled single-rail states can be combined to behave like one dual-rail entangled state via postselection. Imagine that we are

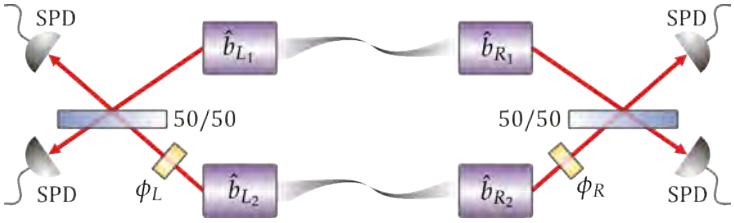

FIGURE 2.9: Test of Bell's inequalities with postselection, as proposed in Ref. [41]. Two copies of the same single-rail entangled state are used. On the left- and right-hand sides of the setup, one mode from each pair impinges on a beam splitter and the outputs are measure. A Bell-type experiment is realised by varying the phase-shifts ϕ_L and ϕ_R and accepting only events with one detector click on each side. The Ekert quantum cryptography scheme can be realised by the same setup [44].

given a state of the form

$$|\psi_\phi^+\rangle_1|\psi_{\phi'}^+\rangle_2 = \frac{1}{2}(\hat{b}_{L_1}^\dagger + e^{i\phi}\hat{b}_{R_1}^\dagger)(\hat{b}_{L_2}^\dagger + e^{i\phi'}\hat{b}_{R_2}^\dagger)|vac\rangle, \tag{2.65}$$

and imagine that we perform some protocol consisting of local operations on the left- and right-hand sides of the channel, followed by measurements of all four modes. This could for example be a setup for testing Bell's inequalities, as shown in Fig. 2.9. If we accept only outcomes with exactly one click on each side, then terms of the form $\hat{b}_{L_1}^\dagger\hat{b}_{L_2}^\dagger|vac\rangle$, $\hat{b}_{R_1}^\dagger\hat{b}_{R_2}^\dagger|vac\rangle$ in our state cannot contribute. For such a protocol, the state is therefore effectively equivalent to

$$\frac{1}{\sqrt{2}}(\hat{b}_{L_1}^\dagger\hat{b}_{R_2}^\dagger + e^{i(\phi-\phi')}\hat{b}_{R_1}^\dagger\hat{b}_{L_2}^\dagger)|vac\rangle, \tag{2.66}$$

which is a maximally entangled dual-rail state.

Note that if the two single-rail pairs are prepared using the same channels and if phases are static, then $\phi = \phi'$ and the postselection step also eliminates the phase in (2.66). The phase $\phi = k\delta x$ is determined by the path length difference δx between the two arms in Fig. 2.8 and the wavenumber k of the light. Fluctuations in the path lengths will hence cause the phases to drift in time, leading to decoherence of the postselected state. In the single-rail repeater protocol discussed in the next chapter, entanglement of the form (2.57) is generated and swapped over the full length of the repeater and postselection is performed only as a final step. In that case, as argued in Ref. [27], the phases need to be stabilised for the entire duration of the protocol leading to extremely demanding requirements for interferometric stability. The stability requirements can be significantly relaxed by basing the repeater scheme on dual-rail rather than single-rail entanglement and by generating entanglement via detection of two coincident photons rather than a single photon. At the same time the use of dual-rail entanglement allows for active purification of errors (including phase errors) with linear optics [27, 72, 114, 145]. Another possibility which has been investigated is to generate the entanglement in a Sagnac interferometer setup, where the excitation pulses inducing two-mode squeezing travel in opposite direction through the same channels as the detected photons [89]. In this case, phase stabilisation is needed only on the scale of the pulse travel time. In the remainder of this thesis

we will not be very much concerned with interferometric stability, however one should keep in mind that it is an issue which needs to be addressed in experimental implementations.

Also note that postselection implies a probabilistic application of the entangled states. Starting from (2.57), the probability for successful postselection is $1/2$. Postselection is thus not suitable for one-time communication tasks, e.g. where one is given a single copy of some quantum state which must be reliably teleported. However, several interesting applications including quantum cryptography protocols and tests of Bell's inequalities do admit probabilistic implementations [41].

Chapter 3

Analysing single-rail ensemble-based repeaters

The work presented in this chapter aims to analyse how imperfections in the quantum memories, losses and dark counts impact the overall performance of a quantum repeater with an architecture like that of the 2001 proposal by Duan *et al.* (DLCZ) [41]. The original motivation for this was to understand, whether a DLCZ-type repeater could be implemented with the atomic ensemble memories demonstrated in 2004 by the Polzik group at the Niels Bohr Institute [74], and hence our analysis has been developed for a fixed basic architecture and with atomic-ensemble-based memories in mind. Nevertheless, we develop a rather general model to describe the repeater, and in particular the memories, in an implementation independent way. We parametrise the memories by a Bogoliubov transformation, which allows us to describe any process with an interaction Hamiltonian quadratic in the mode operators. This formalism applies to ensemble-based memories and to other systems as well. For example it has recently been realised that certain nanomechanical systems admit such a description, e.g. coupling of atoms to tiny membranes [61]. Entanglement generation is described in terms of a two-mode squeezing operation which encompasses both the Raman scattering atom-light interaction of the original DLCZ protocol as well as other schemes such as parametric down conversion of light. The original DLCZ architecture suffers low rates due to a fast-growing vacuum component of the generated states which is a consequence of the single-rail nature of the entanglement in the protocol. In addition it is not robust against phase errors caused e.g. by interferometric instabilities as discussed in Sec. 2.4.3. Within recent years, several more sophisticated protocols based on dual-rail entanglement and also compatible with atomic ensemble memories have been proposed [72, 114, 145]. These schemes achieve significantly better rates and thus DLCZ is not a likely candidate for experimental realisation of a repeater over long distances. However the methods we have developed provide insight into the error behaviour of ensemble-based quantum memories and could be applied also to the more involved repeater protocols. The work in this chapter has been published in Ref. [15].

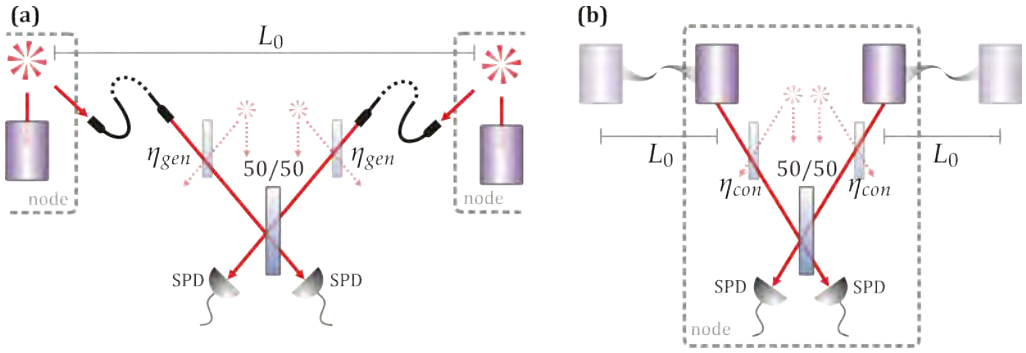

FIGURE 3.1: **(a)** Entanglement generation. One mode from each of two separated squeezing sources is transmitted to a balanced beam splitter and measured, while the remaining modes are stored in quantum memories. Success is conditioned on a single detector click. **(b)** Entanglement swapping. To connect two entangled pairs, modes stored at one node are retrieved, mixed on a beam splitter and measured. Success is conditioned on a single click. Loss and dark counts during both generation and swapping are modelled by fictitious beam splitters and sources of squeezing.

3.1 Repeater model

Our model repeater is defined by the setups for entanglement generation and connection, illustrated in Fig. 3.1. To generate entanglement in one repeater segment of length L_0, we consider a setup as in Sec. 2.4.2 with two sources of two-mode squeezing, which we can think of concretely as two non-degenerate parametric down converters (PDC's). Each PDC produces weak two-mode squeezing in a pair of photonic modes. A single excitation is removed non-locally from the two squeezed pairs, by mixing one mode from each pair on a balanced beam splitter and conditioning on a single click (Fig. 3.1a). As explained in detail in Sec. 2.4.2, under ideal conditions this leaves a Bell state to be stored in the atomic memories

$$|\Psi^{\pm}\rangle = \frac{1}{\sqrt{2}}(|01\rangle \pm |10\rangle). \tag{3.1}$$

The probability for entanglement generation to succeed is proportional to the pair-production probability p of the PDC's. For small p it is $\sim 2\eta_{gen}p$, where η_{gen} is the transmittance of the fibre links. To extend the entanglement distance, two neighbouring segments are connected by mixing one mode from each on a balanced beam splitter and conditioning on a single click (Fig. 3.1b). This removes one excitation from the pair of Bell states and leaves the memories at the central node empty. There is thus one excitation left in the two outermost nodes. The beam splitter erases any information about which segment lost an excitation and hence the outermost modes are again in a Bell state after connection. Thus by iterating the swapping procedure n times, under ideal conditions the protocol generates a maximally entangled pair over the distance $L = 2^n L_0$.

It was shown by Duan *at al.* that a protocol of the type in Fig. 3.1 overcomes transmission losses, yielding a sub-exponential scaling of the rate [41]. Other errors, however, are not purified in this scheme. Our goal in this chapter is to make a detailed investigation of the effect of various types of noise on the efficiency of

the protocol. The imperfections that we will consider are: (i) *transmission losses*, (ii) *detector dark counts* and (iii) *memory imperfections*. In addition, we will consider both photon-counting and bucket detectors, since it is interesting to see what, if anything, may be gained by using single-photon counters, which are difficult to realise experimentally (c.f. Sec. 2.3). We do not consider errors introduced by interferometric instability, such as path-length fluctuations, in the entanglement generation setup. We note that the original scheme of Duan *et al.* [41] is a special case of the protocol considered here obtained for perfect memories, i.e. in the absence of type-(iii) noise.

Transmission losses

To model the transmission losses (i), fictitious beam splitters are inserted into the setup as illustrated in Fig. 3.1. For simplicity we assume that the memories are located close to the PDC's, such that losses in the memory arms are small and can be treated perturbatively as memory imperfections. In the detector arms of the entanglement generation and connection setups, the loss probabilities are $1-\eta_{gen}$ and $1-\eta_{con}$ respectively. This includes both transmission losses and a detector efficiency η_{det}. Since entanglement generation requires the photons to travel a distance $L_0/2$ we have $\eta_{gen} \lesssim \eta_{det}\, e^{-L_0/2L_{att}}$, where L_{att} is the fibre attenuation length, while connection takes place locally so $\eta_{con} \lesssim \eta_{det}$. Therefore we will typically have $\eta_{gen} \ll \eta_{con}$.

Dark counts

To model the dark counts (ii), we assume that the signals to be measured are mixed with thermal states, which we generate by inserting virtual PDC's (see Fig. 3.1). We choose a thermal distribution for the dark-counts, because this is easily treated as a Bogoliubov transformation (see below). The repeater setup we consider is only feasible for $\bar{n}_{dc} \ll 1$, where $\bar{n}_{dc}$ is the average number of dark counts per detector in one measurement cycle. Therefore only the first-order contribution from dark counts is considered, and the actual distribution is not important. The detector dark count rate determines the squeezing parameter in the virtual PDC's (see App. A.2).

Memory imperfections

Memory imperfections (iii) depend on the particular type of quantum memory employed in the setup. We devise a general description of the memories. The incoming and outgoing light fields are conveniently described by harmonic oscillator degrees of freedom, and ideally the memories map the state of the incoming light to the outgoing light. In the Heisenberg picture this implies a mapping $\hat{a}' = \hat{a}$, where $\hat{a}'$ and $\hat{a}$ are the field operators for the outgoing and incoming modes respectively. In the presence of imperfections, the state transfer will be described by an admixture of other field operators into the outgoing mode. Such a process can in many cases be described by a Bogoliubov transformation (see

Sec. 2.1.3). We are mainly interested in describing quantum memories based on atomic ensembles. To leading order, they are typically described by interaction Hamiltonians which are quadratic in the field operators for the light and atoms [63]. In this case, the resulting state evolution can always be described by a Bogoliubov transformation, even in the presence of imperfections such as spontaneous emission. We shall consider quantum memories described by the most general possible Bogoliubov transformation and our results thus apply to a broad class of quantum memories. Our calculations cannot, however, describe interactions with Hamiltonians of order higher than quadratic in the field operators. E.g. we cannot describe the optical Kerr effect or single-atom memories.

3.1.1 Figures of merit

The figures of merit for the repeater are the rate R and fidelity F with which entangled pairs are generated as functions of distance. As we will see below, and as noted in Ref. [41], when detectors are inefficient or do not resolve the photon number, the final state will contain a large vacuum component with no excitations in the ensembles. That is, in the absence of other errors, the final state becomes

$$\lambda|\Psi^{\pm}\rangle\langle\Psi^{\pm}| + (1-\lambda)|vac\rangle\langle vac|, \tag{3.2}$$

where λ may be much less than 1. For this reason, it is not obvious that the states produced by the repeater are useful at all. However, the postselection procedure described in Sec. 2.4.3 by which dual-rail entanglement is extracted from a pair of single-rail states also removes the vacuum component, since the vacuum can never contribute to successful detection events. Thus, provided that fidelity conditioned on successful postselection is high, interesting applications such as quantum cryptography, Bell inequality tests, or teleportation can be performed [41, 111]. We define the postselected fidelity of the state $\hat{\rho}$ by

$$F = \frac{\langle\Psi^{+}_{ps}|\hat{\rho}|\Psi^{+}_{ps}\rangle}{\mathrm{tr}\, P_{ps}\,\hat{\rho}\,P_{ps}}, \tag{3.3}$$

where $|\Psi^{+}_{ps}\rangle$ is a maximally entangled dual-rail state and P_{ps} is the projection operator unto the set of states which fulfil the postselection criterion of one excitation on each side (we assume that appropriate phase flips are performed such that the relevant target is always $|\Psi^{+}_{ps}\rangle$ rather than $|\Psi^{-}_{ps}\rangle$). Referring to the labelling of modes in Fig. 2.9

$$|\Psi^{+}_{ps}\rangle = \frac{1}{\sqrt{2}}(\hat{b}^{\dagger}_{L_1}\hat{b}^{\dagger}_{R_2} + \hat{b}^{\dagger}_{R_1}\hat{b}^{\dagger}_{L_2})|vac\rangle, \tag{3.4}$$

and

$$\begin{aligned} P_{ps} =& \hat{b}^{\dagger}_{L_1}\hat{b}^{\dagger}_{R_1}|vac\rangle\langle vac|\hat{b}_{L_1}\hat{b}_{R_1} + \hat{b}^{\dagger}_{L_1}\hat{b}^{\dagger}_{R_2}|vac\rangle\langle vac|\hat{b}_{L_1}\hat{b}_{R_2} \\ &+ \hat{b}^{\dagger}_{L_2}\hat{b}^{\dagger}_{R_1}|vac\rangle\langle vac|\hat{b}_{L_2}\hat{b}_{R_1} + \hat{b}^{\dagger}_{L_2}\hat{b}^{\dagger}_{R_2}|vac\rangle\langle vac|\hat{b}_{L_2}\hat{b}_{R_2}. \end{aligned} \tag{3.5}$$

Below, we investigate the impact of imperfections on the scaling of F with distance and find the scaling of R for a fixed target fidelity.

We remark that while the fidelity is by far the most popular figure of merit used in the quantum repeater literature, it is not the only possible choice. Depending on the intended application, other ways of quantifying the entanglement in the states distributed by the repeater may be equally relevant. In the published work Ref. [15], which contains most of the result covered in the present chapter, a different quantity known as a Bell parameter was used. This parameter is a direct measure of how useful a state is for testing Bell's inequality. More detail on the Bell parameter as a figure of merit is provided in App. A.3.

3.2 Methods

To understand how imperfections in the repeater protocol influence the rate and fidelity, we start by computing the two-mode density matrix $\hat{\rho}_n$ of the entangled pairs at each step of the repeater protocol, i.e. as a function of L/L_0. Computing $\hat{\rho}_n$ may be broken into two principal steps. First, computing the state $\hat{\rho}_0$ from entanglement generation (Fig. 3.1a) and second, computing $\hat{\rho}_n$ for $n > 0$ by iterating the connection process (Fig. 3.1b). To deal with these two tasks, in particular the dependence on the atomic memory, we have developed a framework for calculating the output state from an arbitrary Bogoliubov transformation followed by projective measurements, given an input state. Our method is based on a *generating function* $\mathcal{F}$. Using this generating function, we can compute $\hat{\rho}_n$ both analytically and numerically. In our analytical treatment we consider all errors except simple losses perturbatively and independently. Numerically, we do not need to make this approximation and hence the numerical results serve as a check that our analytical expressions are valid[1].

3.2.1 Generating function

The function $\mathcal{F}$ takes two variables for each input and each output mode, and is defined such that its derivatives evaluated at zero form a matrix transforming the input to the output state in the Fock-state basis. E.g., for a single input and output mode,

$$\langle i|\hat{\rho}_{out}|j\rangle = \sum_{k,l} M_{ijkl} \times \langle k|\hat{\rho}_{in}|l\rangle, \tag{3.6}$$

$$M_{ijkl} = \left[\frac{1}{\sqrt{i!j!k!l!}} \frac{\partial^k}{\partial\alpha^k} \frac{\partial^l}{\partial\beta^l} \frac{\partial^i}{\partial\gamma^i} \frac{\partial^j}{\partial\delta^j} \mathcal{F}(\alpha,\beta,\gamma,\delta) \right]_{\mathbf{0}}. \tag{3.7}$$

For a given Bogoliubov transformation and set of projection operators, we can compute $\mathcal{F}$ which then in turn allows us to find $\hat{\rho}_{out}$ for any given $\hat{\rho}_{in}$.

We define the generating function in the general case where our system $\mathcal{S}$ has arbitrarily many modes, some of which are output while the remaining modes are measured or traced out. Symbolically $\mathcal{S} = \mathcal{OR}$, where $\mathcal{O}$ are the output and

[1] Note though that we do need to make a cut-off in the photon number, since working with large matrices is not practical.

$\mathcal{R}$ the remaining modes. If the system is subject to a Bogoliubov transformation U and a subsequent measurement with an outcome corresponding to projection operator P, then quantum mechanics dictates that the unnormalised output state is

$$\hat{\rho}_{\mathcal{O}}^{out} = \mathrm{tr}_{\mathcal{R}}(PU\hat{\rho}_{\mathcal{S}}^{in}U^{\dagger}P^{\dagger}). \tag{3.8}$$

Picking some basis labelled $|\mathfrak{o}\rangle$ for $\mathcal{O}$ and a basis labelled $|\mathfrak{s}\rangle$ for $\mathcal{S}$, the matrix elements of this density matrix can be written

$$\langle \mathfrak{o}|\hat{\rho}_{\mathcal{O}}^{out}|\mathfrak{o}'\rangle = \sum_{\mathfrak{s},\mathfrak{s}'} \left[\mathrm{tr}_{\mathcal{R}}\langle \mathfrak{o}|PU|\mathfrak{s}\rangle\langle \mathfrak{s}'|U^{\dagger}P^{\dagger}|\mathfrak{o}'\rangle\right] \times \langle \mathfrak{s}|\hat{\rho}_{\mathcal{S}}^{in}|\mathfrak{s}'\rangle. \tag{3.9}$$

The generating function corresponding to the Bogoliubov transformation U and measurement operators P allows us to compute the first factor under the sum in the basis of Fock states. It is defined to be

$$\begin{aligned}\mathcal{F} = \mathrm{tr}_{\mathcal{R}}\,[{}_{\mathcal{O}}\langle 0| \left(\prod_o e^{\delta_o \hat{a}_o}\right) PU \left(\prod_i e^{\beta_i \hat{a}_i^{\dagger}}\right)|vac\rangle \\ \otimes \langle vac| \left(\prod_i e^{\alpha_i \hat{a}_i}\right) U^{\dagger}P^{\dagger} \left(\prod_o e^{\gamma_o \hat{a}_o^{\dagger}}\right)|0\rangle_{\mathcal{O}}]\end{aligned} \tag{3.10}$$

where i runs over all modes of $\mathcal{S}$ and o runs over the output modes $\mathcal{O}$. The parameters α_i, β_i and γ_i, δ_i are real and correspond to the input and output modes respectively. To see that it makes sense to define $\mathcal{F}$ like this, note that any Fock state $|n\rangle$ can be written

$$|n\rangle = \frac{1}{\sqrt{n!}}(\hat{a}^{\dagger})^n|0\rangle = \left[\frac{1}{\sqrt{n!}}\frac{\partial^n}{\partial \alpha^n}e^{\alpha \hat{a}^{\dagger}}|0\rangle\right]_{\alpha=0}, \tag{3.11}$$

where α can be chosen real. Combining (3.11) and (3.10), we can generalise (3.6)-(3.7), and we see that $\mathcal{F}$ does indeed generate the output state. To compute $\mathcal{F}$ for given U and P, it is convenient to rewrite (3.10) in terms of displacement operators

$$\begin{aligned}\mathcal{F} = e^{\frac{1}{2}\Sigma} \times \langle vac| \left(\prod_i \hat{D}_i(-\alpha_i)\right) U^{\dagger}P^{\dagger} \\ \times \left(\prod_o \hat{D}_o(\gamma_o)|0\rangle_o\langle 0|\hat{D}_o(-\delta_o)\right) PU \left(\prod_i \hat{D}_i(\beta_i)\right)|vac\rangle.\end{aligned} \tag{3.12}$$

This expression, with $\Sigma = \sum_i(\alpha_i^2 + \beta_i^2) + \sum_o(\gamma_o^2 + \delta_o^2)$, follows from (3.10) by the circular property of the trace and the relation

$$e^{\alpha \hat{a}^{\dagger}}|0\rangle = e^{\frac{1}{2}|\alpha|^2}\hat{D}(\alpha)|0\rangle, \tag{3.13}$$

which is a consequence of the disentangling theorem[2]. We can then make use of several properties of displacement operators. First, one may prove (see App. A.1) that the vacuum projection operator can be written as the integral

$$|0\rangle\langle 0| = \int \frac{dpdx}{2\pi} e^{-(x^2+p^2)/4}\hat{D}\left(\frac{x+ip}{\sqrt{2}}\right). \tag{3.14}$$

[2]The disentangling theorem states that if $[A,[A,B]] = [B,[A,B]] = 0$ for a pair of operators A, B, then $e^{A+B} = e^A e^B e^{-\frac{1}{2}[A,B]}$ ([52] p. 49). It is a consequence of the Baker-Hausdorff lemma.

It follows from (3.11) that the projection onto any Fock state can be written in terms of derivatives of an integral over a product of displacement operators. Second, under a Bogoliubov transformation given by

$$U^\dagger \hat{a}_j U = \sum_i b_{ji}\, \hat{a}_i + c_{ji}\, \hat{a}_i^\dagger, \tag{3.15}$$

the displacement operators transform as

$$U^\dagger \hat{D}_j(\beta) U = \prod_i \hat{D}_i(\beta b_{ji}^* - \beta^* c_{ji}). \tag{3.16}$$

And third, the product and vacuum expectation value of displacement operators are given by

$$\hat{D}(\alpha)\hat{D}(\beta) = e^{i\mathrm{Im}(\alpha\beta^*)}\hat{D}(\alpha+\beta), \tag{3.17}$$

$$\langle 0|\hat{D}(\alpha))|0\rangle = e^{-\frac{1}{2}|\alpha|^2}. \tag{3.18}$$

Starting from (3.12), the function $\mathcal{F}$ is found in four steps. First, all projection operators in the expression are replaced by integrals of displacement operators by making use of (3.14). Second, the Bogoliubov transformation is eliminated from the expression via (3.16). Third, the integrals are pulled outside the vacuum expectation which then contains only a product of displacement operators, and the expectation value is evaluated by using (3.17) and (3.18). Last, the resulting Gaussian function is integrated and we obtain an analytic expression for $\mathcal{F}$ involving only the $\alpha, \beta, \gamma, \delta$-variables and the parameters of U.

Projection operators and squeezed initial states

The generating function as defined above can be computed for any measurement described by a projection in the Fock state basis. However, for our purposes measurements where a single or no click is observed are sufficient. When bucket detectors are employed, the possible measurement outcomes correspond to the projectors $P_{dark} = |0\rangle\langle 0|$ and $P_{light} = \mathbb{1} - P_{dark}$, with P_{dark} given by (3.14). When photon counters are used, the relevant projectors are $P_0 = P_{dark}$ and

$$P_1 = |1\rangle\langle 1| = \left[\frac{\partial^2}{\partial\alpha\partial\beta} e^{(|\alpha|^2+|\beta|^2)/2} D(\alpha)|0\rangle\langle 0|\hat{D}(\beta)\right]_{\alpha,\beta=0}. \tag{3.19}$$

The generating function also in principle allows for any input state. In practice, it is not convenient to work with high photon numbers, because the density matrices become large and calculation of high-order derivatives is required, c.f. (3.7). However, a certain class of input states can be treated exactly regardless of photon number. For any state of the form $U_{in}|vac\rangle$, where the operator U_{in} generates a Bogoliubov transformation, we see from (3.8) that we can substitute UU_{in} for U and take the input state to be $|vac\rangle$. In particular, we can treat two-mode squeezed input states exactly by taking $U_{in} = \hat{S}_{ij}(s)$. This is the reason, we model the dark counts sources by two-mode squeezers. An example is included in App. A.2.

3.2.2 Mode reduction and parametrisation

The Bogoliubov transformation for a full state transfer (i.e. storage and subsequent retrieval) of a light mode through a realistic atomic memory often involves many auxiliary modes in addition to the input and output modes. In the most general case, according to (2.32) the mode operator for the retrieved light is given by

$$\hat{a}_1' = b_1\hat{a}_1 + c_1\hat{a}_1^\dagger + \mathbf{b}\cdot\hat{\mathbf{a}} + \mathbf{c}\cdot\hat{\mathbf{a}}^\dagger, \tag{3.20}$$

where $\hat{a}_1$ is for the input mode (in the notation of Ref. [15]). The state transfer is perfect when $b_1 = 1$ and only b_1 is non-zero. Additional terms are due to imperfections. To simplify calculation of the generating function and the general description of the memories, it is convenient to parametrise the general transformation in terms of only a few parameters. This is possible by defining new, independent mode operators $\hat{a}_2$, $\hat{a}_3$ as

$$b_2\hat{a}_2 = \mathbf{b}\cdot\hat{\mathbf{a}}, \qquad\qquad c_2\hat{a}_2^\dagger + c_3\hat{a}_3^\dagger = \mathbf{c}\cdot\hat{\mathbf{a}}^\dagger, \tag{3.21}$$

where b_2, c_2, c_3 are complex coefficients. The transformation (3.20) can then be written in terms of just three modes

$$\hat{a}_1' = b_1\hat{a}_1 + c_1\hat{a}_1^\dagger + b_2\hat{a}_2 + c_2\hat{a}_2^\dagger + c_3\hat{a}_3^\dagger. \tag{3.22}$$

Unitarity requires that

$$|b_1|^2 + |b_2|^2 - |c_1|^2 - |c_2|^2 - |c_3|^2 = 1. \tag{3.23}$$

We perform our analysis below in terms of the transformation (3.22). The results can then be applied to any memory described by a given Bogoliubov transformation by relating the parameters b_1, b_2, c_1, c_2, c_3 to the physical properties of the memory, through (3.20) and (3.21). There is some freedom in the choice of phases of the b's and c's. With the proper choice, all but one of them may be assumed real. The phases of b_1, c_1 can be adjusted by simple phase shifts of the input and output modes. It can be seen, that in our repeater setup a phase shift on the output mode has no effect on the measurement outcomes during swapping, and hence we may always assume that either b_1 or c_1 is real. It is not obvious that choosing both of them real corresponds to an optimal phase choice in terms of F, however we have checked numerically that a phase change of the input mode has negligible effect. Hence we may take b_1 and c_1 both real. Any complex phase on b_2 can be absorbed into the definition of $\hat{a}_2$, and likewise the phase of c_3 can be absorbed in $\hat{a}_3$. Consequentially, we can assume that all parameters but c_2 are real.

An illustration of mode reduction is provided in App. A.2 where we show how (3.22) can be modified to account for dark counts during entanglement swapping.

3.2.3 Example

As an example of how we compute $\hat{\rho}_n$, consider now a very idealised repeater setup, where the errors are small and due solely to memory imperfections. We

neglect transmission losses and detector inefficiency, and we assume the entanglement generation to produce a perfect Bell-state, $\hat{\rho}_0 = |\Psi^+\rangle\langle\Psi^+|$. The parameters of the memories are for now assumed to fulfil

$$b_2, c_2, c_3 = 0, \qquad b_1^2 - 1 = c_1^2 \ll 1 \tag{3.24}$$

with b_1, c_1 real. Using these assumptions we can compute the generating function corresponding to entanglement connection and from the generating function we can find $\hat{\rho}_n$. It is convenient to include the full state transfer through the memories (light to atoms to light) in the connection step such that $\hat{\rho}_n$ denotes the state of two entangled light modes after n connection steps. The Bogoliubov transformation corresponding to connection is found using (3.22) and (3.24) and $\mathcal{F}$ can then be computed from (3.12). Using $\mathcal{F}$ starting from $\hat{\rho}_0$ we find $\hat{\rho}_n$ for the first few steps $n = 1, 2, ...$, at each step expanding it to second order in c_1. Based on the results we come up with the following ansatz

$$\hat{\rho}_n = \begin{pmatrix} 1 - 2f_n + (2f_n - 1 + 2g_n)c_1^2 & 0 & 0 & (1 - 2f_n)c_1 \\ 0 & f_n - g_n c_1^2 & f_n - g_n c_1^2 & 0 \\ 0 & f_n - g_n c_1^2 & f_n - g_n c_1^2 & 0 \\ (1 - 2f_n)c_1 & 0 & 0 & (1 - 2f_n)c_1^2 \end{pmatrix}, \tag{3.25}$$

where $\hat{\rho}_n$ is given in the Fock state basis, and f_n, g_n are unknown, real-valued functions to be determined. Our ansatz will be confirmed, if it is preserved under entanglement connection and the resulting recursion equations for f_n, g_n can be uniquely solved. Connecting two copies of $\hat{\rho}_n$ and expanding to second order in c_1, we find that the ansatz is indeed preserved if

$$\begin{aligned} f_{n+1} &= \frac{f_n}{2 - f_n}, \\ g_{n+1} &= \frac{4f_n(4 + g_n) + 11f_n^3 - 20f_n^2 - 4}{2f_n(f_n - 2)^2}. \end{aligned} \tag{3.26}$$

For $\hat{\rho}_0$ to take the correct form, we must have $f_0 = \frac{1}{2}$, $g_0 = 0$. We thus need to solve (3.26) subject to this initial condition. Making the variable substitution $\tilde{f}_n = f_n^{-1}$ we get

$$\tilde{f}_{n+1} = 2\tilde{f}_n - 1, \tag{3.27}$$

which has the solution

$$\tilde{f}_n = 2^n + 1. \tag{3.28}$$

Inserting the expression for f_n into the g_n-recurrence and making the substitution $\tilde{g}_n = 2(2^n + 1)g_n$ one finds the recurrence equation

$$\tilde{g}_{n+1} = 2\tilde{g}_n - 2^{3n+2} + 2^{2n+2} - 3, \tag{3.29}$$

Which yields the solution

$$\tilde{g}_n = -\frac{1}{3}(2^n - 1)(2^{2n+1} - 2^{n+2} - 9). \tag{3.30}$$

Performing the inverse variable substitutions, the solutions of (3.26) are

$$\begin{aligned} f_n &= \frac{1}{2^n+1}, \\ g_n &= \frac{-2^{1+3n}+3\cdot 2^{1+2n}+5\cdot 2^n-9}{3\cdot 2(2^n+1)^2}. \end{aligned} \tag{3.31}$$

The fidelity of the state (3.25) is

$$F = \frac{(f_n - c_1^2 g_n)^2}{f_n^2 - (2f_n g_n - (2f_n-1)^2)c_1^2 - ((2f_n-1)(2f_n+2g_n-1) - g_n^2)c_1^4} \tag{3.32}$$

Now, if c_1 is small, we can plug in the solutions for f_n, g_n and expand in c_1. Using $L/L_0 = 2^n$, we arrive at the following result

$$F = 1 - (L/L_0 - 1)^2 c_1^2 \approx 1 - (L/L_0)^2 c_1^2 \tag{3.33}$$

to second order in c_1. The last expression is valid when the number of segments L/L_0 is large.

The above example illustrates how we derive analytical results for F: except for transmission losses and detector inefficiencies, which may be considerable, errors are treated perturbatively and independently. First $\hat{\rho}_0$ is computed, and then an ansatz for $\hat{\rho}_n$ to the desired order in the error is found, leading to recurrence equations which are solved[3] with initial conditions given by $\hat{\rho}_0$. To verify our analytical results, we have also performed numerical simulations, for which it is not necessary to treat the errors perturbatively or independently (although we do impose a cut-off on the excitation number). Using our analytical expressions for the generating functions corresponding to entanglement generation (Fig. 3.1a) and swapping (Fig. 3.1a) we numerically compute $\hat{\rho}_n$ for two specific atomic quantum memories and various values of the losses, initial squeezing and dark count rates. The results are presented in the next section.

One may in principle derive an expression for the rate R valid for a repeater based on a general memory, by making use of the generating function as we have done for F. The generation and swapping success probabilities p_i appearing in the expression (2.53) for R can be found by taking the trace of (3.8). However, in the regime where the repeater attains good fidelity and memory imperfections can be treated perturbatively, these do not influence the rate much. The error in F due to memory imperfections may be regarded as fixed. The error introduced in entanglement generation can be controlled by adjusting the pair-production probability, and the rate is primarily determined by the need to keep this error smaller than the fixed error. When computing the rate, we therefore consider only losses and finite initial squeezing, since other imperfections will only slightly perturb the results.

[3]The recurrence equations tend to be considerably more complicated when losses are included, and in some cases we have not been able to obtain a closed analytical solution. In those cases we have obtained an exact solution of the recurrence numerically (by substituting the equation into itself) and from this solution we have deduced the behaviour at large L/L_0. Subsequently we have verified, by comparing with numerical simulations, that the analytical expressions thus obtained are also valid for L close to L_0.

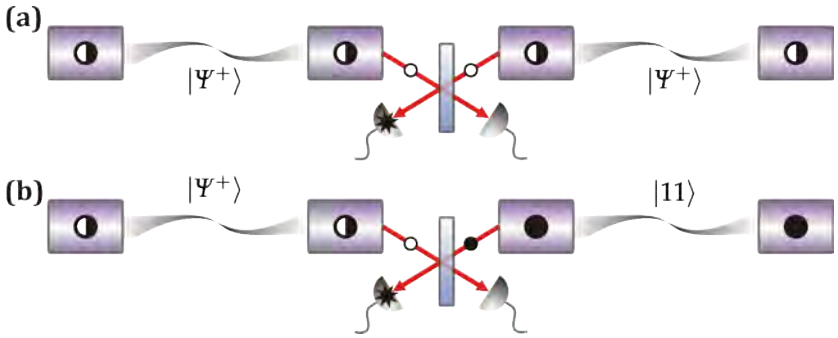

Figure 3.2: Creation and propagation of errors. Filled circles represent excitations, empty circles represent vacuum. **(a)** During connection of two segments in the ideal state $|\Psi^+\rangle$, vacuum is read out but the connection is accepted due to a detector dark count leaving the remaining modes in the separable state $|11\rangle$. **(b)** Connecting $|11\rangle$ with an ideal entangled state requiring a single click leads to $|11\rangle$ (without loss).

3.3 Results

In the first section below we present our analytical, perturbative results for the postselected fidelity based on a general Bogoliubov-transformation model for the quantum memories. In the following section, the analytical approximations are compared to numerical simulations for specific atomic quantum memories.

3.3.1 Analytical results

In the subsections below, we give expressions for the fidelity obtained by perturbation in each error source separately, treating errors as independent. Afterwards, we deal with cross terms and identify the regime in which it is safe to treat perturbations independently.

To get an intuitive idea of the nature of the errors, notice that ideally the entangled state at any step of the repeater protocol contains exactly one excitation. Losses alone, which remove excitations from the state, cannot degrade the final fidelity, since a state with no excitations will be filtered out by postselection. Errors occur whenever superfluous excitations are introduced into the system, since in combination with loss these degrade the final fidelity. Fig. 3.2 shows how a dark count during entanglement swapping introduces an error which propagates through the protocol and leads to a separable output state $|11\rangle$ which is not filtered out by postselection when combined with the vacuum state $|00\rangle$. In what follows, we use similar considerations to understand the scaling of F obtained by perturbation.

Imperfect memories and connection dark counts

Dark counts occurring during entanglement swapping can be treated as memory imperfections by considering the virtual PDC and beam splitter introduced in Fig. 3.1 (b) to be a part of the memory protocol. We therefore treat these two

error sources simultaneously. The Bogoliubov transformation used to model connection dark counts is simply a special case of the general memory transformation. An expression for it is derived in App. A.2.

We take the Bogoliubov transformation for a full state transfer through the atomic memories to be (3.22). We do perturbation in each parameter of the transformation separately, and proceed as in the example in Sec. 3.2.3, neglecting all other error sources except transmission losses. The transmission in entanglement swapping is η_{con} (see Fig. 3.1b). One may check that to leading order, perturbation in the Bogoliubov transformation parameters do not yield any cross-terms, and hence it is justified to add the contributions obtained by treating the parameters independently. For the case without photon counting, we find

$$\begin{aligned} F = 1 &- 4(L/L_0)^2(1-\frac{1}{2}\eta_{con})^2|c_1|^2 \\ &- 6(L/L_0)^2(1-\frac{1}{2}\eta_{con})(|c_2|^2+|c_3|^2+\frac{\bar{n}_{dc}}{\eta_{con}}), \end{aligned} \tag{3.34}$$

and for the case with photon counting

$$\begin{aligned} F = 1 &- 4(L/L_0)^2(1-\eta_{con})^2|c_1|^2 \\ &- 6(L/L_0)^2(1-\eta_{con})(|c_2|^2+|c_3|^2+\frac{\bar{n}_{dc}}{\eta_{con}}). \end{aligned} \tag{3.35}$$

For the perturbation to be valid, the error in F must be much less than 1, and so we require $c_1, c_2, c_3 \ll 1$ and $\bar{n}_{dc} \ll \eta_{con}$. In addition, the expressions above were derived in the large L limit $L_0 \ll L$ and we give only the leading order in L. However, we have verified that the expressions are a good approximation to the exact analytical result for F (which could not be put on a closed form) also for $L \sim L_0$, as long as the perturbative condition is fulfilled.

There are several things to notice about the results (3.34) and (3.35). First, note that F is independent of the parameter b_2. This is because b_2 corresponds to a plain loss. If b_2 is the only imperfection, the transformation (3.22) is passive leading only to an increase of the vacuum component of $\hat{\rho}_n$, which does not influence the postselected fidelity. For the same reason, there is no term in F depending only on the transmission η_{con}. In the presence of additional imperfections, such as dark counts, losses do influence F. However since b_2 is treated perturbatively, only η_{con} enters the formulae above. Second, note that when the photons are counted, errors are suppressed for perfect transmission $\eta_{con} \to 1$, whereas they persist even for perfect transmission when the photons are not counted. This, and also the scaling of the error with L and p_{con}, may be motivated by the following simple picture.

In the case of only c_1 non-zero the unitarity condition (3.23) becomes $|b_1|^2 - |c_1|^2 = 1$, and it follows that the effect of non-zero c_1 is single-mode squeezing of the input mode. Similarly the effect of non-zero c_2 or c_3 is two-mode squeezing of the input mode and an auxiliary mode. The effect of the memories on the state $\hat{\rho} = \hat{\rho}_n \otimes \hat{\rho}_n$ during entanglement swapping where L, R denote the measured modes is to take

$$\hat{\rho} \to \hat{S}_L(s_1)\hat{S}_R(s_1)\,\hat{\rho}\,\hat{S}_L^\dagger(s_1)\hat{S}_R^\dagger(s_1) \tag{3.36}$$

or

$$\hat{\rho} \to \mathrm{Tr}_{lr}\left[\hat{S}_{Ll}(s_2)\hat{S}_{Rr}(s_2)\,\hat{\rho}\,\hat{S}^{\dagger}_{Ll}(s_2)\hat{S}^{\dagger}_{Rr}(s_2)\right] \tag{3.37}$$

where l, r are two auxiliary modes, and $s_1 \approx 1 + 2c_1$, $s_2 \approx 1 + 2c_2$ in the perturbative limit. $\hat{S}_i(\cdot)$ and $\hat{S}_{ij}(\cdot)$ are the single and two-mode squeezing operators defined in Sec. 2.1.1. From these expressions we see, that c_1 errors introduce photon pairs into the measured modes, while c_2 and c_3 errors introduce single photons. To lowest order in the c's, the amplitudes for errors to occur are c_1, c_2, c_3 and hence the error in F scales with $|c_1|^2, |c_2|^2, |c_3|^2$. Now, for an error to survive postselection (see Fig. 2.9) any superfluous excitations must be removed before the postselection stage. In the case of photon counting detectors, this can happen only through photon loss, and therefore the c_1 and c_2, c_3 error terms scale with $(1-\eta_{con})^2$ and $1-\eta_{con}$ respectively. In the case of bucket detectors, in addition to loss, superfluous excitations can be removed when multiple photons are incident on the same detector producing only a single click. This is the reason that errors persists for perfect transmission and is apparent by the replacement $\eta_{con} \to \eta_{con}/2$ from (3.35) to (3.34). To understand the scaling with L, note that there are $L/L_0 - 1$ connection attempts in total. There are therefore L/L_0 ways for a photon to get lost and L/L_0 ways for an extra photon to be introduced. In a c_2 or c_3 error one extra photon is introduced and thus one photon must get lost, whereas in a c_1 error two photons are added and two photon must get lost. However one of the added photons must get lost in the connection attempt in which it was created, since successful connection requires exactly one detector click, and the scaling for both types of error is therefore L^2. Since dark counts are modelled by mixing of the signal mode with a two-mode squeezed state (Fig. 3.1) this error term scales the same way as the c_3 term. This is also apparent from the derivation of the Bogoliubov transformation in App. A.2. Note that as $\eta_{con} \to 0$, the probability that a given click is a dark count approaches 1 and the dark-count error term diverges.

Finite initial squeezing

As seen in Sec. 2.4.2, the two-mode squeezing sources used for entanglement generation contribute also unwanted excitations, degrading the final state fidelity. The probability to generate an unwanted excitation is set by the photon-pair generation probability p, and it is therefore desirable to keep p small. At the same time, the success probability for entanglement generation and hence the rate is proportional to p, which should therefore not be too small. Here we examine the effect of finite initial squeezing, i.e. finite p, on the postselected fidelity F for the final entangled state. We have determined the final state $\hat{\rho}_n$ by first computing the state $\hat{\rho}_0$ produced by entanglement generation (Fig. 3.1a) to first order in p and then proceeding as in Sec. 3.2.3, neglecting all imperfections except transmission losses. Going to first order in p is equivalent to taking a maximal photon number of two, and hence $\hat{\rho}_n$ is described by a 9x9 matrix in this case. The results for the fidelity are

$$F = 1 - 6(L/L_0)^2(1 - \frac{1}{2}\eta_{gen})(1 - \frac{1}{2}\eta_{con})p \tag{3.38}$$

without photon counting, and

$$F = 1 - 6(L/L_0)^2(1 - \eta_{gen})(1 - \eta_{con})p \tag{3.39}$$

with photon counting.

As expected, the error terms are proportional to p. The extra photons come in pairs with one in the detector and one in the memory arm of Fig. 3.1a, and hence the situation is analogous to that of c_1-type errors above. Two photons must get lost before the postselection stage, and one of these must get lost in the generation attempt in which it was created, since a single detector click is required for successful generation. With photon counting this type of error is suppressed when there is no loss in generation ($\eta_{gen} \to 1$) or connection ($\eta_{con} \to 1$), but persist for perfect transmission if the photons are not counted.

Generation dark counts

Finally, we consider the effect of dark counts during entanglement generation, neglecting errors due to finite squeezing, connection dark counts or memory imperfections. Again, $\hat{\rho}_n$ can be derived by means of the generating function for the setup Fig. 3.1a. To lowest order in the dark count probability $\bar{n}_{dc}$ we find, without photon counting

$$F = 1 - 6(L/L_0)^2(1 - \frac{1}{2}\eta_{gen})\frac{\bar{n}_{dc}}{\eta_{gen}}, \tag{3.40}$$

and with counting

$$F = 1 - 6(L/L_0)^2(1 - \eta_{gen})\frac{\bar{n}_{dc}}{\eta_{gen}}. \tag{3.41}$$

As before, notice that the error is suppressed for $\eta_{gen} \to 1$ in the counting case but not in the non-counting case. Because a dark count alone results in the generation of a vacuum state, it must be combined with a double excitation in some segment to survive postselection. This explains the quadratic scaling of the error. Despite the fact that a double excitation is needed, p does not show up in (3.40) and (3.41), because the total number of generated photons is unchanged with respect to the ideal case.

Perturbation cross terms

So far we have considered each error source independently, and we have perturbatively found their effect on the postselected fidelity. However, we have not addressed the possibility for cross terms in the perturbation, when errors of different type are present simultaneously, as will always be the case experimentally. Indeed, cross terms do appear and may have a severe effect on F for certain values of the parameters. Here we identify the regime where cross terms can be safely neglected.

We find that the significant cross terms are those arising from the combination of a generation dark count with a memory imperfection or a connection dark

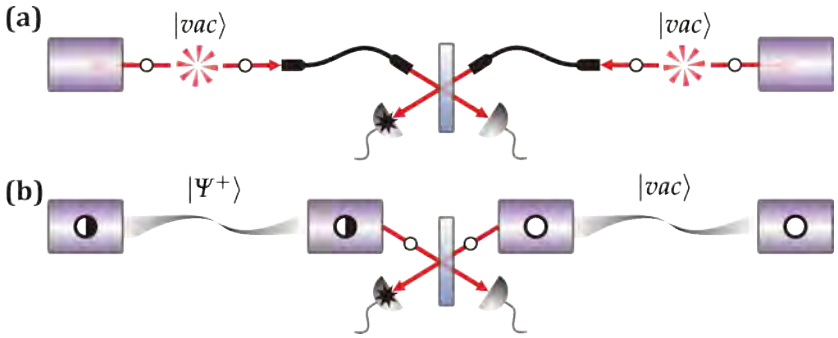

Figure 3.3: **(a)** An entanglement generation attempt is accepted due to a dark count although no photon pairs were produced, creating a vacuum state. **(b)** An additional dark count during connection leads to the separable, non-vacuum state $|10\rangle$.

count. To see this, note that a generation dark count results in a vacuum state. Connecting this with the ideal Bell-type state (3.1) in the presence of a memory imperfection or a generation dark count may result in a separable output state, e.g. $|10\rangle$ as illustrated in Fig. 3.3, leading to an error in F. Since the event requires a generation dark count and an error in connection, the error term must be proportional to $\epsilon\,\bar{n}_{dc}$, with $\epsilon = |c_1|^2, |c_2|^2, |c_3|^2$, or $\bar{n}_{dc}$. However, comparing with the errors considered in previous sections we now require generation of only $L/L_0 - 1$ photons rather than L/L_0, and therefore this error term is also enhanced by a factor of $1/p$, so that the total order of magnitude of the term is $\epsilon\,\bar{n}_{dc}/p$. Relative to the error terms considered previously there is a factor of $\bar{n}_{dc}/p$, which amounts to enhancement if the dark count probability is higher than the pair-production probability and to suppression in the reverse case. On the other hand, the cross term involving a generation dark count and an additional excitation from entanglement generation or the cross terms not involving generation dark counts require generation of L/L_0 photons. They are therefore of order ϵ^2 and can be safely neglected in both cases.

We conclude that the analytical results derived in the previous sections provide a full description of the postselected fidelity whenever the production rate for photon pairs during entanglement generation is significantly higher than the dark count rate of the detectors. By comparing (3.41) to (3.39) we see that for number resolving detectors, the ratio of the error from finite initial squeezing to the error from generation dark counts is $\eta_{gen}(1-\eta_{con})p/\bar{n}_{dc}$. Since typically $\eta_{gen} \ll 1$ and $\eta_{con} \lesssim 0.5$, it will be advantageous to make p larger than $\bar{n}_{dc}$ to increase the rate. We are then only making a minor error by neglecting cross terms. The same holds true for bucket detectors.

3.3.2 Application to specific memories

We now check the analytical results of the previous section against numerical simulations. The results for dark count and initial squeezing errors are independent of the memories and apply to any repeater with the architecture in Fig. 3.1. To verify them, we perform numerical simulations for ideal memories which simply map the input to the output mode $\hat{a}_1' = \hat{a}_1$. To verify the memory re-

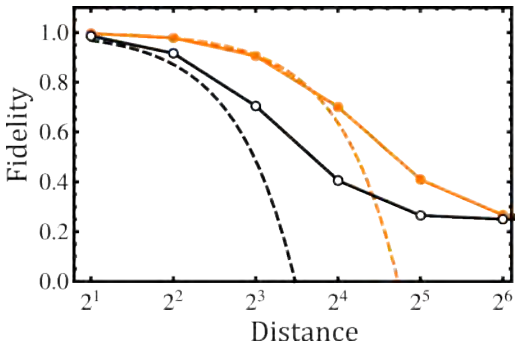

FIGURE 3.4: Finite initial squeezing. The fidelity is plotted for transmissivities $\eta_{gen} = 0.05$, $\eta_{con} = 0.9$, and pair-production probability $p = 2.5 \times 10^{-3}$ using counting (dots) and bucket (circles) detectors. Dashed lines show analytical approximations.

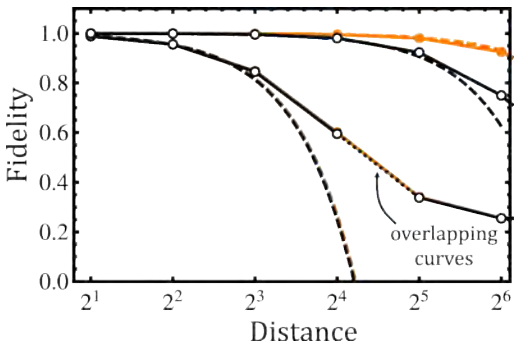

FIGURE 3.5: Detector dark counts. The fidelity is plotted for $\eta_{gen} = 0.05$, $\eta_{con} = 0.9$, and $\bar{n}_{dc} = 2.5 \times 10^{-5}$ using counting (dots) and bucket (circles) detectors. The two upper curves are for dark counts in connection, the lower for generation. Dashed lines show analytical approximations.

sults, we pick two specific ensemble-based quantum memories. One we denote the one-pass memory. It has been demonstrated by Julsgaard *et al.* in an experiment [74] which provided the initial motivation for the work presented in this chapter. The other, here denoted the two-pass memory, has been proposed by Muschik, Hammerer *et al.* [93] and may be regarded as an improved version of the one-pass scheme. We investigate how well these two memories perform in our quantum repeater architecture.

Our numerical results are obtained by computing $\hat{\rho}_n$ by means of the generating function for specific values of the parameters of the system, as explained in Sec. 3.2. In doing so, there is no need to treat errors independently but we do have to restrict the dimension of $\hat{\rho}_n$, because it is not practical to work with large matrices for runtime reasons. This is equivalent to imposing a cut-off on the number of excitations and it means that our numerical results are only valid when errors do not introduce too many extra excitations into the system. In our simulations we take a maximal excitation number of 2 so that $\hat{\rho}_n$ is a 9x9 matrix. Our results can then be considered exact as long as the probability of creating three or more excitations is negligible. Since the repeater protocol breaks down as soon as the probability to have one superfluous excitation becomes appreciable, this condition is well fulfilled in practice.

Squeezing, dark counts and cross terms

In Fig. 3.4 and Fig. 3.5 we display respectively the effect of finite initial squeezing and of detector dark counts on the postselected fidelity as a function of L/L_0. We take the transmission to be 5% for generation and 90% for swapping. Realistically, the latter number should be somewhat lower, since it includes the detector efficiency which is typically less than 60% (c.f. Sec. 2.3). Taking an optimistic value allows us to see a clear difference between photon-counting and bucket detectors. The pair-production probability is taken to be 2.5×10^{-3} and

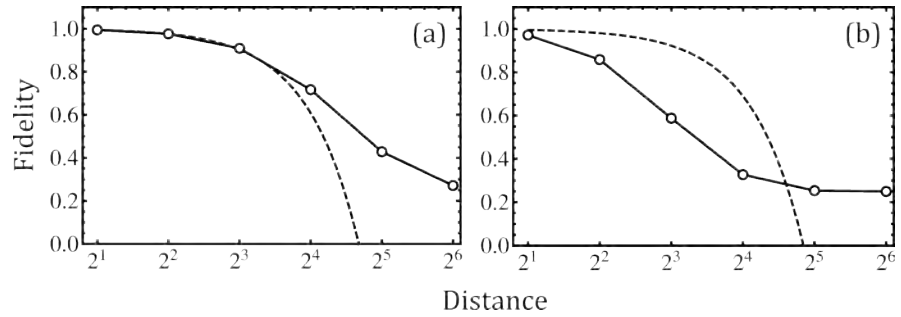

Figure 3.6: Significance of perturbation cross terms. The fidelity is plotted for $\bar{n}_{dc} = 10^{-5}$ in all detectors in the two cases $p = 10^{-4}$ (a) and $p = 10^{-6}$ (b). When $\bar{n}_{dc} > p$, a large discrepancy is observed between the numerics and the analytical approximation omitting perturbation cross terms (dashed line).

the average number of dark counts per detection event is 2.5×10^{-5}, which corresponds to μs-pulses and a realistic dark count rate of 25 Hz [60]. We note that the numerical results are well described by the analytical approximations from Sec. 3.3.1 in the regime where errors are small. The perturbative approach breaks down when errors become larger than $\gtrsim 20\%$. We also note that for finite initial squeezing or dark counts during entanglement swapping, a repeater with number resolving detectors performs better than one with bucket detectors, wheras for dark counts during entanglement generation, counting makes no difference (the curves for counting and non-counting overlap in Fig. 3.5). This can be understood since squeezing and connection dark counts introduce extra excitations into the repeater, e.g. as illustrated in Fig. 3.2a where one segment is in the state $|11\rangle$. These errors will lead to connection events in which two excitations are read out and impinge on the same detectors. When detectors are number resolving such errors can therefore be suppressed. Dark counts during generation on the other hand do not change the total number of excitations in the repeater. It is evident from the plots that there is a maximal distance beyond which the repeater protocol is no longer feasible. Say that a certain minimal fidelity F_{min} for the final pairs is desired. When F_{min} is larger than the breakdown threshold for the perturbative approximation, we can use our analytical expressions to find the maximal distance. E.g. from (3.40) the limit imposed by generation dark counts is

$$(L/L_0)^2 \leq \frac{\eta_{gen}(1 - F_{min})}{6(1 - \eta_{gen})\bar{n}_{dc}} \tag{3.42}$$

for number resolving detectors. With $F_{min} = 80\%$ and the numbers above this gives $L \lesssim 8L_0$ (c.f. Fig. 3.5).

As mentioned in the previous section, different error sources can only be treated independently in perturbation theory when the pair-production rate in entanglement generation is higher than the detector dark count rate. This is demonstrated in Fig. 3.6 where we plot F in the two cases $\bar{n}_{dc} < p$ and $\bar{n}_{dc} > p$ for a setup with dark counts in all detectors. We see that the analytical approximation obtained by adding the error terms (3.34) and (3.40) is valid only when $\bar{n}_{dc} < p$ as expected.

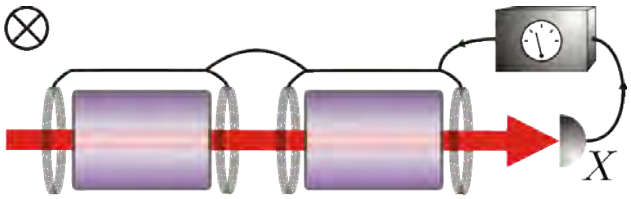

FIGURE 3.7: One-pass memory storage setup. Two atomic ensembles are placed in a magnetic field, with their collective spin strongly polarised along the field. The atoms are traversed once in the plane perpendicular to the field by a light beam. The light is measured by homodyne detection and a magnetic feedback is applied to the atoms. As a result the state of the light field is transferred onto the atomic spin.

One-pass memory

The setup for storage of a quantum state of light in the one-pass memory realised by Julsgaard *et al.* is shown in Fig. 3.7. The memory consist of two ensembles of Caesium atoms contained in glass cells at room temperature placed in a bias magnetic field. The initial state of the atoms is strongly spin polarised, such that the Holstein-Primakoff approximation applies and the ensembles can be described in a harmonic oscillator formalism. The collective spins of the two ensembles are coupled in such a way that the atomic system can be described by collective canonical operators $\hat{X}_A$, $\hat{P}_A$ with the usual commutator $[\hat{X}_A, \hat{P}_A] = i$. The incoming light field is also strongly polarised and described by operators $\hat{X}_L$, $\hat{P}_L$. The light beam passes through both ensembles, and subsequently the quadrature $\hat{X}_L$ is measured by homodyne detection. Based on the outcome, a feedback magnetic pulse is applied to the atoms using coils as shown. The interaction of the light field with the collective atomic spin leads to the Bogoliubov transformation (see Ref. [74] for details)

$$\hat{a}'_A = (1 - \frac{\kappa g}{2})\hat{a}_A + \frac{\kappa g}{2}\hat{a}^\dagger_A + \frac{1}{2}(\kappa + g)\hat{a}_L - \frac{1}{2}(\kappa - g)\hat{a}^\dagger_L, \tag{3.43}$$

where the atomic output mode is denoted by a prime, κ is the light-atom coupling strength and g is the feedback gain. Only the storage step was demonstrated in the experiment [74]. To implement entanglement swapping (Fig. 3.1b) the atomic state must be retrieved back onto a light field. In order to investigate whether the one-pass memory is suitable for use in the repeater, we simply assume perfect readout, i.e. we take $\hat{a}'_L = \hat{a}'_A$ for the output light. From the expression (3.43) it is clear that the memory is never perfect, since for any non-zero choice of κ and g the output light contains some mixing in of the input atomic mode. However, if the atomic mode is squeezed prior to storage, this noise can be suppressed. Assuming that the variance of $\hat{X}_A$ is squeezed by a factor s, and putting $\kappa = g = 1$ the Bogoliubov transformation of a full state transfer becomes

$$\hat{a}'_L = \frac{\sqrt{s}}{2}(\hat{a}_A + \hat{a}^\dagger_A) + \hat{a}_L. \tag{3.44}$$

This is now on the form (3.22) and it is easy to read off the coefficients. In Fig. 3.8 we show the postselected fidelity found by numerical simulation based on (3.44) and compare to the analytical expressions (3.34) and (3.35). Again, we

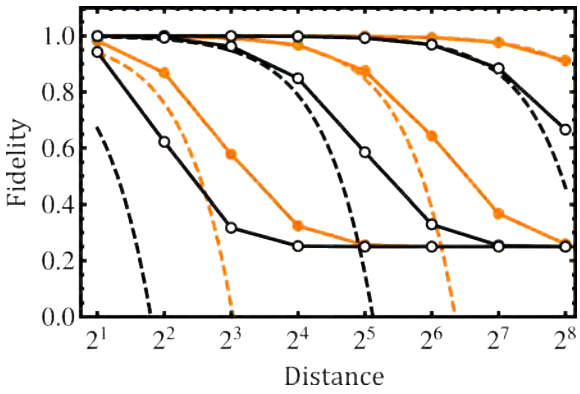

Figure 3.8: One-pass memory. The fidelity is plotted for $\eta_{gen} = 0.05$, $\eta_{con} = 0.9$, and squeezings of (left to right) 10 dB, 30 dB and 50 dB in the case of counting (dots) and bucket (circles) detectors. Dashed lines show analytical approximations.

find good agreement between numerical and analytical results. Note that the value of the atomic spin squeezing in the plot is extremely high. This is because it turns out that the one-pass memory performs poorly for moderate or low squeezing. Using (3.35) we can estimate the squeezing required to implement a repeater with L/L_0 segments and reach a minimal final fidelity F_{min} with number resolving detectors. We get

$$s_{min} = \frac{1 - F_{min}}{3(1 - \eta_{con})(L/L_0)^2}. \tag{3.45}$$

For $L = 8L_0$, $\eta_{con} = 0.9$ and $F_{min} = 80\%$ the squeezing is $s_{min} \approx -20\,\text{dB}$. This value is far beyond what can be achieved experimentally at the moment. The best reported atomic spin squeezing lies in the range of 3-6 dB [1, 80, 127, 130]. We therefore conclude that the one-pass memory is not suitable for implementation of a repeater with the architechture of Fig. 3.1 and hence in particular of the DLCZ protocol.

Two-pass memory

The two-pass memory proposed by Muschik *et al.* is depicted in Fig. 3.9. It consists of a single atomic ensemble, e.g. of alkali atoms, which is contained in a glass cell at room temperature placed in a bias magnetic field, just like for the one-pass setup. The spin of the atoms is strongly polarised, and they interact with a strongly polarised beam of light. Storage and retrieval are achieved by the same geometry. The light beam traverses the cell twice in orthogonal directions and passes through a quarter wave plate in between. Both light and atoms are described by canonical operators $\hat{X}_L$, $\hat{P}_L$ and $\hat{X}_A$, $\hat{P}_A$. The interaction Hamiltonian is $\hat{X}_A\hat{X}_L$ in the first pass of the light pulse and $\hat{P}_A\hat{P}_L$ in the second, and the overall interaction Hamiltonian becomes $\hat{X}_A\hat{X}_L + \hat{P}_A\hat{P}_L \propto \hat{a}_A^\dagger\hat{a}_L + \hat{a}_A\hat{a}_L^\dagger$. As a result of this beam-splitter like interaction, the state of the light and the state of the collective atomic spin are swapped. The process is governed by the light-atom coupling strength κ. In the absence of losses a full state transfer through the

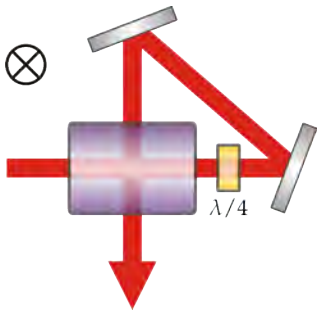

FIGURE 3.9: Two-pass memory setup. An atomic ensemble is placed in a magnetic field, with the spin of the ensemble strongly polarised along the field. The atoms are traversed twice in orthogonal directions in the plane perpendicular to the field by a light beam. As a result, the light polarisation state can be stored in or retrieved from the atomic spin.

memory is described by the Bogoliubov transformation (see Ref. [93] for details)

$$\hat{a}'_L = (e^{-\kappa^2} - 1)\hat{a}_L - e^{-\kappa^2/2}\sqrt{1 - e^{-\kappa^2}}\hat{a}_A + e^{-\kappa^2/2}\hat{a}_L^{ret}, \tag{3.46}$$

where $\hat{a}_L$, $\hat{a}'_L$ are the stored and retrieved light modes, $\hat{a}_A$ is the input atomic mode and $\hat{a}_L^{ret}$ is the input mode of the retrieval light pulse. It is clear from (3.46) that the mapping from input to output light becomes perfect for large coupling strength $\kappa \gg 1$. Even for finite κ, (3.46) is a passive transformation and hence the fidelity is not degraded by storage and retrieval. Only the repeater rate is affected by κ in the absence of loss. The important error parameter in the two-pass setup is technical. In a real implementation, light will be reflected at the walls of the cell. Reflections occurring between the two passes of the pulse introduce an active part to (3.46) and degrades the fidelity. The exact form of the Bogoliubov transformation including reflection losses becomes fairly complicated, involving 22 independent modes [94], and we will not reproduce it here. For small losses and a fixed value of κ the expressions can be simplified. In experiment, the light-atom coupling strength is restricted by spontaneous emission, and in the following we will take an optimistic value of $\kappa = 2$. To first order in the cell wall reflection coefficient ξ we then find $c_1 = c_2 = 0$, and $c_3^2 \approx 0.9\xi$ for the parameters of (3.22). The maximal reflection that can be tolerated in a repeater with L/L_0 segments and number resolving detectors for a desired final fidelity F_{min} is found from (3.35)

$$\xi_{max} = \frac{1 - F_{min}}{0.9 \times 6(1 - \eta_{con})(L/L_0)^2}. \tag{3.47}$$

For $L = 8L_0$, $\eta_{con} = 0.9$ and $F_{min} = 80\%$ the tolarable reflection is $\xi_{max} \approx 6 \times 10^{-3}$. This is a reasonable value, which can be obtained experimentally with present technology. Based on this analysis we thus conclude that the two-pass memory shows significantly more promise for implementation of a quantum repeater than the one-pass memory. In Fig. 3.10 we plot the postselected fidelity for the two-pass memory together with our perturbative approximations (3.34) and (3.35) for three different values of the reflection coefficient ξ.

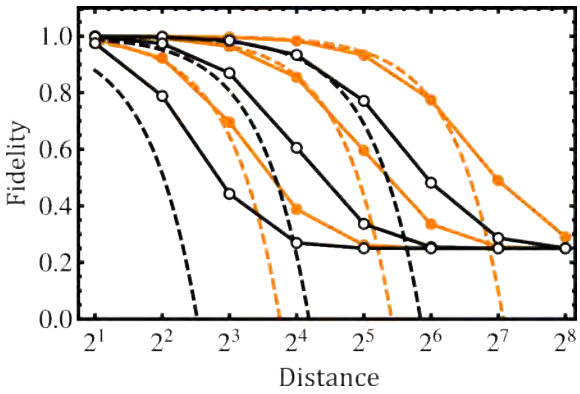

Figure 3.10: Two-pass memory. The fidelity is plotted for $\eta_{gen} = 0.05$, $\eta_{con} = 0.9$ and (from left to right) $\xi = 10^{-2}$, 10^{-3}, and 10^{-4} in the case of counting (dots) and bucket (circles) detectors. Dashed lines show analytical approximations.

3.3.3 Rate

We will now derive an expression for the rate as a function of distance for a fixed final fidelity. When dark counts or active memory imperfections are present, there is a maximal distance beyond which it is no longer possible to reach high fidelity without purification (c.f. (3.42) and (3.47)). We will focus on the case where there are no dark counts and the memories are passive (losses being the only memory imperfections), such that there is no limit on the distance. Unwanted excitations during entanglement generation are then the only imperfections which degrade the fidelity. They can be suppressed by decreasing the pair-production probability p, and the scaling of the rate is determined by the trade-off between p and the fidelity, since the rate is proportional to p. In the course of our derivation we show how detector inefficiency during entanglement connection cause a rapid growth of the vacuum component, significantly suppressing R.

To reach good final fidelity, the probability for unwanted excitations to occur must be kept low, and they do not influence the rate much. We therefore first determine the rate for fixed, very small p neglecting extra excitations. We then combine this result with (3.38) and (3.39) which determine the scaling of p with distance. For small p, the state produced by entanglement generation is ideal $\hat{\rho}_0 = |\Psi^{\pm}\rangle\langle\Psi^{\pm}|$, where the sign of the phase depends on which detector clicks. Since loss is the only error, we expect the state after n connections to take the form

$$\hat{\rho}_n = \lambda_n |\Psi^{\pm}\rangle\langle\Psi^{\pm}| + (1-\lambda_n)|vac\rangle\langle vac|, \tag{3.48}$$

where λ_n is a number and $\lambda_0 = 1$. If this parametrisation of $\hat{\rho}_n$ is conserved under entanglement connection (Fig. 3.1b), then it follows by induction that it is correct. It is not difficult to prove that this is indeed the case, and for number-resolving detectors one finds

$$\lambda_{n+1} = \frac{\lambda_n}{2 - \eta_{con}\lambda_n}, \tag{3.49}$$

which has the solution

$$\lambda_n = \frac{1}{\eta_{con} + 2^n(1-\eta_{con})}. \tag{3.50}$$

From this expression we see that the vacuum component of $\hat{\rho}_n$ grows rapidly with the number of connections when entanglement swapping is lossy, e.g. for imperfect detectors. The growing vacuum component suppresses the probability for connection causing the rate to drop. This is a major drawback of the single-rail architecture and in part motivated the more recent dual-rail schemes of Refs. [27, 72, 114], which do not have this problem. From (3.48) the success probability for connection is

$$p_{n+1} = \lambda_n^2(\frac{1}{2}\eta_{con} + \frac{1}{2}\eta_{con}(1-\eta_{con})) + \lambda_n(1-\lambda_n)\eta_{con} = \frac{1}{2}\eta_{con}\lambda_n^2/\lambda_{n+1}, \tag{3.51}$$

and the probability for successful postselection is $p_{ps} = \frac{1}{2}\lambda_n^2$. For $p \ll 1$, the success probability for entanglement generation is $p_0 = 2\,\eta_{gen}p$. The rate, which is given by (2.53), then becomes

$$R = \tau^{-1} p\,\eta_{gen}\,\eta_{con}^n \frac{2}{3^{n+1}}\lambda_0^2 \prod_{i=1}^{n}\lambda_i. \tag{3.52}$$

This expression can be put on a closed form as follows. We start by turning the product into a sum by taking the logarithm

$$\ln\prod_{i=1}^{n}\lambda_i = -\sum_{i=1}^{n}\ln\left(\eta_{con} + 2^i(1-\eta_{con})\right). \tag{3.53}$$

The sum can be estimated by taking the integral

$$\int_1^{n+1}\ln\left(\eta_{con} + \gamma 2^x(1-\eta_{con})\right)dx, \tag{3.54}$$

where we have introduced a constant γ. By adjusting γ we make sure that the integral agrees with the sum above in the limits where the sum can be easily evaluated. The integral gives

$$n\ln\eta_{con} + \frac{1}{\ln 2}\left[\mathrm{Li}_2\left(\frac{2\gamma(\eta_{con}-1)}{\eta_{con}}\right) - \mathrm{Li}_2\left(\frac{2^{n+1}\gamma(\eta_{con}-1)}{\eta_{con}}\right)\right], \tag{3.55}$$

where Li_2 is the dilogarithm [91]. Because $\mathrm{Li}_2(0) = 0$, the integral equals the sum (3.53) for $\eta_{con} \to 1$. The sum is also easily evaluated in the (unphysical) limit $\eta_{con} \to 0$. In that case it evaluates to

$$\sum_{i=1}^{n}\ln 2^i = \frac{\ln 2}{2}n(n+1). \tag{3.56}$$

Using that $\mathrm{Li}_2(x)$ tends to $-\pi^2/6 - \ln^2(-x)/2$ for large negative values of x [91], the limit of the integral (3.54) is

$$\frac{\ln 2}{2}n\left[n + \frac{2\ln(2\gamma)}{\ln 2}\right]. \tag{3.57}$$

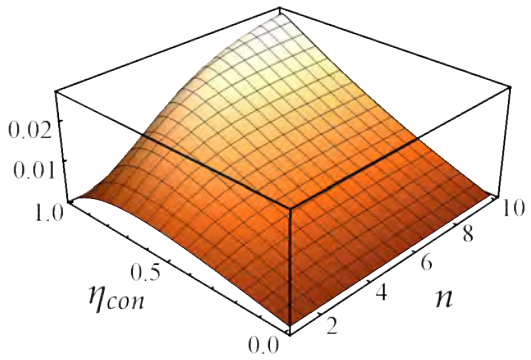

Figure 3.11: Plot of the relative error (LHS − RHS)/LHS where LHS and RHS refer to (3.58).

For the limit of the integral to equal that of the sum, we require $\gamma = 1/\sqrt{2}$. Inserting γ in (3.55) and taking the exponential, our best estimate for the product in (3.52) is

$$\prod_{i=1}^{n} \lambda_i \approx \frac{1}{\eta_{con}^n} \exp \frac{1}{\ln 2} \left[\mathrm{Li}_2 \left(\frac{2^{n+1/2}(\eta_{con}-1)}{\eta_{con}} \right) - \mathrm{Li}_2 \left(\frac{2^{1/2}(\eta_{con}-1)}{\eta_{con}} \right) \right]. \quad (3.58)$$

It can be verified numerically that this is in fact a very good approximation in our range of interest. Fig. 3.11 shows a plot of the relative error as a function of n and η_{con}. For $n \leq 10$ the relative error never exceeds 2.7% for any value of η_{con}. Using (3.58) together with $L/L_0 = 2^n$ and $\lambda_0 = 1$, we obtain the rate

$$R = \frac{2}{3} \tau^{-1} p \, \eta_{gen} (L/L_0)^{-\log_2 3} R' \quad (3.59)$$

with

$$R' = \exp \left[\frac{1}{\ln 2} \mathrm{Li}_2 \left(\frac{\eta_{con}-1}{\eta_{con}} \frac{\sqrt{2}L}{L_0} \right) - \frac{1}{\ln 2} \mathrm{Li}_2 \left(\frac{\eta_{con}-1}{\eta_{con}} \sqrt{2} \right) \right]. \quad (3.60)$$

This expression still contains the parameter p, which for a fixed final fidelity F_{min} depends on the number of segments L/L_0. The transmission coefficients η_{gen} and η_{con} can also be rewritten in terms of more physically tangible quantities. In generation, the important losses are due to attenuation in the fibres and inefficient detectors. Hence $\eta_{gen} = \eta_{det} \, e^{-L_0/2L_{att}}$, where η_{det} is the detector efficiency and L_{att} is the fibre attenuation length. In connection, $\eta_{con} = \eta_{mem}\eta_{det}$ where η_{mem} is the efficiency of the memories. Recalling that $\tau = L_0/c$ is the classical communication time and making use of (3.39) to eliminate p we finally get the rate for the case of number-resolving detectors

$$R = \frac{1}{9} \frac{1-F_{min}}{1-\eta_{mem}\eta_{det}} \frac{c}{L_0} \frac{\eta_{det} e^{-L_0/2L_{att}}}{1-\eta_{det} e^{-L_0/2L_{att}}} (L/L_0)^{-2-\log_2 3} R', \quad (3.61)$$

where R' is still given by (3.60). For bucket detectors, a similar derivation can be carried out with the λ_n-recursion modified slightly since events where two photons reach the same detector are now accepted as successful swapping events.

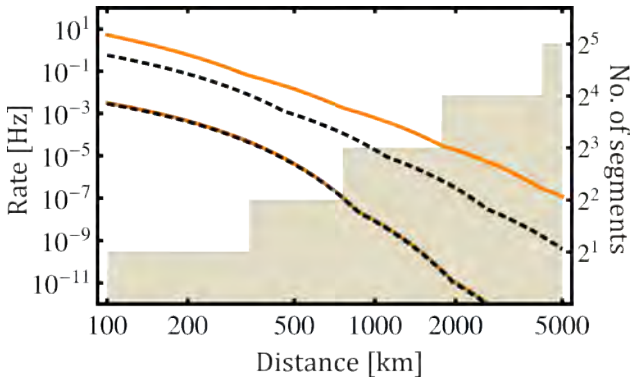

FIGURE 3.12: Rate R vs. distance L using number-resolving (solid orange) and bucket (dashed black) detectors plotted for $F_{min} = 0.95$, $L_{att} = 20\,\text{km}$, perfect retrieval, and $\eta_{det} = 0.9$ (upper curves) and 0.1 (lower curves). The optimal number of segments is indicated by shading.

We find

$$R = \frac{1}{9}\frac{1-F_{min}}{1-\frac{1}{2}\eta_{mem}\eta_{det}}\frac{c}{L_0}\frac{\eta_{det}e^{-L_0/2L_{att}}}{1-\frac{1}{2}\eta_{det}e^{-L_0/2L_{att}}}(L/L_0)^{-2-\log_2 3/2}R' \tag{3.62}$$

with

$$R' = \exp\left[\frac{1}{\ln 2}\text{Li}_2\left(\frac{\eta_{mem}\eta_{det}-2}{\eta_{mem}\eta_{det}}\frac{\sqrt{2}L}{L_0}\right) - \frac{1}{\ln 2}\text{Li}_2\left(\frac{\eta_{mem}\eta_{det}-2}{\eta_{mem}\eta_{det}}\sqrt{2}\right)\right]. \tag{3.63}$$

We note that for the clock cycle period τ of the repeater to equal L_0/c, as we have assumed in (3.61) and (3.62), the memory write and readout times must be much shorter than L_0/c. A typical segment length is $L_0 = 100\,\text{km}$ and hence L_0/c is of order $500\,\mu\text{s}$. In recent experiments, write and readout times $< 1\,\mu\text{s}$ have been achieved [24, 30, 31, 43].

In an implementation, the base segment length L_0 should be optimised for the given L to maximise the rate. Fig. 3.12 shows a plot of the optimal rate for a target fidelity of $F_{min} = 95\%$, assuming perfect lossless memories ($\eta_{mem} = 100\%$), a fibre attenuation length of 20 km corresponding to standard telecom wavelengths, and detector efficiencies of $\eta_{det} = 90\%$ and 10%. When the detector efficiency is high, the rate is seen to be significantly enhanced by the use of number-resolving detectors. This can be understood as a consequence of the vacuum component of $\hat{\rho}_n$ growing faster with bucket detectors. In the connection of two segments each in the ideal entangled state $|\Psi^+\rangle$ it may happen that both excitations are retrieved. If only one click is detected, the connection is accepted but the resulting state is vacuum. With perfect number-resolving detectors, this can never happen while for bucket detectors it occurs even in the absence of any losses. Thus for good detector efficiency, the rate is improved by counting. As η_{det} decreases, the probability for two photons to reach a detector simultaneously becomes small and the advantage of counting disappears, the rates for number-resolving and bucket detectors being equal in the limit of low efficiency.

3.4 Conclusion

We have presented a thorough analysis of quantum repeaters based on the DLCZ architecture, taking into account losses, detector dark counts and quantum memory imperfections, and treating both number-resolving and bucket photodetectors. As a primary result of our analysis we have derived perturbative analytical expressions for the fidelity of the generated entangled states in terms of the distance and the memory parameters. The errors introduced by memory imperfections were found to scale quadratically with the number of repeater segments. The memories were described in terms of a general Bogoliubov transformation and hence our results apply to repeaters based on any type of memory for which the interaction is not more than quadratic in the mode operators. We have verified our analytical results by comparison to numerical simulations and found good agreement in the range where perturbation theory applies.

As evidenced by Fig. 3.12, although the DLCZ protocol achieves sub-exponential scaling, the absolute rate at distances of order 1000 km is very low for realistic photodetector efficiencies. In addition, we have not treated interferometric instability errors and we have not considered the finite coherence time of realistic quantum memories. More recent dual-rail protocols [72, 114, 145] and protocols based on multi-mode memories [119] promise significantly better rates and better tolerance for multi-photon and phase errors. Multiplexing has been proposed to boost rates for low memory coherence times [35].

Chapter 4

An ensemble-based repeater with fluorescence detection

An important limiting factor in existing proposals for atomic-ensemble-based quantum repeater schemes is the efficiency of entanglement swapping. The swapping procedure requires conversion from excitations stored as atomic spin-waves to light, followed by single-photon detection. Neither retrieval of stored excitations nor single-photon detection is very efficient. As discussed in Sec. 2.3.2, typical detector efficiencies are not larger than 60% and there are technical as well as fundamental [56] limits to the retrieval efficiency. In practice, the combined retrieval and photodetection efficiency is on the order of ten percent [26, 30]. This severely limits the communication rate. A very rough indication of the improvement gained by increasing the swapping efficiency can be obtained from the rate expression (2.53). If the combined retrieval and detection efficiency is increased from η_{swap} to η'_{swap}, then when $\eta_{swap}, \eta'_{swap} \ll 1$ the corresponding swapping success probabilities obey $p'_i/p_i \approx \eta'_{swap}/\eta_{swap}$, and the improvement in rate is therefore at least $(L/L_0)^{\log_2(\eta'_{swap}/\eta_{swap})}$. The actual gain may be significantly larger, since improving p_i can affect $p_{i+1}, p_{i+2}, \ldots$, and since higher swapping efficiency implies that smaller values for L_0 become favorable.

In this chapter we present an ensemble-based quantum repeater, which circumvents the problems of low retrieval and single-photon detection efficiencies by storing multiple excitations in a single atomic ensemble. Manipulation of multiple qubits encoded as collective excitations within one atomic ensemble has been proposed as a basis for quantum computing [20, 21]. Our scheme builds on a similar idea. With only a single ensemble at each repeater node, entanglement swapping is achieved by linear transformations of the internal atomic states followed by measurements of the populations of certain levels via fluorescence detection. Taking such an approach, the efficiency of entanglement swapping can be notably enhanced. Fluorescence detection can have very high efficiency and at the same time allows to distinguish between one, two, or a few atoms, i.e. to resolve the number of stored excitations. For trapped ions, incredibly impressive efficiencies up to 99.99% have been experimentally demonstrated [95], and fluorescence measurements have been proposed for efficient photon count-

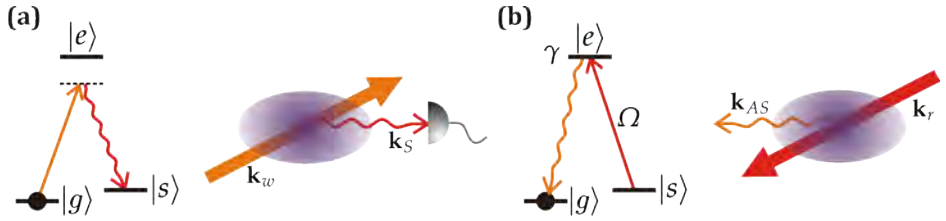

FIGURE 4.1: **(a)** Spin-wave creation. A weak, off-resonant write pulse with wave vector $\mathbf{k}_w$ induces a transition from $|g\rangle$ to $|s\rangle$ associated with emission of a Stokes photon detected in the mode $\mathbf{k}_S$. **(b)** Spin-wave retrieval. A resonant control field with wave vector $\mathbf{k}_r$ excites any atom in $|s\rangle$ to $|g\rangle$ and it decays to $|g\rangle$ emitting an anti-Stokes photon in the mode $\mathbf{k}_{AS}$.

ing by absorbing the photons in ensemble-based memories for light [68, 70]. Our scheme can be implemented both with single-rail and a dual-rail entangled states, and we evaluate the improvement in rate by comparison to the single-rail proposal of Duan, Lukin Cirac and Zoller (DLCZ) [41] and the dual-rail proposal of Jiang *et al.* [72]. For clarity we focus on single-rail in most of the chapter and discuss dual-rail only toward the end.

The work presented in this chapter was done in collaboration with Liang Jiang and Alexey V. Gorshkov in the research group of Prof. Mikhail D. Lukin at Harvard University. It has been published in Ref. [13].

4.1 Review of spin-wave generation and retrieval

Since entanglement both in our new as well as in previous ensemble-based repeaters is based on generation of atomic spin-waves by Raman scattering, and since we will be gauging our protocol against protocols based on retrieval of these spin-waves, we start out the chapter by a brief review of Raman scattering spin-wave generation and retrieval.

4.1.1 Generation

The fundamental building block of previous protocols is an ensemble of atoms with a Λ-type level structure interacting with light. Each ensemble functions as a quantum memory for atomic excitations which are generated by detecting light scattered off the atoms and later retrieved onto light fields. An atomic excitation heralded by light is generated by the setup in Fig. 4.1a. All the atoms are initially prepared in the ground state $|g\rangle$ by optical pumping. The ensemble is said to be strongly spin-polarised (c.f. Sec. 2.1.4). To write an excitation onto the atoms, a weak off-resonant light pulse is applied to the *g-e* transition, inducing Raman scattering into the meta-stable level $|s\rangle$. Emission of a Stokes photon on the *e-s* transition is associated with the transfer of one atom from $|g\rangle$ to $|s\rangle$, thus the interaction of the atoms with the light produces pairs of atomic and photonic excitations and the detection of a Stokes photon heralds the creation of an atomic excitation. When the Stokes photon is detected in the far field, it

carries no information about which particular atom was excited and hence the excitation is coherently shared by all the atoms. If $\mathbf{k}_w$ is the wave vector of the write control pulse and a Stokes photon is emitted with wave vector $\mathbf{k}_S$, then the atomic state becomes [63, 111]

$$e^{i(\mathbf{k}_w-\mathbf{k}_S)\cdot\mathbf{x}_1}|s,g,\ldots g\rangle+\cdots+e^{i(\mathbf{k}_w-\mathbf{k}_S)\cdot\mathbf{x}_N}|g,\ldots g,s\rangle, \tag{4.1}$$

where N is the total number of atoms and $\mathbf{x}_j$ is the position of the j'th atom. This state is referred to as an atomic spin wave with momentum $\Delta\mathbf{k}=\mathbf{k}_w-\mathbf{k}_S$. Focusing on a particular direction for the emitted Stokes light, we can associate a ladder operator $\hat{a}_{\mathbf{k}_S}$ with the Stokes light mode and we can define a collective operator describing excitations of the corresponding atomic mode

$$\hat{s}^\dagger_{\Delta\mathbf{k}}=\frac{1}{\sqrt{N}}\sum_{j=1}^{N}e^{i\Delta\mathbf{k}\cdot\mathbf{x}_j}|s\rangle_j\langle g|. \tag{4.2}$$

When acting on the collective ground state with all atoms in $|g\rangle$, this operator creates the spin wave (4.1). As in Sec. 2.1.4, we can think of $|g,\ldots,g\rangle$ as the "vacuum" state for the atomic system and $\hat{s}^\dagger_{\Delta\mathbf{k}}$ as a creation operator. The conjugate operator $\hat{s}_{\Delta\mathbf{k}}$ annihilates the vacuum. When the atomic ensemble has many atoms $N\gg 1$ and is strongly polarised (nearly all atoms in $|g\rangle$), then $\hat{s}_{\Delta\mathbf{k}}$ and $\hat{s}^\dagger_{\Delta\mathbf{k}}$ obey the usual canonical commutator relation

$$\begin{aligned}[\hat{s}_{\Delta\mathbf{k}},\hat{s}^\dagger_{\Delta\mathbf{k}}]&=\frac{1}{N}\sum_{j,k}e^{i\Delta\mathbf{k}\cdot(\mathbf{x}_k-\mathbf{x}_j)}[|g\rangle_j\langle s|,|s\rangle_k\langle g|]\\&=\frac{1}{N}\sum_j(|g\rangle_j\langle g|-|s\rangle_j\langle s|)\approx 1.\end{aligned} \tag{4.3}$$

Thus both light and atoms can be described in harmonic oscillator formalism. In terms of the creation and annihilation operators, the interaction of a single pair of light and atomic modes is described by the interaction Hamiltonian [41, 63, 111]

$$H=\kappa(\hat{a}_{\mathbf{k}_S}\hat{s}_{\Delta\mathbf{k}}+\hat{a}^\dagger_{\mathbf{k}_S}\hat{s}^\dagger_{\Delta\mathbf{k}}), \tag{4.4}$$

where the coupling strength κ depends on the intensity and detuning of the write pulse, the transition strengths for the *g*-*e* and *e*-*s* transitions and the number of atoms. The complete light-atom interaction will involve many terms of this form corresponding to different Stokes light modes. Referring to Sec. 2.1.3, we see that (4.4) generates two-mode squeezing between the light mode $\hat{a}_{\mathbf{k}_S}$ and the atomic spin-wave mode $\hat{s}_{\Delta\mathbf{k}}$. The interaction in Fig. 4.1a therefore exactly describes a source of the type considered in Sec. 2.4.2 and it can be used to generate entanglement between two separated atomic ensembles as discussed there.

4.1.2 Retrieval

It is a remarkable property of spin waves generated by Raman scattering that although there is no preferred direction for the Stokes light, once a Stokes photon has been detected, the corresponding spin wave can be retrieved onto an

anti-Stokes photon in a well defined mode. The spin wave may be thought of as somewhat analogous to the interference pattern recorded in a classical hologram. When the hologram is illuminated with the appropriate reference beam the recorded signal is reconstructed (note though, that the spin-wave 'hologram' is destroyed by the retrieval process and can only be read out once). Retrieval of a stored spin wave onto light is achieved by the setup in Fig. 4.1b. A resonant retrieval pulse is applied to the *s*-*e* transition and drives transfer of atoms from $|s\rangle$ back to the ground state $|g\rangle$. The spin-wave is retrieved onto the anti-Stokes light emitted on the *e*-*g* transition. If the atoms have not moved prior to retrieval, such that their state is still given by (4.1), and if the retrieval control pulse has wave vector $\mathbf{k}_r$, then the amplitude for emission of an anti-Stokes field with wave vector $\mathbf{k}_{AS}$ is proportional to [111]

$$\sum_j e^{i(\Delta\mathbf{k}+\mathbf{k}_r-\mathbf{k}_{AS})\cdot\mathbf{x}_j}. \tag{4.5}$$

In the limit of very many atoms this function resembles a δ-function, i.e. for large N it is strongly peaked around $\Delta\mathbf{k}+\mathbf{k}_r-\mathbf{k}_{AS}=0$. The anti-Stokes fields emitted by different atoms interfere destructively for all directions except $\mathbf{k}_{AS}=\Delta\mathbf{k}+\mathbf{k}_r$ leading to collective enhancement of emission into this mode. This makes it possible to collect the retrieved spin-wave with good efficiency and is one of the main results motivating the use of atomic ensembles in quantum repeaters. In many cases however, the required storage time (between the write and retrieval pulses) in a repeater setup is much larger than the time scale associated with atomic motion. Hence the atoms move to new positions $\mathbf{x}'_j$ before retrieval, and the expression (4.5) has to be replaced by

$$\sum_j e^{i\Delta\mathbf{k}\cdot\mathbf{x}_j}e^{i(\mathbf{k}_r-\mathbf{k}_{AS})\cdot\mathbf{x}'_j}. \tag{4.6}$$

This is in general not peaked for any direction of $\mathbf{k}_{AS}$, retrieval is no longer directional. An exception is found when $|\Delta\mathbf{k}|\times\Delta x\ll 1$ where Δx is the length scale of the atomic motion. In that case directionality is restored with constructive interference in the direction $\mathbf{k}_{AS}=\mathbf{k}_r$. For this reason, when writing a spin-wave into the ensemble it is often preferable work with a system where levels $|g\rangle$ and $|s\rangle$ are close in energy and to collect Stokes photons emitted in (or very close to) the forward direction, i.e. in the same direction as the write pulse[1]. The spin wave created when $\mathbf{k}_w=\mathbf{k}_S$ is called the flat or symmetric spin wave, because it is described by the operator

$$\hat{s}^\dagger=\hat{s}^\dagger_{\Delta\mathbf{k}=\mathbf{0}}=\frac{1}{\sqrt{N}}\sum_{j=1}^{N}|s\rangle_j\langle g| \tag{4.7}$$

with equal coefficients on all terms.

[1]For a discussion of how atomic motion and deviations from forward collection impact memory coherence times, see the reviews Ref. [111] and Ref. [63].

Retrieval efficiency

The efficiency of spin-wave retrieval has been studied in detail by Gorshkov *et al.* [57]. It depends crucially on the optical depth seen by the retrieved field in the direction $\Delta\mathbf{k} + \mathbf{k}_r$ of constructive interference. The optical depth $d_\mathbf{k}$ along $\mathbf{k}$ is defined such that $\exp(-d_\mathbf{k})$ is the total attenuation incurred by light passing through the atomic ensemble, i.e. $d_\mathbf{k}$ is the length of the ensemble measured in units of the attenuation length for the light. The picture of directional retrieval described above is only valid when $d_{\Delta\mathbf{k}+\mathbf{k}_r} \gg 1$. In this case retrieval is efficient and most of the spin wave is emitted into the mode $\Delta\mathbf{k} + \mathbf{k}_r$. When $d_{\Delta\mathbf{k}+\mathbf{k}_r} \lesssim 1$, retrieval is inefficient. Only a small fraction of the spin wave is emitted in the expected mode and directionality is lost. In particular, for retrieval from the symmetric spin wave, the efficiency is [57]

$$\eta_{ret} = 1 - e^{-d/2}\left[I_0(d/2) + I_1(d/2)\right], \tag{4.8}$$

where $d = d_{\mathbf{k}_r}$ and I_m denotes the modified Bessel function of the first kind. The time it takes for a spin wave to leave the atomic ensemble also depends on the optical depth. When $d_{\Delta\mathbf{k}+\mathbf{k}_r}$ is high, the retrieved field moves at the group velocity. In terms of the retrieval-laser Rabi frequency Ω, the length l of the ensemble in the direction of the retrieval pulse, and the decay rate γ of the excited level $|e\rangle$, the group velocity for the symmetric spin wave is given by [57, 63]

$$v_g = \frac{\Omega^2 l}{\gamma d}, \tag{4.9}$$

provided that $\Omega \ll \gamma d$. On the other hand, when $d_{\Delta\mathbf{k}+\mathbf{k}_r}$ is small the spin wave decays without directionality. For low optical depth, collective effects are negligible and the spin wave then decays at the rate of a single emitter, which is Ω^2/γ for weak driving $\Omega \ll \gamma$ (such that the excited level population vanishes and adiabatical elimination applies). We will make use of this later in Sec. 4.3.

4.2 New protocol

The setup for our protocol is shown in Fig. 4.2. A channel of length L is divided into segments of a shorter length L_0. At each node a single atomic ensemble, which serves as a quantum memory, is located. In the first step of the protocol each ensemble is entangled with both its left and right neighbours. In subsequent steps, the entanglement is swapped to longer distances by local operations and measurements on the atomic ensembles. The atoms are assumed to have the level structure depicted in Fig. 4.3. Each atom has a reservoir level $|g\rangle$, two metastable storage levels $|s_1\rangle$, $|s_2\rangle$, two excited states $|e_1\rangle$, $|e_2\rangle$, and cycling transitions which allow the populations of the storage levels to be measured. Connecting to previous ensemble-based repeaters based on Λ-scheme atoms, one may think of Fig. 4.3 as a double Λ-system – one for each storage level – with two additional cycling transitions [111]. Strictly speaking, given sufficient control over the manifold of stable states, a single cycling transition and a single Λ-type transition is sufficient to implement the scheme, however the configuration in Fig. 4.3 is

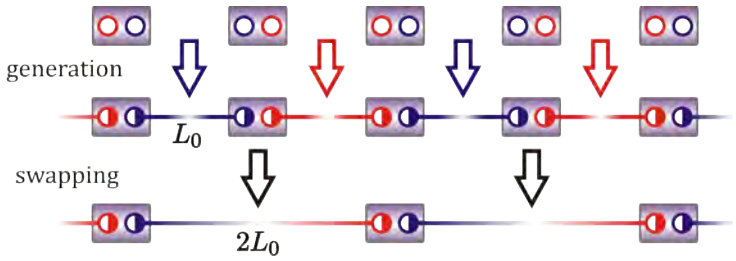

FIGURE 4.2: Repeater structure. One atomic ensemble with two atomic storage levels (indicated by red and blue circles) make up each node. In the first step of the protocol, neighbouring nodes are entangled using the same levels at every other segment. Entanglement on the two storage levels is established asynchronously. In subsequent steps, distant nodes are connected by entanglement swapping.

illustrative. As discussed in Sec. 4.5 below, the proposed level scheme can be implemented in alkali-metal or alkaline-earth-metal atoms.

Entanglement generation

The entanglement generation procedure in the present protocol makes use of the same basic process as previous ensemble-based repeaters, namely creation of atomic spin-waves heralded by detection of scattered Stokes photons. However, in contrast to previous schemes, several spin-waves are now stored in the same atomic ensemble. For an ensemble which is not an end-node, entanglement generation proceeds as follows. The ensemble is first entangled with, say it's left neighbour using the storage level $|s_1\rangle$. In each ensemble a weak laser pulse is applied to the g-e_1 transition, inducing Raman scattering into $|s_1\rangle$ (as in Fig. 4.1a). The forward-scattered Stokes light on the e_1-s_1 transition is collected and transmitted to a balanced beam splitter, where the signals from the two ensembles are mixed and then measured by single-photon detectors (as in Fig. 2.8). When one and only one click is registered, entanglement generation is considered successful. The process is then repeated to entangle the ensemble with its right neighbour, this time applying a laser on the g-e_2 transition and collecting Stokes photons on the e_2-s_2 transition. For a repeater with just two segments (i.e. with three nodes) in the ideal limit of very weak write pulses where events with multiple excitations can be neglected, entanglement generation creates the state

$$(\hat{s}^\dagger_{s_2,3} + \hat{s}^\dagger_{s_2,2})(\hat{s}^\dagger_{s_1,2} + \hat{s}^\dagger_{s_1,1})|vac\rangle, \tag{4.10}$$

where $\hat{s}^\dagger_{s_i,j}$ with $i = 1,2$ and $j = 1,2,3$ creates a symmetric spin wave stored in level $|s_i\rangle$ of the ensemble at the j'th node, c.f. the definition (4.7).

Entanglement swapping

Entanglement swapping at a given node is achieved by first applying a beam-splitter-like transformation on the atoms which takes

$$|s_1\rangle \to \frac{1}{\sqrt{2}}(|s_1\rangle + |s_2\rangle) \qquad |s_2\rangle \to \frac{1}{\sqrt{2}}(|s_1\rangle - |s_2\rangle). \tag{4.11}$$

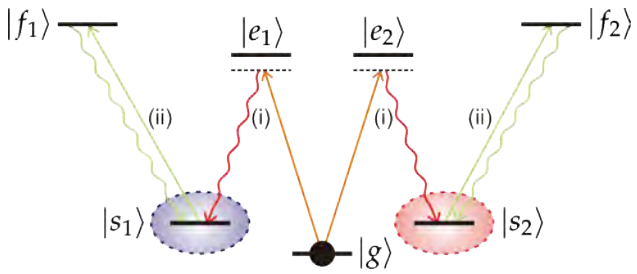

Figure 4.3: Atomic level scheme. Spin-waves stored in the encircled meta-stable levels are generated via the Raman transitions (i). The populations of the storage levels can be measured using the cycling transitions (ii). Prior to entanglement generation, all atoms in an ensemble are initialised in the ground state, and the system remains close to this fully polarised state at all times.

From the definition of $\hat{s}$ it follows that the transformation also acts as a beam splitter between the two spin-wave modes $\hat{s}_{s_1}$, $\hat{s}_{s_2}$. Depending on the actual implementation of the idealised level scheme we are considering here, such a transformation can be implemented in various ways. If $|s_1\rangle$ and $|s_2\rangle$ are stored in magnetic hyperfine sublevels in e.g. alkali atoms, the rotation can be driven by microwaves or radio-frequency magnetic fields and can be implemented with high fidelity [88]. Alternatives in other systems include Raman transitions, optical $\pi/2$-pulses and STIRAP[2]. Once (4.11) has been performed, the populations of the storage levels $|s_1\rangle$, $|s_2\rangle$ are measured by fluorescence detection. A classical laser is applied in turn to each cycling transition (Fig. 4.3) and part of the scattered light is collected. The average collected signal is directly proportional to the population of the storage level. Successful swapping is conditioned on the detection of a single atom in one and only one of the storage levels. Upon such an event at the 2nd node, the state (4.10) is projected to an entangled state of the 1st and 3rd nodes

$$(\hat{s}^\dagger_{s_2,3} + \hat{s}^\dagger_{s_1,1})|vac\rangle. \tag{4.12}$$

In the absence of imperfections, the probability for a single atom to fluoresce is $2N/(4N-1) \sim 1/2$, and hence the maximal success probability for swapping is $1/2$, just as for previous ensemble-based repeaters. However, here no retrieval of the spin waves is required and fluorescence detection can have very high efficiency compared to single-photon detection.

4.3 Purification by interrupted retrieval

Because the same atoms encode several logical spin waves and because of the use of fluorescence detection for entanglement swapping, several issues not present in previous protocols must be considered in our scheme. Here we deal with the fact that fluorescence detection does not selectively detect the symmetric spin wave but rather any atomic excitations in the storage levels $|s_1\rangle$, $|s_2\rangle$. This is in contrast to schemes based on retrieval. Fig. 4.4 illustrates the difference. During entanglement generation, only a small fraction η_{col} of the scattered Stokes

[2] Stimulated Raman Adiabatic Passage, see [48].

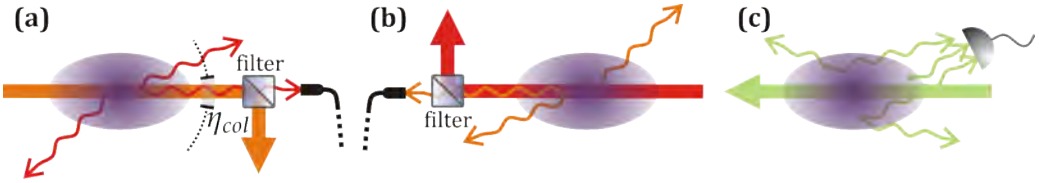

FIGURE 4.4: **(a)** Only a fraction η_{col} corresponding to forward scattered light is detected during entanglement generation, but additional spin waves associated with scattering in other directions are also created. **(b)** Due to collective enhancement during retrieval, only the symmetric spin wave is retrieved into the detected mode. Other spin waves contribute very little to the detected signal. **(c)** In a fluorescence measurement, the is no preferred direction for the scattered light and all atomic excitations contribute equally to the detected signal.

light is collected, however scattering in other directions also occurs and associated atomic excitations are created. The probability to create an excitation in the symmetric spin-wave mode is $\eta_{col}q$ where q is the total probability to create an atomic excitation. In schemes based on retrieval, only excitations of the symmetric mode are detected during entanglement swapping, due to the collective nature of the retrieval process. The probability for erroneous multiple excitations is therefore $\eta_{col}q$. In a fluorescence measurement however, any population of the atomic storage levels will contribute to the detected signal. Excitations in modes other than the symmetric spin wave mode will effectively introduce dark counts during entanglement swapping, and the multiexcitation error probability is then q. Thus if no corrective measures are taken, to reach the same fidelity at a given distance with fluorescence detection instead of retrieval, q and hence the rate must be suppressed by a potentially very small factor of η_{col}.

We propose to overcome this problem by means of *purification by interrupted retrieval* (PIR). The idea is to make use of the dependence of the retrieval process on optical depth (as described in the previous section). If the optical depth is different for different modes, some spin waves may be retrieved with high and some with low efficiency when the retrieval control field is turned on. More importantly, for the efficiently retrieved spin waves the output field will move at the group velocity while spin waves for which retrieval is inefficient decay at the single emitter rate. The associated time scales for excitations to leave the atomic ensemble may potentially be very different. Imagine for example that the optical depth for forward retrieval of the symmetric spin wave is large $d \gg 1$. Then the decay rate of the symmetric spin wave under retrieval is $v_g/l = \Omega^2/\gamma d$ which is much slower than the single emitter rate Ω^2/γ. If the optical depths for all other modes are low (of order 1), the state of the ensemble can be 'purified' by turning on the retrieval field for a duration T such that

$$\frac{\gamma}{\Omega^2} \lesssim T \ll \frac{\gamma d}{\Omega^2}. \tag{4.13}$$

This will allow any excitations in the non-symmetric modes to escape, while only a small fraction of the symmetric spin wave is lost. Clearly there will be a trade-off between loss of the symmetric spin wave and suppression of the incoherent excitations. There are two contributions to the loss of the symmetric

spin wave. One is retrieval at the group velocity as already mentioned. The other is spontaneous decay into other directions due to the limited efficiency of the retrieval process for finite optical depth. As outlined in App. B.1, the total loss becomes

$$\frac{v_g T}{l} + \frac{v_g T}{l} e^{-\Omega^2 T/2\gamma} \left[I_0(\Omega^2 T/2\gamma) + I_1(\Omega^2 T/2\gamma) \right]. \tag{4.14}$$

This is upper bounded by twice the group-velocity loss $\delta = 2v_g T/l$ and approaches this value for small T, i.e. when the loss is small. In other modes, excitations decay at the single emitter rate $\Omega^2/\gamma = \delta d/2T$ and they are therefore suppressed by a factor of $\eta_{col} + (1-\eta_{col})e^{-\delta d/2}$, where we take into account that a fraction η_{col} of the emission does not escape. For small η_{col}, reducing the multiexcitation error probability in our scheme to $O(\eta_{col} q)$ requires that the factor $e^{-\delta d/2} \sim \eta_{col}$. The penalty for suppressing the error is hence a loss

$$\delta \sim -\frac{2\ln(\eta_{col})}{d}. \tag{4.15}$$

The loss δ can be regarded as an inefficiency of entanglement swapping, equivalent to retrieval and single-photon detection losses in schemes based upon retrieval. However, δ scales with $1/d$ whereas retrieval losses according to (4.8) scale as $1/\sqrt{d}$ for large d. For good optical depth $d \gtrsim 100$ and a collection efficiency η_{col} at or above the percent level, δ is below ten percent. This is significantly less than the losses incurred with retrieval, where the single-photon detection losses alone are typically more than 50%. Hence, PIR allows our scheme to retain high efficiency of entanglement swapping, while exhibiting the same scaling of multiexcitation errors as previous schemes.

A configuration where only one retrieved mode sees high optical depth while all other modes see optical depths of order 1 seems difficult to achieve for an atomic ensemble in free space. One might hope to reduce the number of modes with high optical depth by creating an ensemble with a large aspect ratio. However, this is not sufficient. The quantity $\mathcal{F} = A/l\lambda$, where A is the ensemble cross section and λ is the wavelength of light, is called the Fresnel number. The picture of retrieval presented in Sec. 4.1 and the formula (4.8) for the efficiency are derived in the limit of large Fresnel number $\mathcal{F} \gg 1$, where an effective one-dimensional treatment can be carried out [57, 63]. As we estimate in App. B.3, for large Fresnel number there are too many modes propagating near-parallel with the ensemble axis and PIR does not work. On the other hand, for $\mathcal{F} \sim 1$, the one-dimensional treatment breaks down [121] and spin-waves with different $\mathbf{k}$-vectors begin to couple. Thus, the need to suppress the optical depth for all but one mode means that PIR comes with the added experimental complication of placing the ensemble within some kind of photonic structure. One possibility is to enclose the ensemble in a cavity. The effective optical depth of the cavity mode is then enhanced by a factor of the cavity finesse, which can be made much larger than 1. When the unmodified optical depth is close to 1, the desired configuration is achieved. Another possibility is to place an elongated ensemble inside a photonic crystal which has a band gap in the density of states. For example, the ensemble can be placed inside a single-mode hollow-core photonic crystal fibre [3, 32]. Such a fibre supports a single guided mode propagating

along the fibre axis but exhibits a gap in the density of states, suppressing any near-parallel modes [36, 47, 105, 108]. Only the guided mode and modes with large transverse components are present. If the ensemble is optically dense on-axis but sufficiently elongated to be optically thin in the transverse direction, the desired configuration is again attained.

4.4 Bounds on the number of atoms

Several imperfections in our scheme lead to bounds on the number of atoms employed at each ensemble. The use of fluorescence detection for entanglement swapping leads to an upper bound, because measurements will exhibit many dark counts if the number of atoms in the reservoir state $|g\rangle$ is too large [68, 70]. Lower bounds arise because entanglement across neighbouring segments is encoded in the same atoms, and hence the state of one segment may be disturbed by attempts to establish entanglement in another segment. Here we consider two such effects. One is spin-wave mismatch. For an ensemble which is already part of one entangled link, attempts to establish an additional link may remove atoms from the existing spin-wave, causing the sets of atoms entangled 'to the left' and 'to the right' to be different. The other is measurement-induced dephasing. The presence or absence of a spin-wave slightly alters the excitation probability in the entanglement generation step, and hence generation attempts yield information about the atomic state causing a dephasing of existing entangled links.

4.4.1 Upper bound

For simplicity we drop subscripts in the following, since the left and right halves of the level scheme Fig. 4.3 are identical. Population in the reservoir can contribute to dark counts during fluorescence detection in two ways. Either through off-resonant scattering on the $g \leftrightarrow e$ transition of light from the probe field, which is resonant with the cycling transition. Or through population transfer into $|s\rangle$ induced by the probe. Except when the branching ratio β for decay from $|e\rangle$ to $|s\rangle$ is tiny, the latter of these provides a more severe restriction on the atom number, because it is amplified by subsequent resonant scattering. To simplify our analysis we assume that the $g \leftrightarrow e$ and cycling transitions have the same dipole moment, such that we can associate a single Rabi frequency Ω_p with the probe field, and that the $|e\rangle$- and $|f\rangle$-levels all decay at the same rate γ. We denote the frequency difference between the $g \leftrightarrow e$ and cycling transitions by $\Delta = \omega_{sf} - \omega_{ge}$. The fluorescence scattering rate r and the scattering rate r' from $|g\rangle$ into $|s\rangle$ are then given by

$$r = \frac{\gamma\Omega_p^2}{\gamma^2 + 2\Omega_p^2} \quad \text{and} \quad r' = \frac{\beta\gamma\Omega_p^2}{4\Delta^2}, \tag{4.16}$$

for Δ much larger than both Ω_p and γ, which is a reasonable assumption in the atoms we consider for implementations of the scheme. The rates r and r' determine the measurement duration, and the amount of population transfered

from reservoir to storage level during a measurement, respectively. The time required to faithfully detect a single excitation in one of the storage levels via fluorescence detection is $m/\eta'_{col}\eta_{spd}r$ where m is the desired average number of measured photons[3], η'_{col} is the collection efficiency for fluorescence detection, and η_{spd} is the single photon detection efficiency. The expected number of logical dark counts (one logical count being a detected signal corresponding to one atom in the storage level) equals the amount of population transferred during the measurement, which is

$$\bar{n}_{dc} = \frac{Nr'm}{\eta'_{col}\eta_{spd}r} = \frac{m\beta}{\eta'_{col}\eta_{spd}}\frac{\gamma^2 + 2\Omega_p^2}{4\Delta^2}N, \tag{4.17}$$

where N is the number of atoms. Since there is a limit on the tolerable error, we see from this expression that N is bounded from above. Clearly, it is desirable to implement our scheme in a system where Δ can be made large, such that high N and thus high optical depth d can be reached without introducing too many dark counts.

4.4.2 Lower bound

Next we turn to spin-wave mismatch. If for a given repeater node one entangled link has been established using e.g. $|s_1\rangle$, failed attempts at generating another link using $|s_2\rangle$ degrade the entanglement because such attempts may lead to scattering events incoherently projecting atoms into $|s_2\rangle$ or $|g\rangle$, removing them from the existing spin wave. If such an undesired scattering event occurs then, when a generation attempt finally succeeds, there will be atoms which are not part of the s_1-spin-wave but are part of the s_2-spin-wave (those projected into $|g\rangle$ in failed attempts). A mismatch between the spin waves means that even when a single atomic excitation is detected during entanglement connection, the resulting output state is not guaranteed to be entangled. If we assume that undesired population in $|s_2\rangle$ can be removed after failed generation attempts (for example by shelving in another metastable level or heating out of the trap holding the ensemble) only decay into $|g\rangle$ will lead to spin wave mismatch. We can estimate the error introduced by spin wave mismatch as follows. Each generation attempt projects $(1-\beta)q$ atoms from the first spin wave incoherently into $|g\rangle$. An average of $1/q\beta\eta_{col}\eta_{gen}$ attempts are needed to establish the second entangled link, where $\eta_{gen} = \eta_{spd}e^{-L_0/2L_{att}}$ is the combined transmission and detection efficiency in generation, with L_{att} the fibre attenuation length. Hence in total $(1-\beta)/\beta\eta_{col}\eta_{gen}$ atoms take part only in one spin wave. Assuming that the number of atoms is large such that $\beta\eta_{col}\eta_{gen}N \gg 1$, the probability to have a separable state after entanglement connection is of order

$$\frac{1-\beta}{\beta\eta_{col}\eta_{gen}}\frac{1}{N}. \tag{4.18}$$

[3]Each fluorescing atom scatters light at the same rate r. To achieve atom-number resolution, m must be chosen large enough for Poisson distributions with means $m, 2m, 3m, \ldots$ to be reliably distinguished.

We confirm this with a somewhat more thorough calculation in App. B.2. Note that the error probability is inversely proportional to N. Hence if the error must be kept below some threshold, this places a lower bound on N.

Even when the branching ratio β is very close to one, such that there is little spin wave mismatch, the interdependence of spin waves still impose a lower bound on N. The probability for an ensemble to emit a Stokes photon when illuminated by a write field of fixed power is changed by the presence of a spin wave, and hence attempts to establish a second entangled link with an ensemble that already has one link convey information about the state of the first link. This measurement induced dephasing is of relatively little importance compared to other problems which arise for small N, such as low optical depth.

4.4.3 Scaling

To understand how the bounds on N behave beyond the first entanglement swapping step, we need to understand how the dark count and spin-wave mismatch errors scale with the number of repeater segments.

Upper bound

Logical dark counts occurring during fluorescence detection are equivalent to detector dark counts occurring during entanglement connection in the DLCZ scheme. Assuming that we can distinguish the fluorescence signal of one atom from those of multiple atoms (i.e. we can count the fluorescing atoms), we therefore expect the dark count error to scale according to (3.35) as

$$6\frac{1-\eta_{fl}}{\eta_{fl}}\bar{n}_{dc}(L/L_0)^2 = \frac{3}{2}\,\frac{(1-\eta_{fl})m\beta}{\eta_{fl}\eta'_{col}\eta_{spd}}\,\frac{\gamma^2+2\Omega_p^2}{\Delta^2}\,N(L/L_0)^2, \tag{4.19}$$

where (4.17) was used and η_{fl} is the efficiency of fluorescence detection (i.e. if an atomic excitation is present the probability to detect it is η_{fl}).

Lower bound

The scaling of the mismatch error can be estimated as follows. Assuming that errors are small and add under connection, the mismatch error after n swapping steps must be twice the error after $n-1$ steps plus additional mismatch introduced due to failed swapping events at previous levels. If the success probability for entanglement connection is close to $1/2$, then the total number of entanglement generation attempts necessary to generate a pair at level $n-1$ is roughly $(1/2)^{n-1}$ times the number of attempts required to create a pair of length L_0. We now let E_n denote the mismatch error in a pair at level n without any neighbours, and E'_n the error in a pair at level n when one neighbouring pair at the same level has also been generated. The latter error obeys

$$E'_n = 2E'_{n-1} + 2^{n-1}E_0, \tag{4.20}$$

and the initial condition $E'_0 = E_0$. Rewriting the recursion in terms of the variable $2^{-n}E'_n$, the solution is easily found to be $E'_n = (1 + \frac{1}{2}n)2^n E_0$. For $n > 0$, we have $E_n = 2E'_{n-1}$ and hence

$$E_n = (n+1)2^{n-2}E_1 = \frac{1}{4}(L/L_0)\log_2(2L/L0)E_1. \tag{4.21}$$

The error E_1 after a single entanglement swapping step is given by (4.18). Thus

$$E_n = \frac{1-\beta}{4\beta\eta_{col}\eta_{gen}}\frac{1}{N}(L/L_0)\log_2(2L/L0). \tag{4.22}$$

4.5 Results and implementations

We now estimate the improvement in rate achieved by our scheme, assuming an implementation where the upper and lower bounds on N are compatible with each other and where the upper bound is compatible with good optical depth, making PIR possible. We then go on to discuss actual systems in which such an implementation may be possible below.

4.5.1 Rate improvement

Assuming the bounds on N are sufficiently wide apart, the dominant errors come from multiple excitations of the symmetric spin wave mode introduced during entanglement generation. In terms of error scaling our single-rail protocol is then equivalent to the DLCZ protocol, but with the efficiency of entanglement swapping set by spin-wave loss during PIR and the fluorescence detection efficiency rather than by retrieval and single-photon detection efficiencies. We can therefore use the results from Sec. 3.3.3 for the repeater rate if we substitute the appropriate value for the connection efficiency η_{con} in the new scheme. For the DLCZ protocol, the connection efficiency is given by

$$\eta_{con} = \eta_{spd}\,\eta_{ret} = \eta_{spd}\left(1 - e^{-d/2}\left[I_0(d/2) + I_1(d/2)\right]\right), \tag{4.23}$$

where the expression (4.8) for the retrieval efficiency was used. In the new scheme, the connection efficiency is

$$\eta_{con} = \eta_{fl}\left(1 + 2\ln(\eta_{col})/d\right), \tag{4.24}$$

where we have used (4.15) and η_{fl} is the efficiency of fluorescence detection. Fluorescence detection allows to distinguish between one or more excitations, and we assume the single-photon detectors to be number resolving as well, since we are then comparing against the best-case scenario for the DLCZ protocol. From (3.61) the rate scales as

$$\begin{aligned} R = \frac{1}{9}\frac{1-F_{min}}{1-\eta_{con}}\frac{c}{L_0}\frac{\eta_{spd}e^{-L_0/2L_{att}}}{1-\eta_{spd}e^{-L_0/2L_{att}}}(L/L_0)^{-2-\log_2 3} \\ \times \exp\left[\frac{1}{\ln 2}\mathrm{Li}_2\left(\frac{\eta_{con}-1}{\eta_{con}}\sqrt{2}L/L_0\right) - \frac{1}{\ln 2}\mathrm{Li}_2\left(\frac{\eta_{con}-1}{\eta_{con}}\sqrt{2}\right)\right], \end{aligned} \tag{4.25}$$

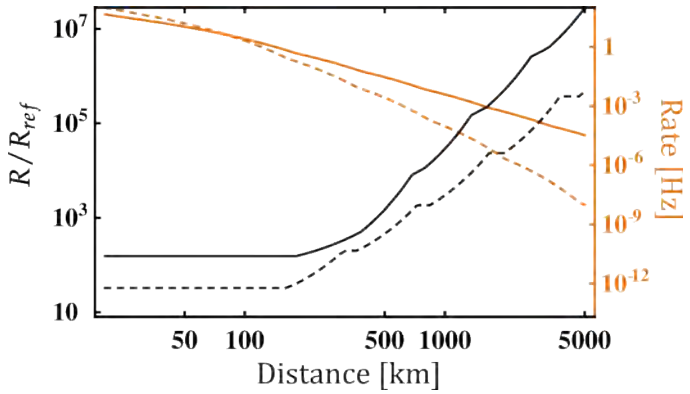

FIGURE 4.5: Black curves: Ratio of the rates in the dual- (solid) and single-rail (dashed) schemes with fluorescence detection and PIR to those of DLCZ and the scheme of Ref. [72], for $L_{att} = 20\,\text{km}$, $d = 100$, $\eta_{col} = 0.05$, $\eta_{spd} = 0.4$, $\eta_{fl} = 0.95$, and $F_{min} = 0.9$. Orange curves: The corresponding absolute rates in the new scheme.

where L_{att} is the attenuation length for transmission during entanglement generation, c is the speed of light, and F_{min} is the desired final fidelity. By plugging η_{con} into this expression, we can compare the rates of the DLCZ protocol and the present single-rail scheme.

We can make a similar comparison between a dual-rail protocol based on fluorescence detection and a retrieval-based dual-rail scheme. We consider the scheme of Jiang *et al.* [72]. This scheme uses four atomic ensembles at each repeater node and entanglement swapping is achieved by means of several polarising beam splitters and detection of two photons, as outlined in App. B.4. By extending the level scheme of Fig. 4.3 with two additional storage levels, it is possible (see the appendix) to find a mapping from the protocol of Ref. [72] to a protocol with a single ensemble at each node, replacing all linear optics transformations by atomic level transformations and single-photon detections by fluorescence detection. As in the single-rail case, the two protocols are then equivalent but with different connection efficiencies given by (4.23) and (4.24). At long distances the rate scales as [72]

$$R \propto \frac{1-F_{min}}{1-\eta_{con}} \frac{c}{L_0} \eta_{spd} e^{-L_0/2L_{att}} (L/L_0)^{-1-\log_2 3 - \log_2((2-\eta_{con})^4/\eta_{con}^2(3-2\eta_{con}))}. \quad (4.26)$$

Note that for good connection efficiency ($\eta_{con} \to 1$), apart from the common power of $\log_2(3)$, the rate of the dual-rail scheme scales as $1/L$ whereas the single-rail rate scales as $1/L^2$. Multiexcitation errors grow only linearly in the dual-rail scheme as opposed to quadratically for single-rail.

In Fig. 4.5 we show the ratio of the rates in the new single- and dual-rail schemes to those of the retrieval-based reference schemes as a function of distance for a fixed final fidelity of $F_{min} = 90\%$. We assume a fibre attenuation length of $L_{att} = 20\,\text{km}$, a collection efficiency during entanglement generation of $\eta_{col} = 0.05$, an optimistic optical depth of $d = 100$ and single-photon and fluorescence detection efficiencies of $\eta_{spd} = 0.4$ and $\eta_{fl} = 0.95$, which gives the values $\eta_{con} = 0.35$ and $\eta_{con} = 0.89$ for the reference and the new schemes respectively. The plot for

the single-rail protocols is based on the analytical expression (4.25) for the rate. The plot for the dual-rail protocols is not based directly on (4.26) but rather on numerical simulation using the same *Matlab* code as in Ref. [72]. This is slightly more accurate at short distances. The number of repeater segments is optimised in both cases. From the figure we see that significant improvements in rate can be obtained using the new protocol. At a distance of 1000 km, improvements of three and four orders of magnitude for the single-rail and dual-rail schemes respectively are found with the chosen parameters. Also note that since the plot is double logarithmic, the improvements are seen to scale polynomially (beyond the first few hundred km).

Since the rate gain obtained by the fluorescence-based repeater scheme relies on a boost in the efficiency of entanglement swapping and since η_{spd} is a crucial parameter for the efficiency of swapping in retrieval-based protocols, the advantage of the new scheme clearly depends on our assumptions about η_{spd}. As discussed in Sec. 2.3 current single-photon detectors generally have efficiencies below 60%. However new detectors in development may push this number upward. In App. B.5 we plot the rate gain for increasing values of η_{spd}. In addition we also vary L_{att}. Attenuation lengths in optical fibre are strongly wavelength dependent and L_{att} therefore depends on the choice of atomic species and transitions employed for Raman scattering during entanglement generation. These vary with implementation and are not necessarily the same for the fluorescence-based and retrieval-based schemes. In the appendix we verify that significant rate gains can be obtained even when the attenuation length of the fluorescence-based scheme is somewhat smaller than that of the reference schemes.

4.5.2 Implementation

Many experiments relevant to the realisation of ensemble-based quantum repeaters – for example demonstrations of teleportation and of storage and retrieval of quantum states of light – are based on alkali-metal (group I) atoms [24, 30, 31, 74, 117, 133]. Techniques for trapping and optically addressing alkali are well developed and well proven in the laboratory, and furthermore the level structure of alkali provides the necessary ingredients for implementation of our scheme. The magnetic sublevel manifold of the $S_{1/2}$ ground state contains enough stable levels, Raman transitions between these levels are possible by coupling to $P_{1/2}$ using the so-called D_1-line, and there are closed cycling transitions on the co-called D_2-line between $S_{1/2}$ and $P_{3/2}$. Alkali metals are thus obvious candidates for realising our protocol.

As explained above, to facilitate PIR our atomic ensembles must be confined within a photonic structure, such as a cavity or photonic crystal, enabling preferential coupling to a small set of optical modes during entanglement generation. In one recent experiment, an ensemble of ^{87}Rb atoms was confined in a hollow-core single-mode photonic crystal fibre and optical depths of $d = 30$ were measured with ~ 3000 atoms [3]. We therefore turn our attention to Rubidium. In Fig. 4.6 we sketch how the single-rail scheme may be implemented in ^{87}Rb. As a first check, we would like to know whether the bounds on N are reasonable. The

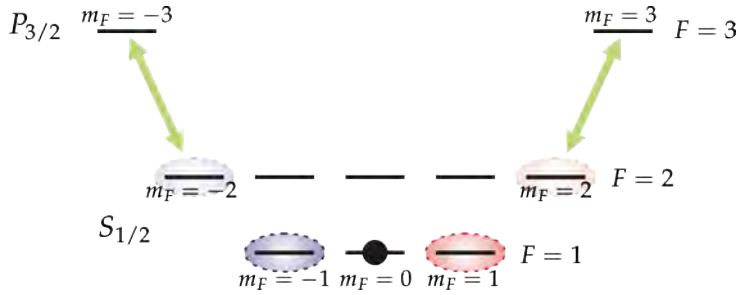

FIGURE 4.6: Possible implementation in ^{87}Rb. The reservoir and storage levels are sublevels of $S_{1/2}$ with hyperfine quantum numbers $|F = 1, m_F = 0\rangle$ and $|F = 1, m_F = \pm 1\rangle$ respectively. To perform a measurement on one of the storage levels, the population is transferred to $|F = 2, m_F = \pm 2\rangle$ and the transition to the sublevel $|F = 3, m_F = \pm 3\rangle$ of $P_{3/2}$ is cycled. Selective transfer of a single storage level from $F = 1$ to $F = 2$ can be achieved by Zeeman splitting of the transition in an applied magnetic field.

D_2-line which is used for the fluorescence measurements has natural line-width $\gamma = 6\,\text{MHz}$ [123]. The separation between this fluorescence transition and transitions involving the reservoir determines the detuning Δ relevant for the dark count probability (4.17). In this case the detuning is set by the difference between the hyperfine splittings in $S_{1/2}$ and $P_{3/2}$. The ground state splitting dominates, giving $\Delta \approx 6.8\,\text{GHz}$ [123]. Furthermore, with some improvement in collection efficiency it is conceivable to reach a regime with $\eta_{col} \sim 0.05$ corresponding to $d \sim 100$ with 2000 atoms. Assuming for simplicity that the collection efficiencies for Stokes light and fluorescence are equal $\eta'_{col} = \eta_{col}$, that $\beta = 0.5$, and taking $\eta_{spd} = 0.5$, $m = 20$ we can plug into (4.19) and (4.22). We find ~ 90 and ~ 1700; not a hugely encouraging result. The bounds are barely compatible and the upper bound imposed by dark counts is rather low. If one merely wishes to exceed the classical limit of fidelity $1/2$, the bounds may allow for a proof-of-principle experiment with about 1000 atoms (corresponding to $d = 50$), implementing a single entanglement swapping step over a short distance of $\sim 10\,\text{km}$. However, for fidelities $> 90\%$ the upper and lower bounds become incompatible and the upper bound becomes very restrictive $N < 350$, suppressing the optical depth. Rubidium 87 is thus not very well suited for realising the fluorescence-based repeater without any additional improvements of the scheme. Indeed this is true in general for the alkali. The bounds are relaxed slightly if ^{133}Cs is used, due to a larger hyperfine splitting in the ground state and slightly smaller D_2 linewidth [122], but they are still too restrictive to reach high fidelities. This impels us to look around for alternative atomic species.

Alkaline-earth-metal (group II) atoms have been proposed as attractive systems for quantum computation because they posses long-lived metastable excited states enabling encoding of qubits at optical frequencies with long lifetimes and allow decoupling of the nuclear spin and electronic states. [38, 58, 65, 125]. They are also good candidates in the present context. By storing spin-waves in the metastable levels while keeping the reservoir atoms in the ground state or vice versa, the cycling transition used to generate fluorescence can be separated from any transitions involving the reservoir by optical frequencies. This dramatically increases the upper bound on the atom number. As an example, let us consider

^{87}Sr. The nuclear spin of this isotope is $9/2$ and it therefore provides levels enough to implement both the single- and dual-rail variants of our scheme. The ground state is $(5s^2)^1S_0$, and the metastable levels $(5s5p)^3P_0$ and $(5s5p)^3P_2$ have lifetimes of $\sim 150\,\mathrm{s}$ and $\sim 520\,\mathrm{s}$ respectively [11, 141]. Various encodings of our protocol in ^{87}Sr are possible. The transition $(5s^2)^1S_0 \leftrightarrow (5s5p)^1P_1$ presents one choice of fluorescence transition. It has natural line-width $\gamma \sim 30\,\mathrm{MHz}$ and is very nearly cycling. Decay from $(5s5p)^1P_1$ to $(5s4d)^1D_2$ and $(5s5p)^3P_0$ is possible but the branching ratios are small, roughly equal to respectively[4] 10^{-5} and 10^{-8} [104, 115, 140]. If the reservoir is kept temporarily in $(5s5p)^3P_0$ during the fluorescence measurements, then the probe laser is detuned by $\Delta \sim 10\,\mathrm{THz}$ from the nearest transitions out of the reservoir [106]. In addition, the measurements do not induce population transfer from the reservoir into the cycling transition. This means that only off-resonant scattering can contribute to dark counts, and the factor $\beta m/\eta'_{col}\eta_{det}$ can be dropped from (4.17), relaxing the upper bound on N further. A possible channel for spin-wave generation is excitation and decay $(5s5p)^3P_0 \rightarrow (5s5p)^1P_1 \rightarrow (5s^2)^1S_0$. The very small branching ratio $1-\beta \sim 10^{-8}$ for back-decay from $(5s5p)^1P_1$ suppresses the mismatch error probability (4.18), reducing the lower bound on N. For a Strontium-based repeater over $L = 1000\,\mathrm{km}$ with $L/L_0 = 2^5$ segments, we estimate the upper bound on N to be around 5×10^7 and the lower bound to be of order 1. Such a repeater might thus be implemented with ensembles of 10^4 atoms, compatible with good optical depth.

4.6 Conclusion

In this chapter we have presented a new type of atomic-ensemble-based quantum repeater which in contrast to previous proposals has only one ensemble at each repeater node. Multiple excitations are stored as spin-waves within the same atomic ensemble and entanglement swapping is achieved by linear transformations of the atomic levels followed by fluorescence measurements of some of the level populations. This approach eliminates the need to retrieve spin-waves onto light and detect them as single photons. Because retrieval and single-photon detection are inefficient processes whereas fluorescence detection can have high efficiency, the result is a significant increase in the efficiency of entanglement swapping and hence a corresponding increase in the rate of entanglement distribution. By comparison to the DLCZ single-rail scheme [41] and the dual-rail scheme of Jiang *et al.* [72], potential improvements of respectively three and four orders of magnitude were found at a distance of 1000 km for a single-photon detection efficiency of 40% and fluorescence measurement efficiency of 95%.

Certain imperfections were discussed which are not present in retrieval-based schemes but affect our scheme due to the use of fluorescence measurements and the fact that spin-waves stored in the same atoms are not independent. We have

[4] The latter number is computed from the values of the electric dipole matrix element for $5s5p^1P_1 \rightarrow 5s^2{}^1S_0$ from Ref. [104] and the magnetic dipole matrix element for $^1P_1 \rightarrow {}^3P_0$ from Ref. [115].

shown how incoherent spin-waves created during entanglement generation can be removed via 'purification by interrupted retrieval' (PIR) provided that the atomic ensemble is enclosed in structure such as a hollow-core photonic crystal fibre or a low-finesse cavity which allows the optical depth for one mode of light to be enhanced. We have also seen that mismatch between spin-waves induced by Raman scattering during entanglement generation and dark counts induced by the probe laser during fluorescence measurements impose lower and upper bounds respectively on the number of atoms N for which our protocol can work reliably. We have estimated these bounds for implementations of the protocol in alkali (^{87}Rb) and alkali-earth (^{87}Sr) atoms. The upper bound was seen to be very restrictive for alkali due to an insufficient splitting between the cycling transition and transitions involving the reservoir state. On the other hand, the bounds for alkali earths were found to be much more favourable allowing implementation of a repeater over 1000 km with $N \sim 10^4$ atoms.

In the context of alkali-earths we note that alternative choices of reservoir and storage states should be considered and may have advantages. For example it may be beneficial to keep the reservoir in the ground state at all times since the ^3P-states are only metastable and slow decay may become important with large populations. If reservoir atoms can decay from ^3P into the cycling transition this will give rise to an additional source of dark counts. In that case, with a fluorescence detection time of 1 ms and $N \sim 10^4$ reservoir atoms the dark count probability becomes an appreciable 7%. By keeping the reservoir in the ground state such dark counts can be avoided. The storage levels can be held in $^3P_3$ and fluorescence measured on the transitions to $(5s4d)^3D_3$ or possibly $(5s5d)^3D_3$. One should also keep in mind that the smaller transition wavelengths in alkaline earths relative to alkali are less convenient for experiments and less compatible with optical fibre. In particular the attenuation length is therefore reduced, which impacts the rate, c.f. App. B.5.

Concerning implementation with alkali atoms, it may be possible to alleviate the strict upper bounds on N by state-selective trapping [69, 79, 85]. If atoms in the reservoir and storage states can be spatially separated prior to the fluorescence measurements, then the N-dependence of the dark count error probability could potentially be eliminated or at least significantly relaxed. Spatial separation could be achieved by independently movable potentials for the reservoir and storage states or (perhaps a more viable approach) by releasing atoms in the storage states to let them drop through a light sheet inducing fluorescence. Integrating such methods with the photonic structure required for PIR and maintaining high detection efficiency is a serious experimental challenge, but could render implementation of the fluorescence-based repeater with alkali atoms feasible, making it possible to take advantage of the well-developed experimental techniques and convenient wavelengths for these atoms.

The entanglement purification protocol proposed in Ref. [72] could in principle be integrated with our dual-rail scheme. However, the level scheme in Fig. B.1 would have to be extended by two additional storage states for every level of entanglement purification, significantly complicating the scheme. Atoms with high nuclear spin such as ^{87}Sr or ^{133}Cs do offer some room for this. A final interesting

perspective, which is facilitated by having only one ensemble at each repeater node, is to incorporate nonlinear interactions that could enable deterministic quantum gates, such as Rydberg blockade as proposed by Brion *et al.* [20].

Chapter 5

A hybrid repeater with cat states

The setting of the previous two chapters has been firmly in the discrete regime of quantum communication. We have been concerned with Fock-type excitations of photonic modes and atomic spin-waves and with discrete detection. In this chapter we cross over into the continuous variable regime to present a quantum repeater protocol which is most naturally described in the language of quadratures and coherent states. While having a definite continuous nature, the protocol retains one leg in the discrete regime, making use of single-photon detection to create entangled states which are then refined and connected using continuous variable techniques. It is in this sense of merging two regimes that the protocol is 'hybrid', as announced in the chapter title. The motivation for developing a repeater based on continuous variables is the same as what motivated the fluorescence based scheme in the previous chapter – better entanglement swapping efficiency. Quadrature measurements are performed using homodyne detection which with present technology offers much higher efficiency that the single-photon detectors employed by repeaters in the discrete variable regime. At the same time the entanglement generated in the protocol presented below is of a qualitatively different type, with non-orthogonal coherent states rather than Fock states as the basic building block, and hence offers a supplement to the kind of entanglement produced by discrete protocols. The states generated by the hybrid protocol have potential uses within existing continuous variable quantum computing schemes [83, 107]. Other hybrid quantum repeater schemes merging discrete and continuous variables have recently been proposed. Ref. [135] combines homodyning with non-linear interactions of light with single spins in cavities. Ref. [112] considers entangled states very similar to those of our scheme and relies on linear optics but makes use of single-photon counters for entanglement swapping.

The protocol presented here distributes entanglement in the form of squeezed variants of two-mode Schrödinger cat states. We introduce the notation $|\gamma'(\alpha,\theta)\rangle$

for the unnormalised two-mode cat state (2.26)

$$|\gamma'(\theta,\alpha)\rangle = e^{i\theta}|\alpha,\alpha\rangle + e^{-i\theta}|-\alpha,-\alpha\rangle, \tag{5.1}$$

where $|\alpha\rangle$ is a coherent state and θ is a phase. We will take α real throughout this chapter. We denote the normalised equivalent of $|\gamma'(\theta,\alpha)\rangle$ by the unprimed symbol $|\gamma(\theta,\alpha)\rangle$. Similarly, it will be useful in what follows to denote the unnormalised single-mode cat state by

$$|\xi'(\theta,\alpha)\rangle = e^{i\theta}|\alpha\rangle + e^{-i\theta}|-\alpha\rangle, \tag{5.2}$$

and its normalised equivalent by $|\xi(\theta,\alpha)\rangle$. For zero phase, we will use the shorthand $|\xi(\alpha)\rangle$. In the sections below we demonstrate that near-deterministic entanglement swapping of cat states using only linear optics and homodyning is possible, and we devise an efficient probabilistic scheme for generating states with potentially many photons and very good overlap with exact squeezed single- and two-mode cat states. Our generation scheme is reminiscent of that of Ref. [101], where creation of squeezed single-mode cat states from photon-number states was demonstrated, but does not require input states with more than a single photon in each mode and takes advantage of quantum memories to significantly increase the rate.

The proposal described in this chapter has been published in Ref. [14].

5.1 Generation of cat-states

Schrödinger cat states are notoriously hard to generate in the lab, in part because they are non-Gaussian. The output states of lasers are well described by coherent states, which have Gaussian phase space distributions (c.f. the wavefunction (2.28)). States with Gaussian phase space distributions are known as Gaussian states[1] and they remain Gaussian under many of the operations available in optics experiments, including any linear optical elements, such as beam splitters or phase shifters, as well as single- and two-mode squeezing and homodyne measurements. Any operation which can be described as a Bogoliubov transformation of the mode operators is Gaussian in the sense that it maps Gaussian states to Gaussian states [18]. Consequentially any interaction which is not more than quadratic in the mode operators cannot take a Gaussian to a non-Gaussian state. Higher-order processes which break Guassianity are typically weak. The optical cross Kerr effect for example can be harnessed to create cat states from coherent states by inducing a phaseshift dependent on the presence or absence of a trigger photon in another mode [51]. It is described by an interaction Hamiltonian proportional to a small third-order nonlinear susceptibility $\chi^{(3)}$, making it difficult to observe the effect [18, 54]. Gaussianity can also be broken by means of

[1] More precisely, Gaussian states are states $\hat{\rho}$ with a Gaussian Wigner function, defined as $W(x,p) = \frac{1}{2\pi}\int_{-\infty}^{\infty} e^{ipq}\langle x-q/2|\hat{\rho}|x+q/2\rangle dq$. The Wigner function is a full description of the state, equivalent to the density matrix and is a quasi-probability distribution over phase space. When $\hat{\rho}$ is a pure state, the marginals of W reproduce the distributions found from the wave function, e.g. $\int_{-\infty}^{\infty} W(x,p)dp = |\psi(x)|^2$. Wigner functions are covered in standard quantum optics text books, see e.g. [4, 52] and also [18].

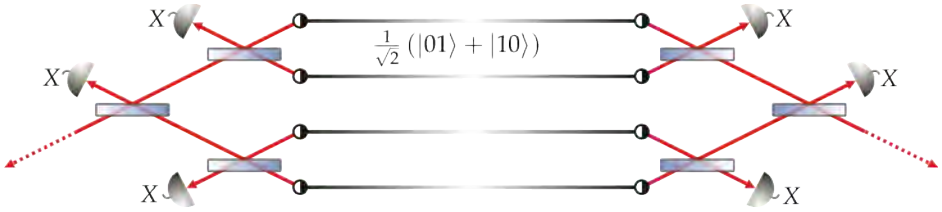

Figure 5.1: Growing approximate two-mode cats from single photons. Two Bell-like single-photon states are joined at both ends on balanced beam splitters, and the $\hat{X}$-quadrature is measured at one output of each beam splitter. When the sum of the outcomes is close to zero, the state is kept. The process is iterated, combining the output modes with those of a similar pair created in parallel.

non-Gaussian measurements, such as single-photon detection. Subtracting single photons from a weak squeezed vacuum state generates an approximate cat state, as demonstrated by several groups[2] [50, 96, 102, 126]. Unfortunately the average photon number is usually restricted to $\lesssim 1$. For larger amplitudes, the overlap of the generated states with cat states degrades (see e.g. [97] p. 35-36 for a discussion). Very recently cat states with a mean photon number of 2.75 have been generated by photon subtraction based on high-efficiency superconducting transition-edge detectors [49].

5.1.1 Scheme

Here we propose a scheme which allows generation of squeezed cat states from single photons by means of homodyne measurements and linear optics. Single-mode cats states can be generated from a supply of single-photon Fock states, and multi-mode entangled states can be generated from single photons delocalised between multiple modes. In the context of a quantum repeater protocol we are mainly interested in generating two-mode cats, but in principle any number of modes is possible. To create a two-mode cat, we start from single excitations delocalised between two spatially separated modes. Such entangled states were also employed in the previous two chapters and they can be generated using two sources of two-mode squeezed states as illustrated in Fig. 2.8. The sources can be realised by means of e.g. parametric down conversion crystals or ensembles of Λ-type atoms [15, 41, 119]. Following a single SPD click, the remaining two modes are projected to a Bell-like state

$$\frac{1}{\sqrt{2}}(|01\rangle + |10\rangle) + O(\sqrt{p}), \tag{5.3}$$

where the last term represents contributions from multiple excitations and is small when the pair production probability p is small, i.e. for weak squeezing. A setup of this type benefits from the discrete nature of single photons, with clicks heralding successful transmission. Given a supply of states of the form (5.3), a squeezed two-mode cat state is generated as illustrated in Fig. 5.1. Pairs of input

[2]Equivalently, cat states can be generated by squeezing of single-photon states (which are non-Gaussian).

states are combined on balanced beam splitters, and the $\hat{X}$-quadratures of two of the output modes are measured. The resulting state is kept, if the sum of the outcomes is sufficiently close to zero. That is, whenever the sum falls within an interval $[-\Delta, \Delta]$. Otherwise the state is discarded, and the process is restarted. Upon success, the protocol is iterated with the output states as new input states.

To see that this scheme can produce cat-like states, it is illuminating to first consider generation of a single-mode state in the ideal limit of perfect initial states and an infinitely narrow acceptance interval, $p \to 0$, $\Delta \to 0$. The single-mode setup corresponds to, say, the left half of Fig. 5.1 only. We start from two sources, each producing a single excitation $|1\rangle$ corresponding to the usual harmonic oscillator wavefunction

$$\psi_0(x) = \psi_{|1\rangle}(x) = \sqrt{2}\pi^{-1/4} e^{-\frac{1}{2}x^2} x. \tag{5.4}$$

The joint wavefunction for the two sources has the form $\psi_0(x)\psi_0(y)$. A balanced beam splitter[3] is then applied to the pair of modes x, y, followed by a measurement of y. If we require $y = 0$, corresponding to $\Delta \to 0$, the state is transformed to

$$\psi_1(x) \propto \left[\psi_0(\frac{x+y}{\sqrt{2}})\psi_0(\frac{x-y}{\sqrt{2}})\right]_{y=0} \propto e^{-\frac{1}{2}x^2} x^2. \tag{5.5}$$

The process is now iterated, combining this state with the output from another pair of sources, etc. Conditioning on zero for the $\hat{X}$-quadrature implies even parity for the photon number in the measured mode because all odd Fock state wavefunctions vanish at the origin as apparent from Fig. 2.2a. Since we start from an even number of photons, we therefore expect an output state containing only even photon numbers. Indeed what we get is essentially a cat state with even parity. After m iterations, the final normalised output state wavefunction becomes

$$\psi_m(x) = \Gamma(2^m + 1/2)^{-1/2} e^{-\frac{1}{2}x^2} x^{2^m}. \tag{5.6}$$

This expression is a symmetric, double-peaked function of x, which closely resembles a squeezed cat state wavefunction. In fact, $|\psi_m\rangle$ is very well approximated by $\hat{S}(2)|\xi(\mu_m)\rangle$, where

$$\mu_m = \sqrt{2^m + 1/2}. \tag{5.7}$$

The wavefunction of this state is

$$\langle x|\hat{S}(2)|\xi(\mu_m)\rangle = (2\pi)^{-1/4}(1 + e^{-2\mu_m^2})^{-1/2}\left(e^{-(x-\mu_m)^2} + e^{-(x+\mu_m)^2}\right). \tag{5.8}$$

Fig. 5.2a shows the similarity of (5.6) and (5.8). The fidelity $|\langle\psi_m|\hat{S}(2)|\xi(\mu_m)\rangle|^2$ of the actual output with respect to the squeezed cat exceeds 99% for $m \geq 2$. It is plotted in Fig. 5.2b. The squeezing in the final state is $\sim 3\,\mathrm{dB}$, which is accessible experimentally, and hence the state can in principle be unsqueezed if desired [40, 87, 128]. We note that since a weakly squeezed single photon $\hat{S}(s)|1\rangle$ is similar to a small cat state [82], if the unsqueezing operation is applied to the input single photons in our scheme, the protocol corresponds to conditional

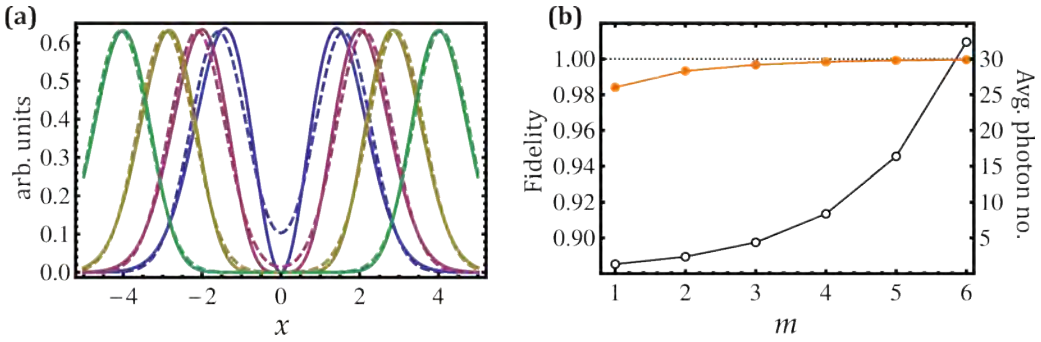

Figure 5.2: **(a)** Wavefunctions of the states produced by our protocol (solid) and of the corresponding squeezed cat states (dashed) for $m = 1, 2, 3, 4$. **(b)** Fidelity (dots) of the generated states with respect to squeezed cat states, and the average photon number (circles) in the unsqueezed cat states.

amplification of small cats with homodyne detection, reminiscent of the schemes in Refs. [82, 129].

The single-mode scheme can be generalised to an arbitrary number of modes by taking the single-photon source mode to be a superposition of some other set of modes. For example (5.3) represents a single excitation shared coherently between two spatially separated modes. More generally, the new mode variables form a vector $\mathbf{x}$, and the source mode variable is given by $\mathbf{u}^\dagger\mathbf{x}$ where $\mathbf{u}$ is a unit vector. Equivalently the annihilation operator for the source mode is $\mathbf{u}^\dagger\hat{\mathbf{a}}$, where $\hat{\mathbf{a}}$ is a vector of mode operators. The single mode source state (5.4) is replaced by

$$\frac{\sqrt{2}}{\pi^{M/4}} e^{-\frac{1}{2}\mathbf{x}^\dagger\mathbf{x}} \mathbf{u}^\dagger\mathbf{x}, \tag{5.9}$$

where M is the number of modes. Starting from a pair of sources, the single-mode protocol is applied to every corresponding pair of modes x_i, y_i and the single-mode condition $y \leq \Delta$ is replaced by $|\mathbf{u}^\dagger\mathbf{y}| \leq \Delta$, where $\mathbf{y}$ is the vector of measurement outcomes. Iterating this procedure, the final output state in the limit $\Delta \to 0$ can be written in terms of the single-mode output state as

$$|\psi_m\rangle_{\mathbf{u}} |vac\rangle_{\perp\mathbf{u}}, \tag{5.10}$$

where we have separated out the mode determined by $\mathbf{u}$ and $|vac\rangle_{\perp\mathbf{u}}$ is the vacuum state of the remaining modes. A coherent state $|\alpha\rangle$ in mode $\mathbf{u}$ is equivalent to a product state of the modes $1, \ldots, M$ of the form

$$|\alpha\rangle_{\mathbf{u}} |vac\rangle_{\perp\mathbf{u}} = |u_1\alpha\rangle_1 \cdots |u_M\alpha\rangle_M, \tag{5.11}$$

as one can check from the definition (2.17) of the displacement operator. Since $|\psi_m\rangle_{\mathbf{u}}$ is well approximated by $\hat{S}_{\mathbf{u}}|\xi(\mu_m)\rangle_{\mathbf{u}}$, the output state is therefore nearly given by

$$\hat{S}_{\mathbf{u}}(2)|\xi(\mu_m)\rangle_{\mathbf{u}} |vac\rangle_{\perp\mathbf{u}} = \hat{S}_{\mathbf{u}}(2)\left(|u_1\mu_m, \ldots, u_M\mu_m\rangle + |-u_1\mu_m, \ldots, -u_M\mu_m\rangle\right). \tag{5.12}$$

[3] It is not strictly necessary for the beam splitters to be balanced. In fact, any non-diagonal unitary will do.

This is a squeezed multi-mode cat state. The fidelity of the actual output state with respect to (5.12) is the same as in the single-mode case. It is plotted in Fig. 5.2b.

In the case of two modes, relevant to the repeater protocol below, the source states are given by (5.3) which corresponds to $\mathbf{u} = \frac{1}{\sqrt{2}}(1,1)$. The output state is

$$\hat{S}_+(2)|\gamma(\mu_m/\sqrt{2},0)\rangle_{ab}, \tag{5.13}$$

where 'a' and 'b' refer to two spatially separated modes and $\hat{S}_+(2)$ denotes squeezing by a factor of two in the variance of the symmetric quadrature $\hat{X}_+ = (\hat{X}_a + \hat{X}_b)/\sqrt{2}$. We note at this point that the squeezing in the state (5.13) is not local and cannot be locally undone. However, as we shall see below, after a few levels of entanglement swapping, the squeezing does actually become local.

5.1.2 Rate

Naturally, to get a non-zero probability for successful generation one needs to take a non-zero value of Δ. Non-zero measurement outcomes then degrade the generated states, and there will be a trade-off between the rate of generation and the output state fidelity. To get an idea about this trade-off and to see the effect of double excitations in the input states (c.f. (5.3)), we perform a numerical simulation of single-mode-cat generation. The generation scheme – for a single or multiple modes – may be implemented entirely on travelling light beams as depicted in Fig. 5.1. In that case, simultaneous success for all measurements is required to reach the output state. The rate can, however, be significantly increased if the states generated at each level of the protocol are stored in quantum memories, since in this case there is no requirement for simultaneity. The necessary homodyne measurements can be performed after retrieving the stored states onto light fields or potentially via quantum non-demolition measurements directly on the memories [1]. In our simulation we assume that memories are employed. We measure the fidelity of the generated states with respect to the squeezed cat $\hat{S}(2)|\xi(\mu_m)\rangle$, and we measure the rate in units of the source repetition rate, i.e. the rate at which singe photons can be produced. The result is shown in Fig. 5.3. With a double excitation contribution of 1%, we find that states with a fidelity of 90% with respect to $\hat{S}|\xi(\mu_3)\rangle$, corresponding to an unsqueezed cat amplitude $\alpha = 2.9$, can be generated at a rate of ~ 0.08.

Although the simulation in Fig. 5.3 was performed for a single mode, it gives a good indication of the trade-off for multiple modes as well due to the equivalence of the single- and multi-mode schemes explained above. For perfect input states with no multi-excitation component, the equivalence is exact. However, the error behaviour with multiple modes is more complex than for a single mode and hence the two cases differ when additional excitations are introduced.

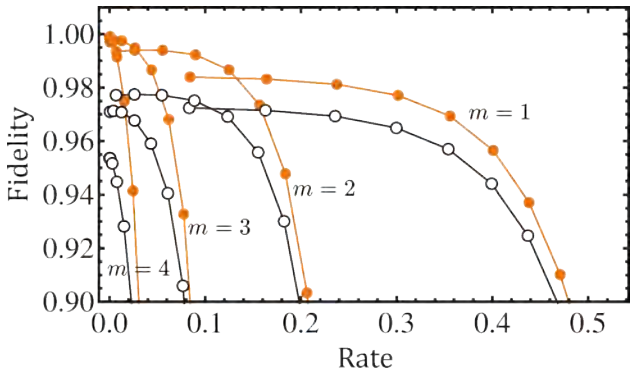

Figure 5.3: Probabilistic generation of single-mode cat states. The fidelity-rate trade-off is plotted for perfect input states (dots) and input states with a 1% two-photon contribution (circles). The rate is measured in units of the source repetition rate.

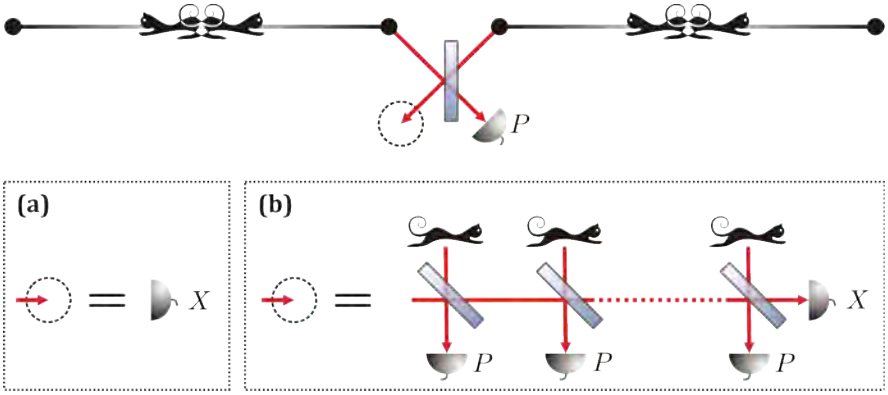

Figure 5.4: **(a)** Simple entanglement swapping. Two two-mode cat states are joined on a balanced beam splitter and the outputs are homodyned. Success is conditioned on an $\hat{X}$-outcome close to zero. **(b)** Improved entanglement swapping using k auxiliary single-mode cat states of size (left to right) $2^{1/2}\alpha$, 2α,...,$2^{k/2}\alpha$.

5.2 Entanglement swapping with ideal cats

In this section we show how entanglement swapping can be realised with ideal two-mode cat states, linear optics and homodyne measurements. We also demonstrate that the success probability for swapping can be increased when an additional local resource of single-mode cat states is allowed for. We treat the simple case without resource states first.

5.2.1 Simple probabilistic swapping

The setup is shown in Fig. 5.4a. The two connecting modes of a pair of consecutive entangled segments are mixed on a balanced beam splitter. At one output port, the $\hat{X}$-quadrature is measured via homodyne detection while at the other port the $\hat{P}$-quadrature is measured. The idea of the swapping procedure is that there are several terms in the input state leading to the same measurement outcome. Conditioning on this outcome therefore projects the output modes into

a superposition state, which is entangled. We consider entanglement swapping starting from two segments initially in the state $|\gamma(0,\alpha)\rangle$. For an arbitrary coherent state input $|\alpha_1\rangle|\alpha_2\rangle$, the balanced beam splitter outputs a product of coherent states with amplitudes $(\alpha_1 \pm \alpha_2)/\sqrt{2}$. In our case, each input mode is in one of the states $|\pm\alpha\rangle$, and thus the possible outputs are $|\pm\sqrt{2}\alpha\rangle$ and $|0\rangle$. There are two ways to obtain the latter, and hence measuring $\hat{X}$ and conditioning on an outcome close to zero results in an entangled output state. More formally, the unnormalised state prior to swapping is

$$|\gamma'(0,\alpha)\rangle|\gamma'(0,\alpha)\rangle = (|\alpha,\alpha\rangle + |-\alpha,-\alpha\rangle)\,(|\alpha,\alpha\rangle + |-\alpha,-\alpha\rangle]), \tag{5.14}$$

which is transformed by the beam splitter into

$$\begin{aligned}\Big[|\alpha,\alpha\rangle|\sqrt{2}\alpha\rangle_p + |-\alpha,-\alpha\rangle|-\sqrt{2}\alpha\rangle_p\Big]\,|0\rangle_x + |\alpha,-\alpha\rangle|0\rangle_p|\sqrt{2}\alpha\rangle_x \\ + |-\alpha,\alpha\rangle|0\rangle_p|-\sqrt{2}\alpha\rangle_x,\end{aligned} \tag{5.15}$$

where we have denoted the modes to be measured by x and p according to the relevant quadratures. For an arbitrary coherent state $|\beta\rangle$, the $\hat{P}$-space wavefunction is given by the Fourier transform of (2.28)

$$\langle p|\beta\rangle = \frac{1}{\pi^{1/4}} e^{-\frac{1}{2}p^2 - i\sqrt{2}\beta p + i\beta\,\mathrm{Im}(\beta)}. \tag{5.16}$$

It follows that after a $\hat{P}$-measurement with outcome p_0, the state of the remaining modes can be written (recall that α is real)

$$|\gamma'(\theta_0,\alpha)\rangle|0\rangle_x + |\alpha,-\alpha\rangle|\sqrt{2}\alpha\rangle_x + |-\alpha,\alpha\rangle|-\sqrt{2}\alpha\rangle_x, \tag{5.17}$$

where $\theta_0 = -2\alpha p_0$. If α is large enough for $|0\rangle$ and $|\pm\sqrt{2}\alpha\rangle$ to be nearly orthogonal, we see from this expression that an $\hat{X}$-measurement with an outcome close to zero will project the remaining modes to a perfect two-mode cat state. Since the last two terms of (5.17) each have norm 1 and $\langle\gamma'(\theta_0,\alpha)|\gamma'(\theta_0,\alpha)\rangle \approx 2$, the probability for this successful outcome is roughly $1/2$. If an outcome close to $\pm 2\alpha$ is obtained, the output state is separable and the swapping attempt has failed.

We note at this point that while the discussion so far neatly illustrates the idea of the swapping procedure and shows that the maximal success probability is $1/2$, it does not capture the effect of finite α. The requirement for the $\hat{X}$-outcome to be 'close to zero' is quantified by picking an acceptance interval $[-\delta,\delta]$. The bound δ must be chosen to ensure that the output state maintains good fidelity. If α is not very large such that there is a non-negligible overlap between $|0\rangle$ and $|\pm\sqrt{2}\alpha\rangle$, it may become necessary to restrict the acceptance interval so much that a non-negligible part of the $|0\rangle$-state distribution lies outside the bounds. In this case, the success probability is reduced from $1/2$. There is thus a trade-off between the rate and fidelity of swapping. We account for this trade-off numerically in our simulation below.

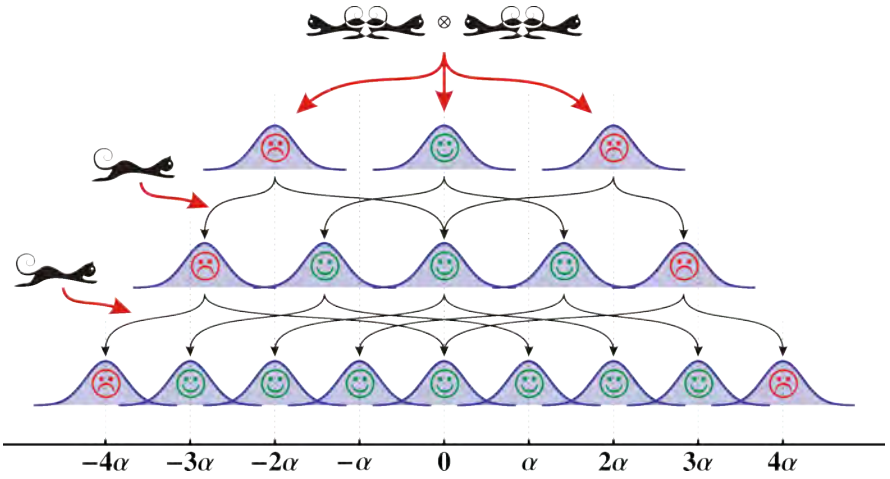

FIGURE 5.5: The effect of mixing with auxiliary states on the distribution of $\hat{X}$-measurement outcomes. Initially, the distribution has three contributions. When auxiliary single-mode cat states are mixed in, each peak separates into two with both extremal peaks contributing to a new peak at $X = 0$. All but the two extremal outcomes lead to successful entanglement swapping. However, as the number of outcomes increases so does the overlap between neighbouring peaks and the fidelity degrades.

5.2.2 Near-deterministic swapping

We have seen that probabilistic entanglement swapping of two-mode cat states is simple to implement. As we now demonstrate, the swapping can be made nearly deterministic using auxiliary single-mode cat states as a resource. The setup is shown in Fig. 5.4b. Additional beam splitters are inserted between the first beam splitter output and the $\hat{X}$-measurement of the simple setup for probabilistic swapping. At the j'th beam splitter an auxiliary single-mode cat state $|\xi(2^{j/2}\alpha)\rangle$ is injected, and a $\hat{P}$-measurement with outcome p_j is performed in one output port.

To understand how the scheme works, we can start by considering just one auxiliary state. By mixing the output from the first beam splitter with a single-mode cat of amplitude $\sqrt{2}\alpha$ we arrange that each of the 'failure' terms $|\pm\sqrt{2}\alpha\rangle_x$ of (5.17) above can combine with one term of the auxiliary state to yield $|0\rangle_x$. An $\hat{X}$-outcome of zero then again projects the output to an entangled state. At the same time, the 'success' term $|0\rangle_x$ above splits into $|\pm\alpha\rangle_x$, leading to two possible $\hat{X}$-outcomes each of which still produces the entangled state $|\gamma'(\theta_0,\alpha)\rangle$. We have thus increased the number of measurement outcomes which lead to successful swapping, provided that α is sufficiently large for $|0\rangle$ and $|\alpha\rangle$ to be nearly orthogonal. For each additional auxiliary state, this picture is repeated. The first couple of steps are illustrated in Fig. 5.5. Formally, mixing in the first auxiliary cat changes the state (5.17) to

$$|\gamma'(\theta_0,\alpha)\rangle(|\alpha\rangle_p|\alpha\rangle_x + |-\alpha\rangle_p|-\alpha\rangle_x) + |\alpha,-\alpha\rangle(|2\alpha\rangle_p|0\rangle_x + |0\rangle_p|2\alpha\rangle_x) \\ + |-\alpha,\alpha\rangle(|0\rangle_p|-\sqrt{2}\alpha\rangle_x + |-2\alpha\rangle_p|0\rangle_x), \tag{5.18}$$

and after two $\hat{P}$-measurements the (unnormalised) state is then

$$|\tilde{\gamma}'(\theta_1,\alpha)\rangle|0\rangle_x + |\gamma'(\theta_0,\alpha)\rangle(e^{i\nu}|\alpha\rangle_x + e^{-i\nu}|-\alpha\rangle_x) + |\alpha,-\alpha\rangle|2\alpha\rangle_x \\ + |-\alpha,\alpha\rangle|-2\alpha\rangle_x, \tag{5.19}$$

where $\theta_1 = -2^{3/2}\alpha p_1$, and $|\tilde{\gamma}'(\theta_1,\alpha)\rangle = e^{i\theta_1}|\alpha,-\alpha\rangle + e^{-i\theta_1}|-\alpha,\alpha\rangle$ is equal to $|\gamma'(\theta_1,\alpha)\rangle$ up to a local phase shift. The phase $\nu = \sqrt{2}\alpha p_1$ is unimportant since it results only in an overall front factor on the final state. Assuming that $|0\rangle$ and $|\alpha\rangle$ are nearly orthogonal, $\hat{X}$-outcomes originating in the $|0\rangle_x$ or $|\pm\alpha\rangle_x$ terms of (5.19) all project the output to a two-mode cat state. Only the extremal outcomes lead to failed swapping. Counting terms, the success probability is seen to be $3/4$.

Generalising to k auxiliary states, we find that the success probability scales as

$$1 - 2^{-k-1} \tag{5.20}$$

given that all terms remain distinguishable. The overlap between two neighbouring terms at level k is

$$\langle 0|2^{-\frac{k-1}{2}}\alpha\rangle = e^{-2^{-k}\alpha^2}, \tag{5.21}$$

where (2.13) was used. Thus to keep the output state fidelity above some given threshold, α must scale with k as $\alpha \sim 2^{k/2}$. Equivalently, the failure probability for entanglement swapping scales inversely with the mean photon number in the largest available two-mode cat state and with the square root of the mean photon number in the largest available single-mode cat. This result demonstrates that given sufficiently large cat-state resources, entanglement swapping using only linear optics and homodyne measurements can be performed with success probability arbitrarily close to one, i.e. near-deterministically.

Teleportation

It is interesting to note, that the same idea can be used for near-deterministic teleportation. Coherent state quantum computing is based on qubits encoded in non-orthogonal coherent states $|\pm\alpha\rangle$ [83, 107]. Such a qubit can be teleported across an entangled segment by a setup analogous to the one in Fig. 5.4b. If one of the two entangled segments in the figure is replaced by $|\phi\rangle = a|\alpha\rangle + b|-\alpha\rangle$ then the state after the first $\hat{P}$-measurement becomes

$$\left[ae^{i\theta_0}|\alpha\rangle + be^{-i\theta_0}|-\alpha\rangle\right]|0\rangle_x + a|-\alpha\rangle|\sqrt{2}\alpha\rangle_x + b|\alpha\rangle|-\sqrt{2}\alpha\rangle_x, \tag{5.22}$$

where we have again denoted the mode measured in $\hat{X}$ by x and $\theta_0 = -2\alpha p_0$ as before. After the second $\hat{P}$-measurement we have

$$\left[ae^{i\theta_1}|-\alpha\rangle + be^{-i\theta_1}|\alpha\rangle\right]|0\rangle_x + \left[ae^{i\theta_0}|\alpha\rangle + be^{-i\theta_0}|\alpha\rangle\right]\left(e^{i\nu}|\alpha\rangle_x + e^{-i\nu}|-\alpha\rangle_x\right) \\ + a|-\alpha\rangle|\sqrt{2}\alpha\rangle_x + b|\alpha\rangle|-\sqrt{2}\alpha\rangle_x, \tag{5.23}$$

with $\theta_1 = -2^{3/2}\alpha p_1$. Continuing along the same lines we see that by conditioning on an $\hat{X}$-measurement outcome close to zero, just as for entanglement swapping above the state $|\phi\rangle$ can be teleported up to a known phase change of a and b (and a possible bit flip $|\alpha\rangle \to |-\alpha\rangle$ which is trivial to undo) with success probability arbitrarily close to one for sufficiently large α.

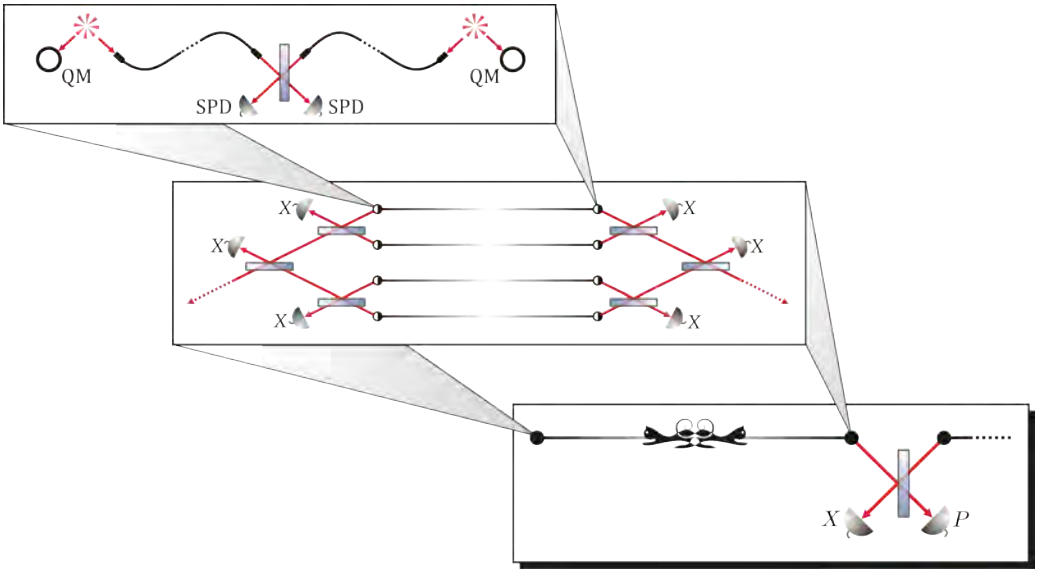

FIGURE 5.6: Nested steps of the hybrid repeater protocol. First, single-excitation entanglement is generated by mixing light form two-mode squeezing sources on a balanced beam splitter and detecting a single photon. The entangled modes are stored in quantum memories (QM). Second, two-mode cat states are grown from the single excitations by means of beam splitters and homodyne measurements. Third, entanglement is swapped to longer distances via homodyning.

5.3 A cat-state repeater

We now turn to the assembly of the steps outlined above – creation of single-photon entangled states, generation of two-mode cat states from the single-photons states, and entanglement swapping – into a fully fledged quantum repeater protocol. The repeater consists in a channel of length L divided into 2^n segments of a shorter length L_0. Two-mode cat states are generated across each segment separately, and the segments are then connected by entanglement swapping. For simplicity, we will consider only simple swapping (Fig. 5.4a) without any auxiliary states. The nested structure of the protocol is illustrated in Fig. 5.6.

5.3.1 Target

The benchmark for the performance of the repeater is the rate at which final, entangled states can be generated with a fixed fidelity with respect to some useful, ideal target state. As a target state for the present protocol we identify a locally squeezed two-mode cat state. Such a state is approached for small widths of the acceptance intervals in cat-state generation and entanglement swapping and vanishing pair production probability during initial entanglement generation, i.e. for $\Delta, \delta, p \to 0$. In this limit the entangled states before swapping are given by (5.13). Conditioning on zero in all $\hat{X}$-measurements, we find that for sufficiently large m the wavefunction after n levels of entanglement swapping can be

expressed as (see App. C.2)

$$\psi_{mn}(x_a, x_b) = e^{-i(\phi_{a,n}x_a+\phi_{b,n}x_b)}e^{-\frac{k_n}{8}(x_a-x_b)^2}\times \left[e^{-\frac{1}{k_n}(x_a+x_b-\mu_m)^2-i\varphi_n} + e^{-\frac{1}{k_n}(x_a+x_b+\mu_m)^2+i\varphi_n}\right], \tag{5.24}$$

where we have denoted the modes of the two entangled nodes by 'a' and 'b'. The parameter k_n is given by $k_n = 2\sqrt{2}\coth(2^n \operatorname{arccoth}(\frac{1}{\sqrt{2}}))$ while $\phi_{a,n}$, $\phi_{b,n}$ and φ_n are determined recursively and depend on the $\hat{P}$-measurement outcomes at all previous levels of entanglement swapping. The recursion relations are given in App. C.2. The parameters $\phi_{a,n}$ and $\phi_{b,n}$ are displacements in phase-space along the quadratures $\hat{P}_a$ and $\hat{P}_b$. Such displacements can be trivially cancelled by local operations, and we can therefore drop the first term of (5.24). The state can then be written as

$$\hat{S}_+(\frac{4}{k_n})\hat{S}_-(\frac{k_n}{2})|\xi(\varphi_n, \frac{\mu_m}{\sqrt{k_n}})\rangle_+|vac\rangle_-, \tag{5.25}$$

where '$+$' and '$-$' refer to the symmetric and anti-symmetric combinations of the spatial modes a and b respectively. This is a product of a squeezed cat state in the symmetric mode and a squeezed vacuum state in the anti-symmetric mode. A single-mode cat state in the symmetric mode is equivalent to a two-mode cat state in the spatial modes a and b since according to (5.11)

$$|\alpha\rangle_+|vac\rangle_- = |\frac{\alpha}{\sqrt{2}}\rangle_a|\frac{\alpha}{\sqrt{2}}\rangle_b. \tag{5.26}$$

Still, (5.25) is not quite a locally squeezed cat state because the symmetric and anti-symmetric modes are not squeezed by the same amount. However, k_n converges fast toward $2\sqrt{2}$ and in this limit

$$\hat{S}_+(\frac{4}{k_n})\hat{S}_-(\frac{k_n}{2}) = \hat{S}_+(\sqrt{2})\hat{S}_-(\sqrt{2}) = \hat{S}_a(\sqrt{2})\hat{S}_b(\sqrt{2}), \tag{5.27}$$

as one can check from (2.18) using the mode operators $\hat{a}_\pm = (\hat{a}_a \pm \hat{a}_b)/\sqrt{2}$. Hence after a few levels of entanglement swapping, our state becomes

$$|\psi_{id}\rangle_{ab} = \hat{S}_a(\sqrt{2})\hat{S}_b(\sqrt{2})|\gamma(\varphi_n, 2^{-5/4}\mu_m)\rangle_{ab}. \tag{5.28}$$

This is a two-mode cat state in the spatial modes a and b with local squeezing of the $\hat{X}_a$ and $\hat{X}_b$ quadratures by a factor of $\sqrt{2}$ or 1.5 dB. We take it to be our target state.

It is interesting to note that although the state (5.13) exhibited a non-local squeezing, after a few levels of swapping the squeezing has become local and can be undone by local operations. The required amount of 1.5 dB is easily accessible in current experiments [40, 87, 128]. The target state can thus in principle be converted to a two-mode cat state with no squeezing, although this may not be necessary for all applications since in an experiment where all modes are squeezed equally and measured by homodyne detection, the squeezing just amounts to a rescaling of the measurement results. We have seen above that, in combination with auxiliary single-mode cats, two-mode cat states can be used to realise

near-deterministic teleportation with only linear optics and homodyne measurements. Also, as previously mentioned, two-mode cat states are useful resources with applications e.g. in existing proposals for fault-tolerant linear optical quantum computing with coherent states and teleportation of gates or states based on single-photon detection [83, 103, 134]. There is thus good reason to create non-local two-mode cats. At the same time, it is apparent from the numerical simulations below that our hybrid repeater protocol can indeed produce states which are very close to (5.28). Hence (5.28) is a sensible target state.

5.3.2 Performance

With (5.28) as our target, we perform a numerical simulation of the full repeater protocol, maximising the rate at each distance L for a fixed final state fidelity threshold

$$F = {}_{ab}\langle\psi_{id}|\hat{\rho}_{out}|\psi_{id}\rangle_{ab}|^2 \geq 0.9. \tag{5.29}$$

When performing the optimisation, there are five parameters to consider, namely p, n, m, Δ and δ. The pair production probability p determines the average number of trials needed to generate single-photon entanglement as well as the admixture of double excitation terms into the generated states. The number of swapping levels n determines the basic segment length L_0 and hence the classical communication time L_0/c between nodes, where c is the speed of light. The number of generation levels m and the acceptance Δ controls the time necessary to grow an approximate two-mode cat and the fidelity of the generation process, and δ controls the entanglement swapping success probability and fidelity.

We carry out the optimisation for a given distance in several steps. We start by computing the average fidelity F_1 and the entanglement generation and connection success probabilities on a grid of values of n, m, Δ, and δ assuming perfect initial single-photon entanglement, i.e. for $p = 0$. Next, we compute the fidelity F_2 on the same grid, replacing one of the single-photon input states by a pure two-photon component. In the third step we take all grid points for which F_1 exceeds the bound (5.29) and determine the largest possible value of p for which the bound is still satisfied by

$$F(p, n, m, \Delta, \delta) = (1 - 3p)F_1(n, m, \Delta, \delta) + 3pF_2(n, m, \Delta, \delta). \tag{5.30}$$

The factor of 3 comes from the number of ways to distribute 2 excitations across one segment (two on the left, two on the right or one on each side). In the fourth step we compute the rate for all grid points at the given distance and determine the maximum.

Our approach effectively amounts to a perturbative treatment in p. In addition to this approximation we make a couple of other assumptions. In our calculation of the two-photon component, we make a worst-case assumption for the transmission during entanglement generation, $e^{-L_0/2L_{att}} \ll 1$, where L_{att} is the attenuation length. The probability for two photons to make it to the detectors simultaneously is then negligible and to first order in p the input states are given by (2.61)

$$(1 - 3p)|\Psi^+\rangle\langle\Psi^+| + 3p\,\rho_2, \tag{5.31}$$

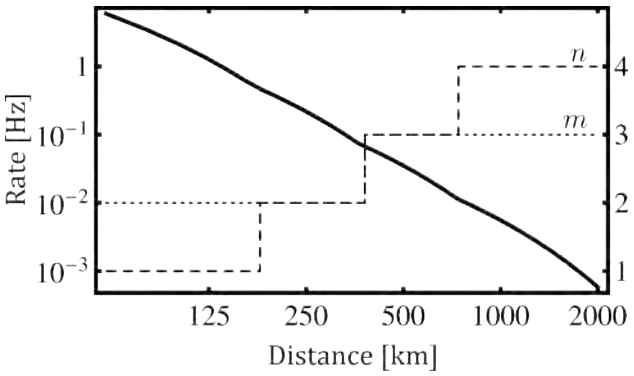

FIGURE 5.7: Simulation of the full repeater protocol including both generation and connection of entangled states. We plot the rate (solid line) assuming a final fidelity of 90%, a fibre attenuation length of 20 km and a single-photon detection efficiency of 50%. The rhs axis shows the optimal values of n and m.

with the two-photon component ρ_2 given by (2.62). The assumption also implies that it does not matter whether the single-photon detectors are number resolving or not. In the superposition basis, the two-photon component is a simple mixture

$$\rho_2 = \frac{1}{3}|11\rangle_{+-}\langle 11| + \frac{2}{3}|20\rangle_{+-}\langle 20|. \tag{5.32}$$

Since our cat generation scheme is naturally described in this basis (the symmetric and antisymmetric modes effectively decouple according to (5.10)) this means that the $|11\rangle$ and $|20\rangle$ type errors can be treated separately which provides a technical simplification in the calculation of $F_2 = \frac{1}{3}F_{11} + \frac{2}{3}F_{20}$. When computing the rate, we assume that local operations are much faster than L_0/c, such that the repetition rate for generation of single-photon entanglement is c/L_0 (the 'source repetition rate' for generating (5.3)). As mentioned in previous chapters, this is a common assumption in the quantum repeater litterature [72, 111, 112, 119, 135, 145]. From the simulation we find typical segment lengths on the order of 100 km, corresponding to about 0.5 ms. Recent experiments have demonstrated storage, retrieval, and entanglement generation on timescales of $< 1\,\mu$s. The assumption is thus consistent. We take a fibre attenuation length of 20 km and a 50% detection efficiency for the single-photon detectors. For runtime reasons we have restricted the number of generation steps to $m \leq 3$.

The result of the simulation is shown in Fig. 5.7. At 1000km our protocol reaches a rate of 0.3 pairs/minute. The best reported numbers for atomic-ensemble-based repeaters in the discrete variable regime are comparable to this [13, 111, 114]. E.g. of the six schemes compared in Ref. [114], five achieve rates of this order of magnitude or lower and one is about one order of magnitude faster. However, these numbers assume high-efficiency single-photon detectors ($\gtrsim 90\%$) which, unlike the efficient homodyne detectors employed in the present scheme, are not readily available in the lab as discussed in Sec. 2.3. The schemes are very sensitive to detection efficiency [111]. The scheme of Chap. 4 is less sensitive to SPD efficiency, but this comes at the expense of more complicated entanglement generation and swapping procedures. Temporal or spatial multiplexing, which offer potential speed-ups for the discrete variable protocols might

also be applicable to the present scheme, in particular for improving the initial generation of single-photon entanglement. The hybrid repeater thus seems to present a promising alternative route on the quest for higher entanglement distribution rates. We should also note that for existing repeaters in the discrete variable regime, the success probability for entanglement swapping can never exceed $1/2$ even when all operations are perfect. This is because a Bell measurement implemented only with linear optics and SPD without (non-vacuum) auxiliary states can never succeed with probability better than $1/2$, as proven by Calsamiglia and Lütkenhaus [23]. There is no obvious way of beating this limit for the discrete schemes (although one could perhaps consider adaptations of the near-deterministic linear optics gates proposed by Knill, Laflamme and Milburn [75]). On the other hand, for the protocol presented in this chapter, we have demonstrated that near-deterministic swapping is possible when the swapping procedure of Fig. 5.4a is replaced by that of Fig. 5.4b.

5.4 Conclusion

In this chapter we have presented a hybrid quantum repeater protocol combining entanglement generation in the discrete variable regime with growth of entangled states and entanglement swapping in the continuous variable regime. We have shown how quadrature squeezed Schrödinger cat states can be grown from single-photon states using only linear optics and homodyne detection both in local variants and in non-local variants shared between multiple modes, and we have demonstrated that entanglement in the form of two-mode cat states can be distributed to long distances also by means of homodyne detection. The basic entanglement swapping procedure succeeds with probability $1/2$. We have shown that by taking advantage of local auxiliary single-mode cats, this probability can be increased and scales inversely with the mean photon number in the largest available two-mode cat state and with the square root of the mean photon number in the largest available single-mode cat. For sufficiently large cat state amplitudes near-deterministic operation is achieved. This also implies that near-deterministic teleportation with linear optics and homodyning is possible.

The use of homodyne rather than single-photon detectors is advantageous for the entanglement distribution rate because homodyne detectors can have very high efficiencies, whereas high-efficiency single-photon detectors are not as readily available currently. By numerical simulation of a protocol with the basic entanglement swapping setup, we found that the hybrid quantum repeater achieves a rate comparable to the rates of the best proposed ensemble-based repeaters in the discrete regime, when high-efficiency single-photon detection is assumed for those schemes. In combination with the potential for near-deterministic entanglement swapping, this leads us to conclude that the hybrid approach represents a promising avenue for reaching higher rates.

Since our protocol uses only linear optics, light storage and retrieval, and single-photon and homodyne detectors, the means for a first experimental implementation are in principle available in today's laboratories. However in any experiment there are bound to be losses, and in particular the quantum memories cannot be

expected to have high efficiencies. In the treatment presented above we have provided no analysis of the effect of imperfections in the cat state generation or swapping processes. Cat state entanglement is known to be sensitive to loss [134] and a more careful analysis taking memory and detector inefficiencies into account is needed to fully judge the viability of our scheme.

Our treatment has also been slightly limited on a couple of other accounts. The number of steps in the cat state generation was restricted to $m \leq 3$. It is desirable to simulate the protocol also for higher m, since one can easily imagine applications where cats of a certain size are desired. For $m = 3$, the coherent states in the two-mode cat produced by our protocol have an amplitude (without squeezing) of $\alpha = 2^{-5/4}\sqrt{8+1/2} \approx 1.23$ which gives an overlap of $\langle\alpha|-\alpha\rangle \sim 5\%$ for two states of opposite phase. We have also worked with a fixed acceptance interval Δ for the conditional measurements at all levels of cat state generation. In principle there might be some advantage to adapting this interval at each level. Since the cats are growing for every iteration, the separation of peaks in the distribution of $\hat{X}$-measurement outcomes is also increasing and hence larger Δ can be applied at higher levels without degrading the fidelity. This may allow a gain in the rate of generation.

An intriguing perspective on the work in this chapter would be to investigate whether cat state generation can be performed entirely in an atomic ensemble memory without any need for retrieval by implementing the homodyne measurements via quantum non-demolition probing directly on the atoms [1]. Also, recently a method was demonstrated by Ourjoumtsev *et al.* for generating a nonlocal two-mode cat state from two separated single-mode cats by nonlocal subtraction of a single photon in a setup similar to that of Fig. 2.8 [100]. A repeater based on this method, cat states, and single-photon detection has been proposed by Sangouard *et al.* [112]. An interesting variant of our scheme might be obtained by generating single-mode cats locally and incorporating the method of Ref. [100] to entangle nodes.

Chapter 6

Summary and outlook

6.1 Summary

In this thesis we have been concerned with the distribution of entangled states over distances much longer than typical attenuation lengths associated with transmission of light. Light is an ideal carrier of quantum states because it couples only weakly to its environment. Nevertheless, for direct transmission e.g. through optical fibre, loss and decoherence probabilities grow exponentially with distance leading to an exponential decrease in distribution rate. Classical amplification schemes fail to resolve this problem due to the no-cloning principle for quantum states, but polynomial scaling of the rate is made possible by quantum repeater protocols which first establish entanglement between a string of nodes separated by shorter distances and then join entangled segments to form longer links by quantum teleportation. The entanglement is generated in a probabilistic fashion and the approach therefore relies on quantum memories in which the generated entangled states can be stored allowing different segments to succeed at different times. In the thesis we have studied three different proposals for repeaters. In the first two, atomic ensembles play the role of quantum memories with the entangled states encoded in collective spin-wave excitations. The last protocol was developed without reference to any particular memory, but relies on the same method for entanglement generation as the first two, which may be implemented using atomic ensembles.

In Chap. 3 we studied a repeater protocol which can be seen as a generalised version of the seminal proposal by Duan, Lukin, Cirac and Zoller [41]. We paid particular attention to the quantum memories and the impact of memory imperfections on the fidelity of the output states, and we developed a formalism in which the memories are described as Bogoliubov transformations on a set of harmonic oscillator modes. This formalism encompasses any memory with an interaction Hamiltonian of at most quadratic order in the mode operators. In particular, atomic-ensemble-based memories typically admit such a description. Taking the most general Bogoliubov transformation and treating imperfections in first-order perturbation theory, we obtained the scaling of memory induced

errors as well as the scaling of errors coming from dark counts and from multiple excitations introduced during entanglement generation. All these errors were found to scale quadratically with the number of repeater segments and we found that memory errors can generally be described as either single-mode squeezing of the stored mode or two-mode squeezing of this mode and an auxiliary noise mode, which is related to the fact that any quadratic Hamiltonian can be constructed from squeezers, phase shifts and displacements [18]. To corroborate our perturbative results we compared them to numerical simulations, picking two particular atomic-ensemble based quantum memory protocols. We found good agreement between simulation and analytics within the validity range of the perturbation. Finally, we derived an expression for the rate in the single-rail repeater architecture applicable when multiexcitation events are the dominant error source. This expression proved useful in the subsequent chapter.

The scaling of the rate in single-rail repeaters, although sub-exponential, is poor due to a rapid growth of the vacuum component of the generated states. This can be overcome by basing protocols on dual-rail entanglement and entanglement swapping on two-photon detection, in which case the vacuum component can be made constant and multiexcitation errors scale linearly rather than quadratically. However low efficiencies of retrieval and single-photon detection significantly limit the rates in ensemble-based repeaters even with dual-rail entanglement. In Chap. 4 we proposed a new type of atomic-ensemble-based repeater protocol inspired by ideas for quantum computing with collective atomic excitations and for efficient detection of single photons absorbed in atomic ensembles via fluorescence measurements. By storing multiple spin-waves within the same atomic ensemble, the need for retrieval is eliminated and single-photon detection can be replaced by efficient fluorescence measurements. We showed that using these ideas, the single-rail DLCZ scheme and the dual-rail scheme of Jiang *et al.* can be mapped onto protocols with only a single ensemble at each repeater node and, and for a single-photon detection efficiency of 40% and a fluorescence measurement efficiency of 95%, we saw improvements in rate of three to four orders of magnitude at 1000 km. We found that incoherent spin-wave excitations associated with transverse scattering during entanglement generation show up as dark counts in the fluorescence measurements, and we devised a method for suppressing these dark counts via 'purification by interrupted retrieval' which, however, requires the atoms to be confined in a photonic structure such as a hollow-core fibre or low-finesse cavity. We discussed implementation of our scheme in alkali and alkali-earth atoms, in particular ^{87}Rb and ^{87}Sr. For alkali the limit on the number of atoms imposed by off-resonant scattering is too low to be compatible with good optical depth for implementations with more than one level of swapping but alkali-earths appear to be promising candidates for implementations over distances of order 1000 km

In Chap. 5 we ventured into the realm of continuous variable quantum information – relatively unexplored terrain in the context of quantum repeaters. Our motivation was again to improve the efficiency of entanglement swapping, this time by replacing inefficient single-photon detection by highly efficient homodyne detection. To this end, we developed a probabilistic scheme for growing coherent state superpositions – Schrödinger cat states – from single-photon states

using only linear optics and homodyning, and we showed that probabilistic entanglement swapping with two-mode Schrödinger cat states can be implemented by the same means. Based on this, we presented a hybrid quantum repeater protocol combining discrete variable entanglement generation with continuous variable growth and swapping to distribute cat states over long distances. A numerical simulation of the protocol assuming ideal quantum memories and homodyne detectors showed that reasonably high rates for simple swapping can be obtained, on par with those found for ensemble-based repeaters in the discrete regime when high efficiency of single-photon detection is assumed. Furthermore we demonstrated that entanglement swapping can be made near-deterministic with the assistance of a local supply of single-mode cat states, which can in principle be produced using our growth scheme. The probability for swapping to fail decreases linearly with the mean photon number of the largest available two-mode cat and the square root of the mean photon number in the largest available single-mode cat.

6.2 Outlook

Our analyses of the new protocols presented in Chap. 4 and Chap. 5 are still wanting in certain respects.

For the fluorescence based protocol, a more detailed study of implementation of the dual-rail scheme in specific atomic species is definitely desirable. We have already identified alkali-earth atoms as promising candidates due to their long-lived excited states, but more work is required to identify which configuration is more convenient in terms of wavelengths, transitions strengths (which determine the time needed for fluorescence measurements), branching ratios, and controllability of the magnetic sublevel manifold. The possibility to alleviate the restrictive upper bounds on the atom number for alkali by state selective trapping also deserves careful consideration. If the bounds for alkali could be relaxed this would greatly enhance the experimental viability of of the protocol. A state selective trap might allow atoms in the storage states to be spatially separated from the reservoir atoms prior to fluorescence detection, reducing dark counts. Hence one should investigate whether state selective trapping can be made compatible with the other requirements of our scheme, in particular the need to enclose the atoms in a photonic structure. For example one could imagine state-dependent 1-d lattices along the axis of a hollow-core fibre [3, 79].

For the hybrid protocol based on entangled Schrödinger cat states, a study incorporating losses is needed. In our treatment so far we have included the finite efficiency of single-photon detection as well as errors introduced by double excitations during entanglement generation, but we have assumed unit efficiency for the quantum memories and homodyne measurements. This was fine in the context of investigating the inherent trade-offs in the protocol. However, while it is true that homodyning can be done very efficiently, the assumption is certainly unrealistic for the quantum memories and this should be taken into account. Both our schemes for growing cat states and for entanglement swapping rely on conditioning on $\hat{X} \sim 0$ in a quadrature measurement, which can be understood

as similar to conditioning on even photon-number parity since all odd Fock state wavefunctions vanish at the origin. Based on this one can expect a high sensitivity to loss, since the loss of a single photon changes the parity from even to odd. Other studies of teleportation and entanglement swapping with cat states and single-photon detection also indicate that this form of entanglement is fragile with respect to losses [112, 134].

In a broader perspective, despite the impressive experimental and theoretical progress since the field-opening DLCZ paper, the entanglement distribution rates predicted not only for the schemes presented in this thesis but for all atomic-ensemble-based protocols proposed so far are rather low, generally less than 0.1 pair/second for distances on the order of 1000 km [111]. This is insufficient for realistic implementation of communication schemes such as quantum key distribution. More importantly in the short term, it implies low data collection rates for experiments demonstrating the principles of quantum repeaters and furthermore is incompatible with current coherence times for most quantum memories. In implementations of probabilistic repeaters it is important for the memory coherence time to be long enough to store the entangled states until the final entanglement swapping or postselection attempt has been carried out. The storage time therefore must be at least of the same order as the inverse rate. The longest storage times demonstrated in cold atomic gasses are a few hundred ms, and less in hot gasses. For solid-state ensembles storage up to 1 s has been demonstrated, but with low (1%) efficiency [111]. It has been shown by Collins *et al.* [35] that the storage time requirements can be significantly relaxed by spatial multiplexing, which requires several parallel repeater architectures to be interwoven. This is a promising approach, but complicated to implement in practise.

One major stumbling stone for achieving higher rates is that the success probability of entanglement swapping in these schemes is limited to 1/2 even with perfect quantum memories and detectors. For schemes in the discrete regime using entanglement swapping based on linear optics and single-photon detection without auxiliary states, this is a fundamental limit [23]. There have been many proposals for implementing repeaters in alternative systems which in principle allow the implementation of deterministic Bell measurements. The most promising system currently is probably trapped ions, since techniques for quantum information processing with ions are generally very far advanced [9, 67, 90]. A scheme combining trapped ions with temporal multiplexing for an additional speed-up was recently put forward [110]. Other proposals include nitrogen-vacancy centres in diamond [28, 29], and quantum dots [120]. A more exhaustive list with references can be found in the review of ensemble-based repeater by Sangouard *et al.* [111]. For the two new schemes presented in this thesis, there is some potential for overcoming the 1/2-limit and approaching deterministic entanglement swapping. In the scheme of Chap. 4 where the same ensemble stores multiple spin-waves, one might hope to employ Rydberg blockade to implement a controlled-not operation [20]. Rydberg blockade is also applicable in principle to schemes with multiple ensembles provided they are close enough for the blockade to be effective, however in terms of distance it is clearly an advantage to work with only one ensemble per repeater node. In the hybrid scheme we have

seen that near-deterministic teleportation or swapping can be achieved with a local resource of auxiliary single-mode cat states, provided that cat states with sufficiently large amplitudes can be grown.

Looking further ahead, another issue will eventually affect achievable rates. To reach very long distances in the presence of realistic imperfections, all the repeater protocols we have discussed so far, even with deterministic entanglement swapping, are likely to require entanglement purification which relies on two-way classical communication. This means that the rates they can achieve are ultimately limited by the time required for light to travel from one end of the repeater to the other, and the communication distance is limited by the coherence time of the quantum memories. These limits can be beat by schemes which require only one-way classical communication, at the price of a polynomially increasing (with distance) number of qubits per node, based on quantum error correcting codes [64, 73].

Appendix A

Supplement to Chapter 3

A.1 Integral form of the vacuum projector

Here we prove the following

Lemma

$$|vac\rangle\langle vac| = \int \frac{dpdx}{2\pi} e^{-(x^2+p^2)/4} \hat{D}(\frac{x+ip}{\sqrt{2}}) \tag{A.1}$$

where $|vac\rangle$ is the vacuum state for the mode on which $\hat{D}(\cdot)$ acts.

Proof

The eigenstates of the quadrature $\hat{X}$ form a complete set and are denoted by $|x\rangle$, where $x \in \mathbb{R}$. Since the canonical commutator is $[\hat{X}, \hat{P}] = i$, the translation operator for the X-eigenstates is given by $e^{-i\hat{P}\Delta x}$ (see e.g. [109] p. 44ff). We may therefore write

$$|x\rangle\langle x'| = |x\rangle\langle x| e^{i\hat{P}(x'-x)} = |x\rangle\langle x| e^{-(\hat{a}^\dagger - \hat{a})\frac{x'-x}{\sqrt{2}}} = |x\rangle\langle x| \hat{D}(\frac{x-x'}{\sqrt{2}}) \tag{A.2}$$

Now for any $x' \in \mathbb{R}$ we have:

$$\begin{aligned} \int \frac{dp}{2\pi} e^{ip(\hat{X}-x)} |x'\rangle &= \int \frac{dp}{2\pi} e^{ip(x'-x)} |x'\rangle = \delta(x'-x)|x'\rangle \\ &= \delta(x'-x)|x\rangle = |x\rangle\langle x|x'\rangle \end{aligned} \tag{A.3}$$

and hence the operator $|x\rangle\langle x|$ equals the integral expression on the left. Inserting this into (A.2) we obtain

$$\begin{aligned} |x\rangle\langle x'| &= \int \frac{dp}{2\pi} e^{ip(\hat{X}-x)} \hat{D}(\frac{x-x'}{\sqrt{2}}) = \int \frac{dp}{2\pi} e^{ip(\frac{\hat{a}^\dagger + \hat{a}}{\sqrt{2}} - x)} e^{\hat{a}^\dagger \frac{x-x'}{\sqrt{2}} - \hat{a}\frac{x-x'}{\sqrt{2}}} \\ &= \int \frac{dp}{2\pi} e^{\hat{a}^\dagger \frac{x-x'+ip}{\sqrt{2}} - \hat{a}\frac{x-x'-ip}{\sqrt{2}}} e^{-ip(x+x')/2} \\ &= \int \frac{dp}{2\pi} \hat{D}(\frac{x-x'+ip}{\sqrt{2}}) e^{-ip(x+x')/2} \end{aligned} \tag{A.4}$$

where the disentangling theorem was used in the second line ([52] p. 49). With the help of (A.4) and (3.18) we can express the projection on the vacuum in the following manner (note that the vacuum state is not the same as $|x=0\rangle$)

$$\begin{aligned}
|vac\rangle\langle vac| &= \int dxdx' |x\rangle\langle x|vac\rangle\langle vac|x'\rangle\langle x'| \\
&= \int dxdx' |x\rangle\langle x'|\langle vac|x'\rangle\langle x|vac\rangle \\
&= \int \frac{dxdx'dpdp'}{(2\pi)^2} \hat{D}(\frac{x-x'+ip}{\sqrt{2}}) e^{-ip(x+x')/2} e^{-\frac{1}{2}\left|\frac{x'-x+ip'}{\sqrt{2}}\right|^2} e^{-ip'(x+x')/2} \\
&= \int \frac{dxdx'dpdp'}{(2\pi)^2} \hat{D}(\frac{x-x'+ip}{\sqrt{2}}) e^{-i(p+p')(x+x')/2} e^{-\frac{1}{4}\left[(x-x')^2+p'^2\right]} \\
&= \int \frac{dydy'dpdp'}{2(2\pi)^2} \hat{D}(\frac{y+ip}{\sqrt{2}}) e^{-i(p+p')y'/2} e^{-(y^2+p'^2)/4} \\
&= \int \frac{dydpdp'}{2(2\pi)} \hat{D}(\frac{y+ip}{\sqrt{2}}) \delta(\frac{-p-p'}{2}) e^{-(y^2+p'^2)/4} \\
&= \int \frac{dydp}{2\pi} e^{-(y^2+p^2)/4} \hat{D}(\frac{y+ip}{\sqrt{2}})
\end{aligned} \tag{A.5}$$

relabelling the variable 'y'' $\rightarrow$ 'x' concludes the proof of the lemma■

A.2 Including dark counts

In the following we describe how dark counts (c.f. Sec. 2.3.2) during entanglement swapping can be taken into account by incorporating them in the Bogoliubov transformation for storage and retrieval given in Sec. 3.2.2. We generate the dark counts by introducing a virtual squeezing operation which injects extra excitations into the entanglement swapping setup. Hence the calculation below is at the same time an example of how squeezed input states can be treated in our generating function formalism, as mentioned at the end of Sec. 3.2.1.

As illustrated in Fig. 3.1b, transmission loss during entanglement connection is modelled by a virtual beam splitter with transmission η_{con}. To model dark counts a virtual two-mode squeezing source is introduced. Tracing out one squeezed mode leaves a thermal state in the other, which is then injected at the empty port of the beam splitter. Denoting the memory Bogoliubov transformation (3.22) by U_{mem} and the squeezed modes by s_1 and s_2, the new Bogoliubov transformation including squeezing is given by $U(\eta_{con})U_{mem}\hat{S}_{s_1s_2}(s)$, where $U(\eta_{con})$ is a beam splitter transformation. For $s = e^{2r}$, the output modes with and without squeezing are related by

$$\begin{aligned}
\hat{a}_1'' &= \hat{S}_{s_1s_2}(s) U^\dagger(\eta_{con})\, \hat{a}_1'\, U(\eta_{con}) \hat{S}^\dagger_{s_1s_2}(s) \\
&= \sqrt{\eta_{con}}\, \hat{a}_1' + \sqrt{1-\eta_{con}}\, (\hat{a}_{s_1} \cosh r - \hat{a}^\dagger_{s_2} \sinh r).
\end{aligned} \tag{A.6}$$

The second line follows from (2.29) and (2.31). Applying mode reduction, we can write

$$\hat{a}_1'' = b_1'\hat{a}_1 + c_1'\hat{a}_1^\dagger + b_2'\hat{a}_2' + c_2'\hat{a}_2'^\dagger + c_3'\hat{a}_3'^\dagger, \tag{A.7}$$

where, using (3.21)

$$b_2'\hat{a}_2' = \sqrt{\eta_{con}}\, b_2\hat{a}_2 + \sqrt{1-\eta_{con}}\cosh(r)\,\hat{a}_{s_1}, \tag{A.8}$$

$$c_2'\hat{a}_2'^{\dagger} + c_3'\hat{a}_3'^{\dagger} = \sqrt{\eta_{con}}\,(c_2\hat{a}_2^{\dagger} + c_3\hat{a}_3^{\dagger}) - \sqrt{1-\eta_{con}}\sinh(r)\hat{a}_{s_2}^{\dagger}. \tag{A.9}$$

Choosing $b1', b2', c3'$ real and positive and using the canonical commutators, we find the primed coefficients to be

$$b_1' = \sqrt{\eta_{con}}\, b_1 \tag{A.10}$$

$$b_2' = \sqrt{\eta_{con} b_2^2 + (1-\eta_{con})\cosh^2(r)} \tag{A.11}$$

$$c_1' = \sqrt{\eta_{con}}\, c_1 \tag{A.12}$$

$$c_2' = \eta_{con} b_2 c_2 / b_2' \tag{A.13}$$

$$c_3' = \sqrt{\eta_{con}(|c_2|^2 + c_3^2) + (1-\eta_{con})\sinh^2(r) - |c_2'|^2}. \tag{A.14}$$

It remains to relate the parameters η_{con} and s to the physical dark count rate. Tracing out mode s_2 from the state $\hat{S}_{s_1 s_2}(s)$ leaves mode s_1 in a thermal state of mean photon number $\sinh^2(r)$ (see e.g. Ref. [4] p. 76). The average number of dark counts must equal the mean photon number at the detector due to the virtual squeezing, and we therefore get $\bar{n}_{dc} = (1-\eta_{con})\sinh^2(r)$. To obtain a final expression for the Bogoliubov transformation including dark counts we rewrite (A.10) in terms of the physical parameter $\bar{n}_{dc}$, and since here we are only interested in introducing dark counts but not photon loss to the memory output mode we let $\eta_{con} \to 1$ while keeping $\bar{n}_{dc}$ constant. The result is

$$b_1' = b_1 \tag{A.15}$$

$$b_2' = \sqrt{b_2^2 + \bar{n}_{dc}} \tag{A.16}$$

$$c_1' = c_1 \tag{A.17}$$

$$c_2' = b_2 c_2 / b_2' \tag{A.18}$$

$$c_3' = \sqrt{|c_2|^2 - |c_2'|^2 + c_3^2 + \bar{n}_{dc}}. \tag{A.19}$$

Note that since we have chosen to include the dark counts in the memory transformation, attention should be payed to keeping the dark count rate fixed for non-zero photon loss ($\eta_{con} < 1$).

A.3 Bell parameter as figure of merit

In Chap. 3 we have used the postselected fidelity as a figure of merit for the quality of the states generated by the repeater. In our published work [15] a different quantity known as a Bell parameter was used. Here we provide a link to that work.

A.3.1 The CHSH Bell parameter

The Bell parameter $S(\hat{\rho})$ for a state $\hat{\rho}$ is related to the so-called Clauser-Horne-Shimony-Holt (CHSH) inequality [33] which is a variant of Bell's inequality [6].

It can be used as a measure of the amount of entanglement in a pair of two-level systems, i.e. a pair of qubits.

$S(\hat{\rho})$ is defined in terms of correlations between measurement performed on the two qubits in the following way. Let $|0\rangle$ and $|1\rangle$ denote qubit basis states and define a rotated basis by $|0_\phi\rangle = \cos(\phi)|0\rangle + \sin(\phi)|1\rangle$ and $|1_\phi\rangle = -\sin(\phi)|0\rangle + \cos(\phi)|1\rangle$. Consider projective measurements of the qubits onto different rotated bases with angles ϕ_L and ϕ_R and let $P_{same}(\phi_L, \phi_R)$, $P_{diff}(\phi_L, \phi_R)$ denote respectively the probability that both measurements yield 0 or both 1 and the probability that one yields 0 and the other 1 or vice versa, given the state $\hat{\rho}$. Define $C(\phi_L, \phi_R) = P_{same}(\phi_L, \phi_R) - P_{diff}(\phi_L, \phi_R)$. Then

$$S(\hat{\rho}) = \max_{\phi_R, \phi_R, \phi'_L, \phi'_R} C(\phi_L, \phi_R) - C(\phi_L, \phi'_R) + C(\phi'_L, \phi_R) + C(\phi'_L, \phi'_R). \tag{A.20}$$

That is, $S(\hat{\rho})$ is a function of the correlations between measurement outcomes in four different experiments. Quantum mechanically, the probabilities above are given by

$$P_{same}(\phi_L, \phi_R) = \langle 0_{\phi_L}, 0_{\phi_R}|\hat{\rho}|0_{\phi_L}, 0_{\phi_R}\rangle + \langle 1_{\phi_L}, 1_{\phi_R}|\hat{\rho}|1_{\phi_L}, 1_{\phi_R}\rangle, \tag{A.21}$$

$$P_{diff}(\phi_L, \phi_R) = \langle 0_{\phi_L}, 1_{\phi_R}|\hat{\rho}|0_{\phi_L}, 1_{\phi_R}\rangle + \langle 1_{\phi_L}, 0_{\phi_R}|\hat{\rho}|1_{\phi_L}, 0_{\phi_R}\rangle, \tag{A.22}$$

and one can show, that the range of $S(\hat{\rho})$ is

$$-2\sqrt{2} \leq S(\hat{\rho}) \leq 2\sqrt{2}. \tag{A.23}$$

On the other hand, as demonstrated by Clauser *et al*. [33], any local hidden variable theory must obey the CHSH inequality which stipulates that $|S(\hat{\rho})| \leq 2$. Since it is trivial to construct a local hidden variable theory for any separable state, it follows that $\hat{\rho}$ is entangled whenever $|S(\hat{\rho})| > 2$. The amount by which $S(\hat{\rho})$ exceeds the threshold can be used as a measure of the amount of entanglement. For the maximally entangled Bell states, $S(\hat{\rho}) = 2\sqrt{2}$ as one might expect.

A.3.2 Postselection and fixed angles

In the context of single-rail entanglement and postselection, the probabilities $P_{same}(\phi_L, \phi_R)$ can be defined as the conditional probabilities that both upper or both lower detectors of Fig. 2.9 click given that exactly one click occurs on each side. Similarly $P_{diff}(\phi_L, \phi_R)$ is the conditional probability for one upper and one lower detector to click. $S(\hat{\rho})$ then quantifies how much the CHSH inequality is broken in a postselected Bell experiment.

In our paper, a simplification was introduced to avoid the cumbersome maximisation over angles in (A.20). Since we know that the ideal state produced by the repeater in the absence of imperfections is $|\Psi_2^+\rangle$ (see Sec. 3.1.1), we can evaluate the Bell parameter at the angles which are optimal for this particular state. To first order in small perturbations away from the target state, these angles will still be optimal, as we now prove. Let $\hat{\rho}(\mathbf{x})$ denote a perturbation away from the ideal state with $\hat{\rho}(\mathbf{0}) = |\Psi_2^+\rangle\langle\Psi_2^+|$ for some parametrisation $\mathbf{x} = (x_1, \ldots, x_k)$. Let

$\boldsymbol{\phi} = (\phi_L, \phi_R, \phi'_L, \phi'_R)$, let $\boldsymbol{\phi}^0$ denote the optimal angles for $\mathbf{x} = \mathbf{0}$ and let $S(\mathbf{x}, \phi)$ denote the right-hand side of (A.20) without maximisation. Then the angles which optimise $S(\mathbf{x}, \boldsymbol{\phi})$ will also be close to $\boldsymbol{\phi}^0$ and to first order we can write

$$\begin{aligned} S(\mathbf{x}, \boldsymbol{\phi}) &= 2\sqrt{2} + \sum_{i=1}^{k} x_i \left[\frac{\partial S}{\partial x_i}\right]_{\mathbf{0},\boldsymbol{\phi}^0} + \sum_{i=1}^{4} (\phi_i - \phi_i^0) \left[\frac{\partial S}{\partial \phi_i}\right]_{\mathbf{0},\boldsymbol{\phi}^0} \\ &= 2\sqrt{2} + \sum_{x_i} x_i \left[\frac{\partial S}{\partial x_i}\right]_{\mathbf{0},\boldsymbol{\phi}^0} = S(\mathbf{x}, \boldsymbol{\phi}^0), \end{aligned} \tag{A.24}$$

where we have used that $\hat{\rho}(\mathbf{0})$ is maximally entangled and that $S(\mathbf{0}, \boldsymbol{\phi})$ has a maximum at $\boldsymbol{\phi} = \boldsymbol{\phi}^0$. The optimal angles for the state $|\Psi_2^+\rangle$ are $\boldsymbol{\phi}^0 = (\frac{\pi}{2}, \frac{\pi}{4}, 0, -\frac{\pi}{4})$. Using this, the analog of (3.3) for the Bell parameter becomes

$$\frac{S}{2\sqrt{2}} = \frac{\langle vac|\hat{a}_L \hat{b}_R \,\hat{\rho}\, \hat{b}_L^\dagger \hat{a}_R^\dagger|vac\rangle + \langle vac|\hat{b}_L \hat{a}_R \,\hat{\rho}\, \hat{a}_L^\dagger \hat{b}_R^\dagger|vac\rangle}{\mathrm{tr}\, P_{ps}\, \rho\, P_{ps}}, \tag{A.25}$$

where the postselection projector P_{ps} is given by (3.5).

Perturbative results for the Bell parameter

In the paper [15] analytical, perturbative results are given for the Bell parameter in the presence of memory imperfections, finite initial squeezing and dark counts. The results are expressed in terms of the probabilities $1 - \eta_{gen}$ and $1 - \eta_{con}$ for photon loss during entanglement generation and swapping (denoted p_{gen} and p_{con} in the paper). Rewriting the formulae in terms of η_{gen} and η_{con} one obtains exactly the same form for the errors in $S/2\sqrt{2}$ as we have obtained for the postselected fidelity F in Sec. 3.3.1, up to numerical factors of order 1.

Appendix B

Supplement to Chapter 4

B.1 Retrieval loss

Here we outline a derivation of the expression (4.14). The derivation is based on Ref. [57] and is due to A. Gorshkov. We consider retrieval from the symmetric spin wave in an atomic Λ-system and treat the problem in a one-dimensional approximation. The atomic ground state is denoted $|g\rangle$, the excited state $|e\rangle$ and the metastable level $|s\rangle$ as usual. The system is described in terms of slowly varying time- and position-dependent operators $\mathcal{E}(z,t)$ for the retrieved field, $S(z,t)$ for the spin wave, and $P(z,t)$ for the atomic polarisation. They are defined by (see Ref. [57] for details)

$$\mathcal{E}(z,t) = \sqrt{\frac{l}{2\pi c}} \int d\omega \hat{a}_\omega(t) e^{i\omega z/c}, \tag{B.1}$$

$$S(z,t) = \frac{\sqrt{N}}{N_z} \sum_j \hat{\sigma}_{ge}^{(j)}(t) e^{i(\omega_{eg}-\Delta)(t-z_j/c)}, \tag{B.2}$$

$$P(z,t) = \frac{\sqrt{N}}{N_z} \sum_j \hat{\sigma}_{gs}^{(j)}(t) e^{i(\omega_{eg}-\omega_{es})(t-z_j/c)}, \tag{B.3}$$

where Δ is the detuning of the classical retrieval field, ω_{ge}, ω_{es} are the atomic transition frequencies and $\sigma_{mm'}^{(j)} = |m\rangle_j\langle m'|$ is the transition operator and z_j the position of the j'th atom. The sums are over all atoms in a thin slice of the ensemble at position z with N_z atoms. The $\hat{a}_\omega$ are annihilation operators for different frequency modes, N is the total number of atoms, l is the length of the ensemble and c is the speed of light. We denote the decay rate from the excited level by γ and the optical depth by d.

For convenience we rescale to dimensionless variables $z \to z/l$ and $t \to \gamma t$ and define a rescaled retrieval duration $\tau = \gamma T$ and Rabi frequency $\chi = \Omega/\gamma$. In Ref. [57] it is shown that under resonant retrieval (note that the definitions of Ω, γ and d used in [57] are all smaller by a factor of 2 than the traditional definitions

used here)

$$\partial_z \mathcal{E} = i\sqrt{\frac{d}{2}}P, \tag{B.4}$$

$$\partial_t P = -\frac{1}{2}P + i\frac{1}{2}\sqrt{\frac{d}{2}}\mathcal{E} + i\frac{1}{2}\chi S, \tag{B.5}$$

$$\partial_t S = i\frac{1}{2}\chi P. \tag{B.6}$$

For times $T \sim \gamma/\Omega^2 \gg 1/\gamma d$, adiabatical elimination of the polarisation P is a good approximation and we can therefore take $\partial_t P$ to be zero. We then find from (B.4)-(B.6)

$$\begin{aligned} 2\int_0^\tau dt \int_0^1 dz |P(z,t)|^2 &= -\int_0^\tau dt \int_0^1 dz \left(\mathcal{E}\partial_z\mathcal{E}^* + \mathcal{E}^*\partial_z\mathcal{E} + S\partial_t S^* + S^*\partial_t S\right) \\ &= -\int_0^\tau dt \left[|\mathcal{E}(z,t)|^2\right]_{z=0}^{z=1} - \int_0^1 dz \left[S(z,t)|^2\right]_{t=0}^{t=\tau}. \end{aligned} \tag{B.7}$$

We rewrite this using that, since there can be no retrieved field at the beginning of the sample, $\mathcal{E}(0,t) = 0$, and since all of the excitation is initially stored in the spin wave, $\int_0^1 dz|S(z,0)|^2 = 1$.

$$1 - \int_0^1 dz|S(z,\tau)|^2 = \int_0^\tau dt|\mathcal{E}(1,t)|^2 + 2\int_0^\tau dt \int_0^1 dz|P(z,t)|^2. \tag{B.8}$$

This equation expresses that the total fraction of spin wave lost after a duration $T = \tau/\gamma$ is given by a part which is retrieved into the forward mode plus a part which decays spontaneously in all directions, as claimed in Sec. 4.3.

We now find the two loss terms on the right-hand side of (B.8) in terms of the group velocity. We denote the terms by $A_\mathcal{E}$ and A_P.

$$A_\mathcal{E} = \int_0^\tau dt|\mathcal{E}(1,t)|^2, \qquad A_P = 2\int_0^\tau dt \int_0^1 dz|P(z,t)|^2. \tag{B.9}$$

Under the assumption of adiabatic elimination, the retrieval equations (B.4)-(B.6) can be solved exactly. One obtains

$$\mathcal{E}(z,t) = -\chi\sqrt{\frac{d}{2}}\int_0^z dz' S(z-z',0)e^{-\frac{1}{2}(\chi^2 t + dz')} I_0(\sqrt{\chi^2 t dz'}), \tag{B.10}$$

$$S(z,t) = e^{-\frac{1}{2}\chi^2 t}S(z,0) + \int_0^z dz' S(z-z',0)e^{-\frac{1}{2}(\chi^2 t+dz')}\sqrt{\frac{\chi^2 td}{4z'}} I_1(\sqrt{\chi^2 t dz'}), \tag{B.11}$$

$$P(z,t) = i\chi S(z,t) + i\sqrt{\frac{d}{2}}\mathcal{E}(z,t). \tag{B.12}$$

We are retrieving from the symmetric, flat spin wave which has $S(z,0) = 1$. This allows the expressions for $A_\mathcal{E}$ and A_P to be simplified somewhat. With a change of integration variables to $x = \sqrt{\chi^2 t dz'}$, $y = dz$, and $u = \chi^2 t$ we get

$$A_\mathcal{E} = \frac{2}{d}\int_0^{\frac{1}{2}\chi^2\tau} du \frac{1}{u^2}\left(\int_0^{\sqrt{ud}} dx x e^{-\frac{1}{2}(u+x^2/u)} I_0(x)\right)^2 \tag{B.13}$$

$$A_P = \frac{2}{d}\int_0^{\frac{1}{2}\chi^2\tau} du e^{-u}\int_0^d dy \left(1 + \int_0^{\sqrt{uy}} dx x e^{-x^2/2u}[I_1(x) - \frac{x}{u}I_0(x)]\right)^2 \tag{B.14}$$

In the limit of large optical depth (taking d in the integral limits to infinity) this can be evaluated and using the expression $v_g = \Omega^2 l/d\gamma$ for the group velocity we obtain

$$A_{\mathcal{E}} = \frac{\chi^2\tau}{d} = \frac{v_g T}{l}, \tag{B.15}$$

$$A_P = \frac{v_g T}{l} e^{-\Omega^2 T/2\gamma} \left[I_0(\Omega^2 T/2\gamma) + I_1(\Omega^2 T/2\gamma) \right], \tag{B.16}$$

which confirms (4.14) as promised.

B.2 Spin wave mismatch

Here we estimate the spin wave mismatch incurred during entanglement generation in the protocol of Chap. 4. For simplicity we consider just two segments, i.e. one central node C which is to be entangled with a neighbour L on the left and a neighbour R on the right. We imagine that entanglement between L and C has successfully been established using the level $|s_1\rangle$ such that the (unnormalised) state of the system is

$$\left(\frac{1}{\sqrt{N}} \sum_{j=1}^{N} |s_1\rangle_j\langle g| + \hat{s}_L^\dagger \right) |vac\rangle, \tag{B.17}$$

where $\hat{s}_L^\dagger$ creates a spin wave in L and $|vac\rangle$ is the state with all atoms of L, C and R in the ground state $|g\rangle$. Failed attempts at establishing entanglement between C and R using the level $|s_2\rangle$ will impact (B.17). We assume that the power of the classical write laser is the same in each generation attempt. For every attempt there is then a fixed probability p_g per atom to scatter a photon on the g-e transition, projecting the atom into $|g\rangle$, and a fixed probability p_s to emit a Stokes photon on the e-s_2 transition, projecting the atom into $|s_2\rangle$. We further assume that following each failed attempt, any population present in $|s_2\rangle$ can be effectively removed either by shelving or by ejecting the atoms from the ensemble.

We introduce integers n_g and n_s representing respectively the number of atoms which have been projected into $|g\rangle$ and $|s_2\rangle$ by scattering events, and we define a state

$$|\psi(n_g, n_s)\rangle = \frac{1}{\sqrt{2N - n_g - n_s}} \left(\sum_{j=1}^{N-n_g-n_s} |s_1\rangle_j\langle g| + \sqrt{N}\hat{s}_L^\dagger \right) |vac\rangle_{N-n_s}, \tag{B.18}$$

where the notation indicates that ensemble C has only $N - n_s$ atoms. Note that $|\psi(0,0)\rangle$ equals (B.17). If we keep track of which particular atoms have scattered a photon and number the atoms appropriately, then failed entanglement generation attempts preserve this form of the state, changing only n_g and n_s. Scattering of a photon on the g-e transition either leaves the system unchanged or takes $n_g \to n_g + 1$ depending on whether the atom involved has previously scattered a photon or not. Emission of a Stokes photon takes $n_s \to n_s + 1$ and either

$n_g \to n_g$ or $n_g \to n_g - 1$. Thus the state just before entanglement generation for the second link succeeds is given by $|\psi(n_g, n_s)\rangle$ for some n_g, n_s. A successful generation attempt leads to the state

$$\begin{aligned} &\frac{1}{\sqrt{N-n_g-n_s}}\left(\sum_{j=1}^{N-n_g-n_s}|s_1\rangle_j\langle g| + \sqrt{N}\hat{s}_L^\dagger\right)\times \\ &\frac{1}{\sqrt{N-n_s}}\left(\sum_{j=1}^{N-n_s}|s_2\rangle_j\langle g| + \sqrt{N}\hat{s}_R^\dagger\right)|vac\rangle_{N-n_s}. \end{aligned} \tag{B.19}$$

All $N - n_s$ atoms of ensemble C are part of the s_2-spin-wave, but only $N - n_g - n_s$ of them are also part of the s_1-spin-wave. Successful entanglement swapping consists in a beam-splitter-like transformation (4.11) followed by measurements of the storage level populations. If we assume outcomes one in $|s_1\rangle$ and zero in $|s_2\rangle$ and average over which atom is found in $|s_1\rangle$, the normalised output state becomes a mixture

$$\frac{N-n_g-n_s}{N-n_s}\frac{1}{2}(\hat{s}_L^\dagger + \hat{s}_R^\dagger)|vac\rangle\langle vac|(\hat{s}_L + \hat{s}_R) + \frac{n_g}{N-n_s}\hat{s}_L^\dagger|vac\rangle\langle vac|\hat{s}_L. \tag{B.20}$$

The first term is a perfectly entangled state, for which the postselected fidelity is 1, while the second term is a separable state with postselected fidelity $1/2$. Hence the fidelity of the output state is

$$F(n_g, n_s) = \frac{N-n_g-n_s}{N-n_s} + \frac{n_g}{N-n_s}\times\frac{1}{2} = 1 - \frac{1}{2}\frac{n_g}{N-n_s}. \tag{B.21}$$

By finding average values attained by n_g and n_s before entanglement generation for the second link succeeds and inserting these values in (B.21), we can estimate the impact of spin wave mismatch. We let $\bar{n}_g(k)$ and $\bar{n}_s(k)$ denote the averages of n_g and n_s over many realisations as functions of the number of generation attempts. The averages must obey the recursion equations

$$\bar{n}_g(k+1) = \bar{n}_g(k) + p_g\left[N - \bar{n}_g(k) - \bar{n}_s(k)\right] - p_s\bar{n}_g(k), \tag{B.22}$$

$$\bar{n}_s(k+1) = \bar{n}_s(t) + p_s\left[N - \bar{n}_s(k)\right]. \tag{B.23}$$

These equations are easily solved, subject to the initial condition $\bar{n}_g(0) = \bar{n}_s(0) = 0$. One finds

$$\bar{n}_g(k) = \left[(1-p_s)^k - (1-p_g-p_s)^k\right]N \approx kp_gN, \tag{B.24}$$

$$\bar{n}_s(k) = \left[1-(1-p_s)^k\right]N \approx kp_sN, \tag{B.25}$$

where the approximations are valid for small excitation probabilities $p_g, p_s \ll 1/k$. Now, if the branching ratios for decay from $|e\rangle$ to $|s_2\rangle$ and to $|g\rangle$ are β and $1-\beta$ respectively and the combined efficiency of collection, transmission and detection during entanglement generation is η, then the probability for a generation attempt to succeed is $(N-n_s)\eta\beta p_g/(1-\beta)$. To first order in the excitation probabilities, we can drop n_s from this expression and take the average

number of failed attempts before generation succeeds to be $\bar{k} = (1-\beta)/\beta\eta p_g N$. Assuming that $\beta\eta N \gg 1$ and inserting into the solutions for $\bar{n}_g$ and $\bar{n}_s$ we find

$$\bar{n}_g(\bar{k}) \approx \frac{1-\beta}{\beta\eta}, \tag{B.26}$$

$$\bar{n}_s(\bar{k}) \approx \frac{1-\beta}{\beta\eta}\,\frac{p_s}{p_g} = \frac{1}{\eta}. \tag{B.27}$$

Using these results and the expression for the fidelity $F(n_g, n_s)$ above, we find the average value

$$F = 1 - \frac{1}{2}\frac{1-\beta}{\beta\eta}. \tag{B.28}$$

This confirms Eq. (4.18).

B.3 PIR in free space with high Fresnel number

Here we give a rough lower bound on the number of modes which are not cleared of undesired incoherent excitations by PIR for an ensemble in free space in the limit of high Fresnel number.

For simplicity, we consider an elliptical ensemble of constant density with major axis l and minor axis $\sqrt{A}$. For light with wavelength λ, the Fresnel number is then $\mathcal{F} = A/\lambda l$. The symmetric spin-wave is retrieved along the major axis and the optical depth along this axis is d. We denote the optical depth along a direction making an angle θ with the major axis by d_θ. Thus $d_0 = d$. The decay rate from an atomic mode which is retrieved at an angle θ is then $\sim \Omega^2/\gamma d_\theta$. After retrieval for a duration T, a fraction $\delta = 2\Omega^2 T/\gamma d$ of the symmetric spin-wave is lost according to (4.14). The fraction f of excitations left in other modes is found by summing over modes with non-zero θ

$$f = \left(\sum_{\mathbf{k}_\theta, \theta\neq 0} e^{-\frac{1}{2}\delta d/d_\theta}\right) / \left(\sum_{\mathbf{k}_\theta, \theta\neq 0} 1\right). \tag{B.29}$$

Since the atomic cloud is elliptical, we have

$$\left(\frac{d_\theta}{d}\right)^2 = \frac{1}{l^2} \times \frac{1+\tan^2(\theta)}{1/l^2 + \tan^2(\theta)/A}. \tag{B.30}$$

For small angles and an elongated ensemble with large aspect ratio, i.e. $\theta^2 \ll A/l^2$ and $1 \ll l^2/A$, we can approximate

$$d_\theta \approx \frac{1}{2}\left(1 - \theta^2\frac{l^2}{2A}\right) d. \tag{B.31}$$

Motivated by our definition of the density, which is constant inside our ellipsis and zero outside, we take the quantisation volume in the transverse direction to be set by A. We can then replace the sum in (B.29) by an integral over the transverse component of the $\mathbf{k}$-vectors. That is, we replace

$$\sum_{\mathbf{k}_\theta, \theta\neq 0} \to \frac{A}{(2\pi)^2}\int d^2k_\perp. \tag{B.32}$$

For small angles, the length of $\mathbf{k}_\perp$ is related to θ by

$$k_\perp = k\sin(\theta) = \frac{2\pi\sin(\theta)}{\lambda} \approx \frac{2\pi\theta}{\lambda}. \tag{B.33}$$

Considering only near-parallel modes with $\theta^2 < A/l^2$, the numerator in (B.29) becomes

$$\begin{aligned}\frac{A}{(2\pi)^2}\int_0^{2\pi\sqrt{A}/l\lambda} d^2k_\perp e^{-\delta(1+\frac{1}{2}\left(\frac{\lambda k_\perp}{2\pi}\right)^2\frac{l^2}{A})} &= \frac{A}{\lambda^2}\int_0^{\sqrt{A}/l} d\theta\theta e^{-\delta(1+\frac{l^2}{2A}\theta^2)} \\ &= \frac{e^{-3\delta/2}(e^{\delta/2}-1)}{\delta}\mathcal{F}^2,\end{aligned} \tag{B.34}$$

and the denominator becomes

$$\frac{A}{(2\pi)^2}\int_0^{2\pi\sqrt{A}/l\lambda} 1 d^2k_\perp = \frac{1}{2}\mathcal{F}^2. \tag{B.35}$$

This expression measures the number of near-parallel modes which we have taken into account. We note that there may be modes with $\theta^2 \geq A/l^2$ which can still be considered near-parallel. However, we are only trying to lower bound the number of modes which are not cleared by PIR and hence $\theta^2 < A/l^2$ is sufficient. For PIR to make sense, most of the symmetric spin wave must be retained, δ is therefore small and the fraction of excitations left becomes

$$f \approx \frac{2}{\delta}e^{-3\delta/2}(e^{\delta/2}-1) \approx 1 - \frac{5}{4}\delta. \tag{B.36}$$

We thus see that PIR in free space does *not* clean out unwanted excitations in the near parallel modes. Since we are working in the limit of high Fresnel number, the total number of near-parallel modes (B.35) is large and the probability for incoherent spin-wave excitation even after PIR may be significantly higher than the multiexcitation probability with full retrieval. We conclude that PIR in free space does not work well. The ensemble must be placed in a cavity or other photonic structure to enable good PIR. In a single-mode hollow-core photonic crystal fibre for example, there is a bandgap suppressing near-parallel modes. Only the guided mode and near-transversal modes are present [36, 47, 105, 108].

B.4 Fluorescence-based dual-rail repeater

In Chap. 4 we presented rate simulations of a dual-rail quantum repeater with fluorescence detection based on a dual-rail architecture with retrieval and single-photon detection proposed by Jiang and coworkers [72]. Here we provide a brief sketch of that protocol and explain how it can be mapped to a fluorescence-based scheme. The basic ingredients are the same as for the single-rail DLCZ protocol, but the entanglement swapping setup is somewhat more involved and, crucially, now depends on coincident detection of two photons.

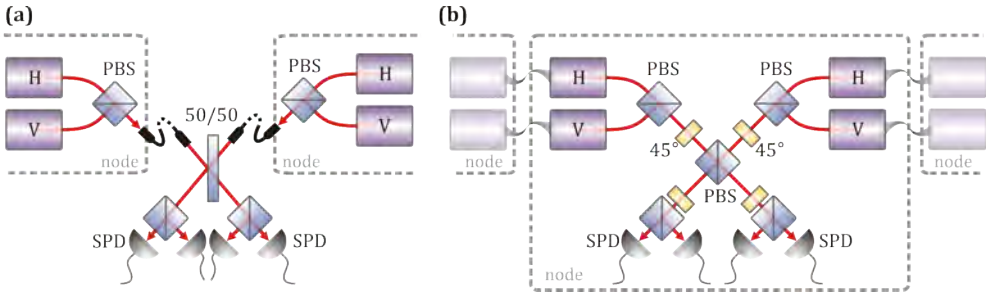

Figure B.1: Setup for the dual-rail scheme proposed by Jiang *et al.* [72]. **(a)** Entanglement generation as in the DLCZ scheme, but with two pairs prepared in parallel. H/V indicates polarisation of retrieved light, PBS polarising beam splitters. **(b)** Entanglement swapping. First two 45° polarisation rotations inserted the first level of swapping only. The left and right hand outputs of the central beam splitter are measured in the basis $|\pm\rangle = (|H\rangle \pm |V\rangle/\sqrt{2}$. Successful swapping is conditioned on exactly one click on each side of the central beam splitter.

B.4.1 Retrieval-based dual-rail scheme

The proposal by Jiang *et al.* [72] employs four atomic ensembles at each repeater node (except the end nodes). Each ensemble corresponds to a single (spin-wave) mode, and an entangled link always contains two excitations stored in different ensembles. The setups for entanglement generation and swapping are shown in Fig. B.1. Entanglement generation is achieved by the same basic scheme as in the DLCZ protocol, described in Sec. 2.4.2 with atomic spin-waves generated by Raman scattering as explained in Sec. 4.1. However, here two pairs of entangled ensembles are created in parallel between the same nodes. The generated state is

$$\frac{1}{2}\left(\hat{a}^\dagger_{LH} + \hat{a}^\dagger_{RH}\right)\left(\hat{a}^\dagger_{LV} + \hat{a}^\dagger_{RV}\right)|vac\rangle + O(\sqrt{p}), \tag{B.37}$$

where p is the excitation probability and (referring to Fig. B.1) L, R denote left and right ensembles and H, V denote upper and lower ensembles. Entanglement swapping relies on two-photon detection. The atomic modes of all four ensembles within a given node are retrieved onto light and subjected to a linear optical transformation followed by detection. The first level of entanglement swapping converts (B.37) into a dual-rail entangled state of the form (neglecting higher-order terms)

$$\frac{1}{\sqrt{2}}\left(\hat{a}^\dagger_{LH}\hat{a}^\dagger_{RH} + \hat{a}^\dagger_{LV}\hat{a}^\dagger_{RV}\right)|vac\rangle. \tag{B.38}$$

It was demonstrated in Ref. [72] that in this protocol, the vacuum component of the entangled states remains constant under entanglement swapping and that multiexcitation errors grown only linearly. As a consequence the rate scales significantly better than in the DLCZ protocol, which suffers from a rapid growth of the vacuum component and quadratic scaling of multiexcitation errors as seen in Secs. 3.3.3 and 3.3.1. In addition, Ref. [72] also included an entanglement purification scheme based on linear optics, which allows high fidelity to be maintained in the presence of other errors such as phase drifts.

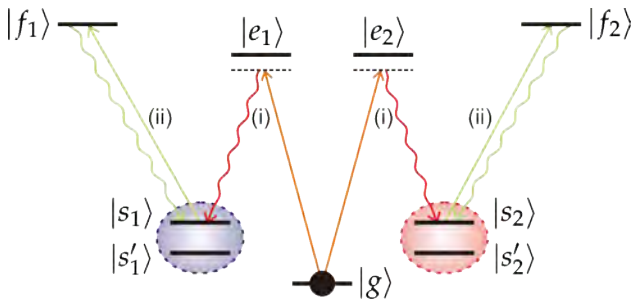

FIGURE B.2: Atomic level scheme for a dual-rail implementation. There are four the encircled meta-stable storage levels. Spin-waves are generated via the Raman transitions (i). The populations of the storage levels can be measured using the cycling transitions (ii). All atoms are initialised in the ground state, and the system remains close to this fully polarised state at all times.

B.4.2 Mapping to fluorescence-based scheme

By introducing two additional levels with respect to the single-rail levels scheme of Fig. 4.3, it is possible to find a one-to-one mapping of the scheme proposed by Jiang *et al.* onto a scheme based on fluorescence detection with no need for full retrieval of atomic spin-waves. The level dual-rail level scheme is pictured in Fig. B.2. A node with four ensembles in the scheme of Fig. B.1 is replaced by a single ensemble and the roles of individual ensembles is now played by the four storage levels $|s_1\rangle$, $|s_1'\rangle$, $|s_2\rangle$, and $|s_2'\rangle$. Entanglement generation on the two levels $|s_1\rangle$ and $|s_1'\rangle$ with, say the neighbouring ensemble on the left, proceeds sequentially using the same scheme as the single-rail protocol. Each level is entangled with its neighbouring twin in turn by detection of a Stokes photon on the s_1-e_1 transition. When the first pair has been generated on the levels $|s_1\rangle$, it is shelved by swapping levels $|s_1\rangle$ and $|s_1'\rangle$ and the process is repeated. There is no decay from $|e_1\rangle$ to $|s_1'\rangle$. Once an ensemble is entangled with both its left and right neighbours, entanglement swapping is achieved by implementing transformations of the atomic levels equivalent to the linear optical transformations of Fig. B.1b. For example the 45° polarisation rotations correspond to the transformations

$$|s_i\rangle \to \frac{1}{\sqrt{2}}\left(|s_i\rangle + |s_i'\rangle\right), \qquad |s_i'\rangle \to \frac{1}{\sqrt{2}}\left(|s_i\rangle - |s_i'\rangle\right), \tag{B.39}$$

and similarly for the beam splitters. The final single-photon detections are replaced by fluorescence measurements of the population of all four storage levels.

B.5 Additional rate plots

In this appendix we provide plots demonstrating the behaviour of the fluorescence-based repeater scheme of Chap. 4 for alternative values of the single-photon detection efficiency η_{spd} and the attenuation length L_{att} associated with transmission of Stokes photons during the entanglement generation step of the protocol.

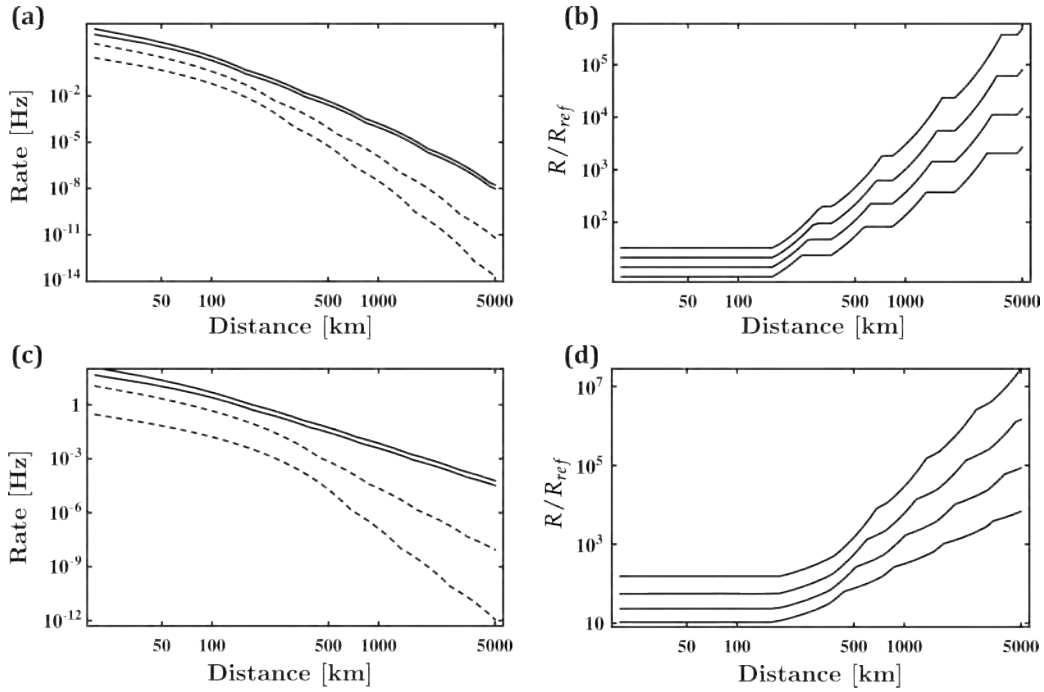

Figure B.3: **(a)** The rates in the new (solid) and DLCZ (dashed) single-rail schemes. The rates are shown for $\eta_{spd} = 0.4$ (upper curve) and 0.7 (lower curve). **(b)** Ratio of the rate in the new single-rail scheme to that of the DLCZ scheme for $\eta_{spd} = 0.4$, 0.5, 0.6, 0.7 (top to bottom). **(c)** The rates in the new dual-rail scheme (solid) and the scheme of Ref. [72]. The rates are shown for $\eta_{spd} = 0.4$ (upper curve) and 0.7 (lower curve). **(d)** Ratio of the rate in the new dual-rail scheme to that of Ref. [72] for $\eta_{spd} = 0.4$, 0.5, 0.6, 0.7 (top to bottom). In all plots $\eta_{fl} = 0.95$, $\eta_{col} = 0.05$, $d = 100$, $L_{att} = 20\,\text{km}$.

The plots show the improvement in rate with respect to the retrieval-based reference schemes and the absolute value of the rate. They supplement Fig. 4.5.

B.5.1 Varying η_{spd}

Fig. B.3 shows the effect of varying η_{spd}. The rates in the fluorescence-based schemes are relatively robust against changes in η_{spd} while the reference scheme rates are more sensitive, because the efficiency of entanglement swapping depends critically on η_{spd}. The relative gain in rate thus increases with decreasing η_{spd} because the reference scheme rates drop.

B.5.2 Varying L_{att}

On the one hand, the attenuation length of optical fibre is quite sensitive to the wavelength of transmitted light. On the other hand, the Stokes photon wavelength employed in a quantum repeater scheme depends on the specifics of the implementation, such as the atomic species and the mapping of reservoir and storage states onto specific atomic levels. Hence the attenuation length relevant for determining the communication rate of the repeater is an implementation-

dependent quantity. As a consequence, it may be that the attenuation lengths relevant the fluorescence-based scheme and the reference schemes are different, and we therefore need to verify that the advantage of our scheme persists when the attenuation length is reduced with respect to that of the reference schemes. Fig. B.4 shows the rate gain with the attenuation length in the fluorescence-based schemes reduced by factors of 2 and 5 relative to that of the reference schemes. From this plot and by comparison to Fig. B.3b and Fig. B.3d we note that the gain is somewhat sensitive to changes in L_{att}. However, significant gains are still obtained even for the reduced values of L_{att}.

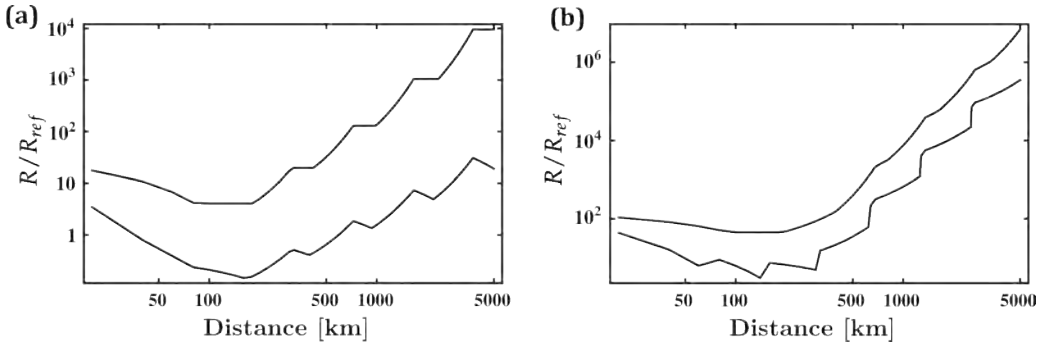

FIGURE B.4: **(a)** Ratio of the rate in the new single-rail scheme to that of the DLCZ scheme. **(b)** Ratio of the rate in the new dual-rail scheme to that of Ref. [72]. In both plots $\eta_{spd} = 0.4$, $\eta_{fl} = 0.95$, $\eta_{col} = 0.05$, $d = 100$ and $L_{att} = 10\,\text{km}$ (top), $4\,\text{km}$ (bottom) in the new schemes and $L_{att} = 20\,\text{km}$ in the reference schemes.

Appendix C

Supplement to to Chapter 5

C.1 Entropy of entanglement for the two-mode cat

A widely used measure of entanglement for pure[1] states is the so-called 'entropy of entanglement' E. It is defined for a bipartite state $\hat{\rho}$ as the von Neumann entropy of the reduced density matrices $\hat{\rho}_{\mathcal{A}} = \mathrm{tr}_{\mathcal{B}}\,\hat{\rho}$ and $\hat{\rho}_{\mathcal{B}} = \mathrm{tr}_{\mathcal{A}}\,\hat{\rho}$ where $\mathcal{A}$, $\mathcal{B}$ label the two subsystems. Intuitively, the more entangled the state of the total system becomes, the more mixed the subsystem states become due to their interconnectedness, and thus the entropy which measures 'disorder' increases. Formally

$$E(\rho) = \mathrm{tr}[\rho_{\mathcal{A}} \log_2 \rho_{\mathcal{A}}] = \sum_i \lambda_i \log_2 \lambda_i, \tag{C.1}$$

where λ_i are the eigenvalues of $\hat{\rho}_{\mathcal{A}}$ and we take $0 \log_2 0 = 0$. The definition makes sense since by the Schmidt decomposition, λ_i are also the eigenvalues of of $\hat{\rho}_{\mathcal{B}}$ ([98] p.109). Thus $E(\hat{\rho})$ only depends on $\hat{\rho}$ and on the choice how the system is partitioned. The range of $E(\hat{\rho})$ is

$$0 \leq E(\hat{\rho}) \leq \log_2 d, \tag{C.2}$$

where d is the smaller of the dimensions of $\hat{\rho}_{\mathcal{A}}$ and $\hat{\rho}_{\mathcal{B}}$. Equality in the first inequality $E(\hat{\rho}) = 0$ is achieved if and only if $\hat{\rho}$ is separable. Conversely, when $E(\hat{\rho}) = \log_2 d$ the state is said to be maximally entangled. In particular, when the system consists of two qubits, a maximally entangled state has $E(\hat{\rho}) = 1$. Taking the logarithm to base 2, the amount of entanglement is sometimes referred to as measured in 'ebits'.

It is easy to see that the Bell states are maximally entangled in the sense of maximising E. As a slightly more interesting example, let us compute the amount of entanglement in the two-mode cat state (2.26). The easiest approach is to rewrite the state in terms of the orthonormal single-mode cat states $|\pm\rangle =$

[1] An entanglement measure must obey monotonicity – it should not be possible to increase the measure by local operations and classical communication. The entropy of entanglement is not an entanglement monotone for mixed states.

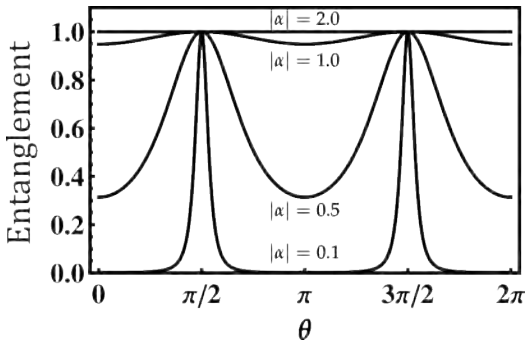

FIGURE C.1: Entanglement in ebits as a function of phase for the two-mode cat state.

$\mathcal{N}_\pm(|\alpha\rangle \pm |-\alpha\rangle)$, where $\mathcal{N}_\pm = (2 \pm 2e^{-2|\alpha|^2})^{-1/2}$. In terms of these states

$$\begin{aligned} e^{i\theta}|\alpha,\alpha\rangle + e^{-i\theta}|-\alpha,-\alpha\rangle =& \cos(\theta)\mathcal{N}_+^2|+,+\rangle + i\sin(\theta)\mathcal{N}_+\mathcal{N}_-|-,+\rangle \\ &+ i\sin(\theta)\mathcal{N}_-\mathcal{N}_+|+,-\rangle + \cos(\theta)\mathcal{N}_-^2|-,-\rangle. \end{aligned} \tag{C.3}$$

From this expression we can see that the entanglement in the two-mode cat must depend on the phase θ, at least when α is small. For $\theta = \pi/2$ the two-mode cat equals the Bell state $|+,-\rangle + |-,+\rangle$ for any value of α, but for $\theta = 0$ the expression approaches the separable state $|--\rangle$ when α approaches zero. To quantify the entanglement, we compute the reduced density matrix of one mode from (C.3) in the basis of $|+\rangle$ and $|-\rangle$ and determine the eigenvalues. They are

$$\lambda_\pm = \frac{1}{2} \pm \frac{1}{2}\kappa\frac{\sqrt{\cos^2(\theta)[4 - 2\kappa^2 + 2\kappa^2\cos(2\theta)]}}{1 + \kappa^2\cos(2\theta)}, \tag{C.4}$$

where $\kappa = e^{-2|\alpha|^2}$. The entanglement in the two-mode cat is then $\lambda_+ \log_2(\lambda_+) + \lambda_- \log_2(\lambda_-)$. It is plotted in Fig. C.1 as a function of θ for several values of $|\alpha|$. For small $|\alpha|$, the entanglement does indeed depend strongly on phase. Notice however that for $|\alpha| > 1$, the dependence quickly becomes negligible (at $|\alpha| = 1$ the variation is 0.05 and at $|\alpha| = 2$ it is of order 10^{-7}) and the state essentially always contains 1 ebit of entanglement.

C.2 Target state for the hybrid repeater.

In this section, we find the target state for the hybrid repeater protocol of Chap. 5. We start from the approximate cat states generated in the first step of the protocol. In the limit of low pair production probability and narrow acceptance interval ($p, \Delta \to 0$), the state after m levels of growth is well approximated by the two-mode cat state (5.13). Denoting the two modes by 'a' and 'b', this state has the wavefunction

$$\psi_{0m}(x_a, x_b) = N_{0m}^{-1/2} e^{-\frac{1}{4}(x_a - x_b)^2}\left[e^{-\frac{1}{2}(x_a + x_b - \mu_m)^2} + e^{-\frac{1}{2}(x_a + x_b + \mu_m)^2}\right], \tag{C.5}$$

where $N_{0m} = 2^{-1/2}\pi(1 + e^{-\mu_m^2})$ and $\mu_m = \sqrt{2^m + 1/2}$. To see the effect of entanglement swapping on this state, we must connect two identical copies according

to the setup of Fig. 5.4a. Denoting the variables of the second copy by primes, the (unnormalised) state after swapping with X-measurement outcome zero and P-measurement outcome p is given by

$$\begin{aligned}\tilde{\psi}_{1m}(x_a, x_b') &= \int_{-\infty}^{\infty} dx_b\, e^{-ix_b p} \left[\psi_{0m}(x_a, \frac{x_b + x_a'}{\sqrt{2}})\psi_{0m}(\frac{x_b - x_a'}{\sqrt{2}}, x_b')\right]_{x_a'=0} \\ &= \int_{-\infty}^{\infty} dx_b\, \psi_{0m}(x_a, \frac{x_b}{\sqrt{2}})\psi_{0m}(\frac{x_b}{\sqrt{2}}, x_b')\, e^{-ix_b p}.\end{aligned} \tag{C.6}$$

The function $\psi_{0m}(x_a, x_b)$ has two peaks displaced by $\pm\mu_m/\sqrt{2}$ along the diagonal in (x_a, x_b)-space, and the integrand contains four corresponding terms. If μ_m is sufficiently large, the direct terms coming from products of two peaks displaced in the same direction contribute very little to the zero outcome $x_a' = 0$. The main contribution is due to the cross terms coming from products of two peaks with opposite displacements. We therefore discard the direct terms and keep only the cross terms. Performing the Fourier transformation and simplifying the resulting expression, one then arrives at the expression

$$\begin{aligned}\psi_{1m}(x_a, x_b) = N_{1m}^{-1/2}\, e^{-i\phi(x_a+x_b)} e^{-\frac{3}{8}(x_a-x_b)^2} \times \\ \left[e^{-\frac{1}{3}(x_a+x_b-\mu_m)^2 - i\varphi} + e^{-\frac{1}{3}(x_a+x_b+\mu_m)^2 + i\varphi}\right],\end{aligned} \tag{C.7}$$

where N_{1m} is a normalisation factor, $\phi = \frac{p}{3\sqrt{2}}$, and $\varphi = \frac{2\sqrt{2}}{3}\mu_m p$. Based on this result, and by iterating the calculation a few times, discarding the direct terms in each iteration, we come up with the following ansatz for the state after n levels of entanglement connection

$$\begin{aligned}\psi_{mn}(x_a, x_b) = N_{nm}^{1/2}\, e^{-i(\phi_{a,n}x_a + \phi_{b,n}x_b)} e^{-\frac{k_n}{8}(x_a-x_b)^2} \times \\ \left[e^{-\frac{1}{k_n}(x_a+x_b-\mu_m)^2 - i\varphi_n} + e^{-\frac{1}{k_n}(x_a+x_b+\mu_m)^2 + i\varphi_n}\right].\end{aligned} \tag{C.8}$$

Here $\phi_{a,n}$ and $\phi_{b,n}$ can be interpreted as P-space displacements since $\hat{X}$ is the generator of translations in P-space. The parameter k_n determines the squeezing of the sum and difference quadratures $(\hat{X}_a \pm \hat{X}_b)/\sqrt{2}$, and φ_n is a phase. The initial state (C.5) is clearly of the form (C.8), with $k_0 = 2$ and $\phi_{a,0} = \phi_{b,0} = \varphi_0 = 0$. The ansatz will be confirmed if it is preserved under entanglement swapping. By connecting two copies of ψ_{nm} and computing the output wavefunction as in (C.6), again discarding the direct product terms, one can show after a non-zero amount of tedious maths (we enlisted the assistance of *Mathematica*) that the form of the ansatz is indeed preserved. The parameters fulfil the recursion relations

$$k_{n+1} = \frac{8 + k_n^2}{2k_n}, \tag{C.9}$$

$$\varphi_{n+1} = \frac{8\mu_m}{k_{n+1}k_n}\left(\frac{p}{\sqrt{2}} + \phi_{b,n} + \phi_{a,n}'\right) + \varphi_n + \varphi_n', \tag{C.10}$$

$$\phi_{a,n+1} = \frac{1}{k_{n+1}}\left(\frac{k_n}{4} + \frac{2}{k_n}\right)\left(\frac{p}{\sqrt{2}} + \phi_{b,n} + \phi_{a,n}'\right) + \phi_{a,n}, \tag{C.11}$$

$$\phi_{b,n+1} = \frac{1}{k_{n+1}}\left(\frac{k_n}{4} + \frac{2}{k_n}\right)\left(\frac{p}{\sqrt{2}} + \phi_{b,n} + \phi_{a,n}'\right) + \phi_{b,n}'. \tag{C.12}$$

The solution of the first recursion, with the initial condition $k_0 = 2$, is

$$k_n = 2\sqrt{2}\coth(2^n \operatorname{arccoth}(\frac{1}{\sqrt{2}})). \tag{C.13}$$

The other parameters cannot be put on a closed form, because they depend on the P-measurement outcomes. We can and do, however, keep track of them numerically in our simulations of the repeater protocol.

By evaluation it can be seen that k_n converges fast toward $2\sqrt{2}$. The relative error $(k_n - 2\sqrt{2})/2\sqrt{2}$ is 6%, 0.2%, and 2×10^{-4}% for $n = 1$, 2 and 3. As discussed in Sec. 5.3, this which means that the squeezing can be seen as independent squeezing of the $\hat{X}_a$ and $\hat{X}_b$ quadratures, i.e. it becomes local. From the ansatz, one can then determine a locally squeezed two-mode cat state, which can be used as a target state for the repeater. This was done in (5.28). The fact that we are able to obtain very good fidelities with respect to the chosen target state in our simulations (e.g. for the the plot in Fig. 5.7 the fidelity is > 90%) confirms that the approximations we have made – discarding the direct terms above and taking the limit of local squeezing – are reasonable.

Bibliography

[1] J. Appel, P. J. Windpassinger, D. Oblak, U. B. Hoff, N. Kjærgaard, and E. S. Polzik, "Mesoscopic atomic entanglement for precision measurements beyond the standard quantum limit," *Proceedings of the National Academy of Sciences* **106**, 10960 (2009).

[2] Alain Aspect, Jean Dalibard, and Gérard Roger, "Experimental test of Bell's inequalities using time- varying analyzers," *Phys. Rev. Lett.* **49**, 1804 (1982).

[3] M. Bajcsy, S. Hofferberth, V. Balic, T. Peyronel, M. Hafezi, A. S. Zibrov, V. Vuletic, and M. D. Lukin, "Efficient all-optical switching using slow light within a hollowfiber," *Phys. Rev. Lett.* **102**, 203902 (2009).

[4] S. M. Barnett and P. M. Radmore, *Methods in Theoretical Quantum Optics* (Oxford University Press, 1997).

[5] J. S. Bell, *Speakable and Unspeakable in Quantum Mechanics* (Cambridge University Press, 2004), 2nd edn.

[6] John Bell, "On the Einstein Podolsky Rosen paradox," *Physics* **1**, 195 (1964).

[7] C. H. Bennett and G. Brassard, in "Proceedings of the IEEE International Conference on Computers, Systems and Signal Processing, Bangalore, India," (IEEE, New York, 1984), p. 175.

[8] C. H. Bennett, G. Brassard, C. Crépeau, R. Jozsa, A. Peres, and W. K. Wootters, "Teleporting an unknown quantum state via dual classical and einstein-podolsky-rosen channels," *Phys. Rev. Lett.* **70**, 1895 (1993).

[9] R. Blatt and D. Wineland, "Entangled states of trapped atomic ions," *Nature* **453**, 1008 (2008).

[10] S. Bose, P. L. Knight, M. B. Plenio, and V. Vedral, "Proposal for teleportation of an atomic state via cavity decay," *Phys. Rev. Lett.* **83**, 5158 (1999).

[11] M. M. Boyd, *High Precision Spectroscopy of Strontium in an Optical Lattice: Towards a New Standard for Frequency and Time*, Ph.D. thesis, University of Colorado, USA (2007).

[12] J. B. Brask, *Long Distance Communication with Atomic Quantum Memories*, Master's thesis, Niels Bohr Institute, University of Copenhagen, Denmark (2006).

[13] J. B. Brask, L. Jiang, A. V. Gorshkov, V. Vuletic, A. S. Sørensen, and M. D. Lukin, "Fast entanglement distribution with atomic ensembles and fluorescent detection," *Phys. Rev. A* **81**, 020303 (2010).

[14] J. B. Brask, I. Rigas, E. S. Polzik, U. L. Andersen, and A. S. Sørensen, "A hybrid long-distance entanglement distribution protocol," *arXiv* **quant-ph**, 1004.0083 (2010).

[15] J. B. Brask and A. S. Sørensen, "Memory imperfections in atomic-ensemble-based quantum repeaters," *Phys. Rev. A* **78**, 012350 (2008).

[16] S. L Braunstein, C. A. Fuchs, and H. J. Kimble, "Criteria for continuous-variable quantum teleportation," *Journal of Modern Optics* **47**, 267 (2000).

[17] S. L. Braunstein and H. J. Kimble, "Teleportation of continuous quantum variables," *Phys. Rev. Lett.* **80**, 869 (1998).

[18] Samuel L. Braunstein and Peter van Loock, "Quantum information with continuous variables," *Rev. Mod. Phys.* **77**, 513 (2005).

[19] H.-J. Briegel, W. Dür, J. I. Cirac, and P. Zoller, "Quantum repeaters: The role of imperfect local operations in quantum communication," *Phys. Rev. Lett.* **81**, 5932 (1998).

[20] E. Brion, K. Mølmer, and M. Saffman, "Quantum computing with collective ensembles of multilevel systems," *Phys. Rev. Lett.* **99**, 260501 (2007).

[21] E. Brion, L.H. Pedersen, M. Saffman, and K Mølmer, "Error correction in ensemble registers for quantum repeaters and quantum computers," *Phys. Rev. Lett.* **100**, 110506 (2008).

[22] C. Cabrillo, J. I. Cirac, P. García-Fernández, and P. Zoller, "Creation of entangled states of distant atoms by interference," *Phys. Rev. A* **59**, 1025 (1999).

[23] J. Calsamiglia and N. Lütkenhaus, "Maximum efficiency of a linear-optical bell-state analyzer," *Appl. Phys. B* **72**, 67 (2001).

[24] T. Chanelière, D. N. Matsukevich, S. D. Jenkins, S.-Y. Lan, T. A. B. Kennedy, and A. Kuzmich, "Storage and retrieval of single photons transmitted between remote quantum memories," *Nature* **438**, 833 (2005).

[25] S. Chen, Y.-A. Chen, B. Zhao, Z.-S. Yuan, J. Schmiedmayer, and J.-W. Pan, "Demonstration of a stable atom-photon entanglement source for quantum repeaters," *Phys. Rev. Lett.* **99**, 180505 (2007).

[26] Y.-A. Chen, S. Chen, Z.-S. Yuan, B. Zhao, C.-S.Chuu, J. Schmiedmayer, and J.-W. Pan, "Memory-built-in quantum teleportation with photonic and atomic qubits," *Nature Physics* **4**, 103 (2008).

[27] Z.-B. Chen, B. Zhao, Y.-A. Chen, J. Schmiedmayer, and J.-W. Pan, "Fault-tolerant quantum repeater with atomic ensembles and linearoptics," *Phys. Rev. A* **76**, 022329 (2007).

[28] L. Childress, J. M. Taylor, A. S. Sørensen, and M. D. Lukin, "Fault-tolerant quantum communication based on solid-state photon emitters," *Phys. Rev. Lett.* **96**, 070504 (2006).

[29] L. Childress, J. M. Taylor, A. S. Sørensen, and M. D. Lukin, "Fault-tolerant quantum repeaters with minimal physical resources and implementations based on single-photon emitters," *Phys. Rev. A* **72**, 052330 (2005).

[30] K. S. Choi, H. Deng, J. Laurat, and H. J. Kimble, "Mapping photonic entanglement into and out of a quantum memory," *Nature* **452**, 67 (2008).

[31] C.-W. Chou, J. Laurat, H. Deng, H. Choi, K. S.and de Riedmatten, D. Felinto, and H. J. Kimble, "Functional quantum nodes for entanglement distribution over scalablequantum networks," *Science* **316**, 1316 (2007).

[32] Caleb A. Christensen, Sebastian Will, Michele Saba, Gyu-Boong Jo, Yong-Il Shin, Wolfgang Ketterle, and David Pritchard, "Trapping of ultracold atoms in a hollow-core photonic crystal fiber," *Phys. Rev. A* **78**, 033429 (2008).

[33] J. F. Clauser, M. A. Horne, A. Shimony, and R. A. Holt, "Proposed experiment to test local hidden-variable theories," *Phys. Rev. Lett.* **23**, 880 (1969).

[34] J F Clauser and A Shimony, "Bell's theorem. experimental tests and implications," *Reports on Progress in Physics* **41**, 1881 (1978).

[35] O. A. Collins, S. D. Jenkins, A. Kuzmich, and T. A. B. Kennedy, "Multiplexed memory-insensitive quantum repeaters," *Phys. Rev. Lett.* **98**, 060502 (2007).

[36] R. F. Cregan, B. J. Mangan, J. C. Knight, T. A. Birks, P. St. J. Russell, P. J. Roberts, and D. C. Allan, "Single-mode photonic band gap guidance of light in air," *Science* **285**, 1537 (1999).

[37] M. Dakna, T. Anhut, T. Opatrný, L. Knöll, and D.-G. Welsch, "Generating Schrödinger-cat-like states by means of conditional measurements on a beam splitter," *Phys. Rev. A* **55**, 3184 (1997).

[38] A. J. Daley, M. M. Boyd, J. Ye, and P. Zoller, "Quantum computing with alkaline-earth-metal atoms," *Physical Review Letters* **101**, 170504 (2008).

[39] D. Dieks, "Communication by EPR devices," *Physics Letters A* **92**, 271 (1982).

[40] R. Dong, J. Heersink, J. F. Corney, P. D. Drummond, U. L. Andersen, and G. Leuchs, "Experimental evidence for raman-induced limits to efficient squeezing in optical fibers," *Opt. Lett.* **33**, 116 (2008).

[41] L.-M. Duan, M. D. Lukin, J. I. Cirac, and P. Zoller, "Long-distance quantum communication with atomic ensembles and linear optics," *Nature* **414**, 413 (2001).

[42] A. Einstein, B. Podolsky, and N. Rosen, "Can quantum-mechanical description of physical reality be considered complete?" *Phys. Rev.* **47**, 777 (1935).

[43] M. D. Eisaman, A. André, F. Massou, M. Fleischhauer, A. S. Zibrov, and M. D. Lukin, "Electromagnetically induced transparency with tunable single-photon pulses," *Nature* **438**, 837 (2005).

[44] A. K. Ekert, "Quantum cryptography based on bell's theorem," *Phys. Rev. Lett.* **67**, 661 (1991).

[45] D. Felinto, C. W. Chou, J. Laurat, E. W. Schomburg, H. de Riedmatten, and H. J. Kimble, "Conditional control of the quantum states of remote atomic memories for quantum networking," *Nature Physics* **2**, 844 (2006).

[46] Richard P. Feynman, "Simulating physics with computers," *International Journal of Theoretical Physics* **21**, 467 (1982).

[47] D. P. Fussell, R. C. McPhedran, and C. Martijn de Sterke, "Three-dimensional Green's tensor, local density of states, and spontaneous emission in finite two-dimensional photonic crystals composed of cylinders," *Phys. Rev. E* **70**, 066608 (2004).

[48] U. Gaubatz, P. Rudecki, S. Schiemann, and K. Bergmann, "Population transfer between molecular vibrational levels by stimulated raman scattering with partially overlapping laser fields. a new concept and experimental results," *The Journal of Chemical Physics* **92**, 5363 (1990).

[49] T. Gerrits, S. Glancy, T. S. Clement, B. Calkins, A. E. Lita, A. J. Miller, A. L. Migdall, S. W. Nam, R. P. Mirin, and E. Knill, "Generation of optical Schrödinger cat states by number-resolved photon subtraction from squeezed vacuum," *arXiv* **quant-ph**, 1004.2727 (2010).

[50] T. Gerrits, S. C. Glancy, T. S. Clement, B. Calkins, A. Lita, A. J. Miller, Migdall, A. L., S.W. Nam, R. Mirin, and E. Knill, "Generation of optical Schrodinger cat states by number-resolved squeezed photon subtraction," in "Proceedings from Conference of Lasers and Electro-optics (CLEO) and International Quantum Electronics Conference (IQEC)," (2009).

[51] C. C. Gerry, "Generation of optical macroscopic quantum superposition states via state reduction with a mach-zehnder interferometer containing a kerr medium," *Phys. Rev. A* **59**, 4095 (1999).

[52] C. C. Gerry and P. L. Knight, *Introductory Quantum Optics* (Cambridge University Press, 2005).

[53] N. Gisin, G. Ribordy, W. Tittel, and H. Zbinden, "Quantum cryptography," *Rev. Mod. Phys.* **74**, 145 (2002).

[54] S. Glancy and H. M. de Vasconcelos, "Methods for producing optical coherent state superpositions," *J. Opt. Soc. Am. B* **25**, 712 (2008).

[55] R. J. Glauber, "Coherent and incoherent states of the radiation field," *Phys. Rev.* **131**, 2766 (1963).

[56] A. V. Gorshkov, A. André, M. Fleischhauer, A. S. Sørensen, and M. D. Lukin, "Universal approach to optimal photon storage in atomic media," *Phys. Rev. Lett.* **98**, 123601 (2007).

[57] A. V. Gorshkov, A. André, M. D. Lukin, and A. S. Sørensen, "Photon storage in lambda-type optically dense atomic media. II. Free-space model," *Phys. Rev. A* **76**, 033805 (2007).

[58] A. V. Gorshkov, A. M. Rey, A. J. Daley, M. M. Boyd, J. Ye, P. Zoller, and M. D. Lukin, "Alkaline-earth-metal atoms as few-qubit quantum registers," *Physical Review Letters* **102**, 110503 (2009).

[59] Lov K. Grover, "A fast quantum mechanical algorithm for database search," in "STOC '96: Proceedings of the 28th annual ACM symposium on Theory of computing," (ACM, New York, NY, USA, 1996), pp. 212–219.

[60] R. H. Hadfield, "Single-photon detectors for optical quantum information applications," *Nature Photonics* **3**, 696 (2009).

[61] K. Hammerer, M. Wallquist, C. Genes, M. Ludwig, F. Marquardt, P. Treutlein, P. Zoller, J. Ye, and H. J. Kimble, "Strong coupling of a mechanical oscillator and a single atom," *Phys. Rev. Lett.* **103**, 063005 (2009).

[62] K. Hammerer, M. M. Wolf, E. S. Polzik, and J. I. Cirac, "Quantum benchmark for storage and transmission of coherent states," *Phys. Rev. Lett.* **94**, 150503 (2005).

[63] Klemens Hammerer, Anders S. Sørensen, and Eugene S. Polzik, "Quantum interface between light and atomic ensembles," *Rev. Mod. Phys.* **82**, 1041 (2010).

[64] L. Hartmann, B. Kraus, H.-J. Briegel, and W. Dür, "Role of memory errors in quantum repeaters," *Phys. Rev. A* **75**, 032310 (2007).

[65] D. Hayes, P. S. Julienne, and I. H. Deutsch, "Quantum logic via the exchange blockade in ultracold collisions," *Phys. Rev. Lett.* **98**, 070501 (2007).

[66] T. Holstein and H. Primakoff, "Field dependence of the intrinsic domain magnetization of a ferromagnet," *Phys. Rev.* **58**, 1098 (1940).

[67] J. P. Home, D. Hanneke, J. D. Jost, J. M. Amini, D. Leibfried, and D. J. Wineland, "Complete methods set for scalable ion trap quantum information processing," *Science* **325**, 1227 (2009).

[68] A. Imamoglu, "High efficiency photon counting using stored light," *Phys. Rev. Lett.* **89**, 163602 (2002).

[69] D. Jaksch, H.-J. Briegel, J. I. Cirac, C. W. Gardiner, and P. Zoller, "Entanglement of atoms via cold controlled collisions," *Phys. Rev. Lett.* **82**, 1975 (1999).

[70] D. F. V. James and P. G. Kwiat, "Atomic-vapor-based high efficiency optical detectors with photon number resolution," *Phys. Rev. Lett.* **89**, 183601 (2002).

[71] H. Jeong, W. Son, M. S. Kim, D. Ahn, and Č. Brukner, "Quantum nonlocality test for continuous-variable states with dichotomic observables," *Phys. Rev. A* **67**, 012106 (2003).

[72] L. Jiang, J. M. Taylor, and M. D. Lukin, "Fast and robust approach to long-distance quantum communication with atomic ensembles," *Phys. Rev. A* **76**, 012301 (2007).

[73] Liang Jiang, J. M. Taylor, Kae Nemoto, W. J. Munro, Rodney Van Meter, and M. D. Lukin, "Quantum repeater with encoding," *Phys. Rev. A* **79**, 032325 (2009).

[74] B. Julsgaard, J. Sherson, J. I. Cirac, J. Fiurášek, and E. S. Polzik, "Experimental demonstration of quantum memory for light," *Nature* **432**, 482 (2004).

[75] E. Knill, R. Laflamme, and G. J. Milburn, "A scheme for efficient quantum computation with linear optics," *Nature* **409**, 46 (2001).

[76] P. Kok, W. J. Munro, K. Nemoto, T. C. Ralph, J.P. Dowling, and G. J. Milburn, "Linear optical quantum computing with photonic qubits," *Rev. Mod. Phys.* **79**, 135 (2007).

[77] A. Kuzmich, W. P. Bowen, A. D. Boozer, A. Boca, C. W. Chou, L.-M. Duan, and H. J. Kimble, "Generation of nonclassical photon pairs for scalable quantum communication with atomic ensembles," *Nature* **423**, 731 (2003).

[78] J. Laurat, C. w. Chou, H. Deng, K. S. Choi andD. Felinto, H. de Riedmatten, and H. J. Kimble, "Towards experimental entanglement connection with atomic ensembles in the single excitation regime," *New Journal of Physics* **9**, 207 (2007).

[79] P. J. Lee, M. Anderlini, B. L. Brown, J. Sebby-Strabley, W. D. Phillips, and J. V. Porto, "Sublattice addressing and spin-dependent motion of atoms in a double-well lattice," *Phys. Rev. Lett.* **99**, 020402 (2007).

[80] I. D. Leroux, M. H. Schleier-Smith, and V. Vuletić, "Implementation of cavity squeezing of a collective atomic spin," *Phys. Rev. Lett.* **104**, 073602 (2010).

[81] Seth Lloyd, "Universal quantum simulators," *Science* **273**, 1073 (1996).

[82] A. P. Lund, H. Jeong, T. C. Ralph, and M. S. Kim, "Conditional production of superpositions of coherent states with inefficient photon detection," *Phys. Rev. A* **70**, 020101 (2004).

[83] A. P. Lund, T. C. Ralph, and H. L. Haselgrove, "Fault-tolerant linear optical quantum computing with small-amplitude coherent states," *Phys. Rev. Lett.* **100**, 030503 (2008).

[84] N. Lütkenhaus, J. Calsamiglia, and K.-A. Suominen, "Bell measurements for teleportation," *Phys. Rev. A* **59**, 3295 (1999).

[85] O. Mandel, M. Greiner, A. Widera, T. Rom, T. W. Hänsch, and I. Bloch, "Coherent transport of neutral atoms in spin-dependent optical lattice potentials," *Phys. Rev. Lett.* **91**, 010407 (2003).

[86] S. Massar and S. Popescu, "Optimal extraction of information from finite quantum ensembles," *Phys. Rev. Lett.* **74**, 1259 (1995).

[87] M. Mehmet, H. Vahlbruch, N. Lastzka, K. Danzmann, and R. Schnabel, "Observation of squeezed states with strong photon-number oscillations," *Phys. Rev. A* **81**, 013814 (2010).

[88] S. T. Merkel, P. S. Jessen, and I. H. Deutsch, "Quantum control of the hyperfine-coupled electron and nuclear spins in alkali-metal atoms," *Phys. Rev. A* **78**, 023404 (2008).

[89] J. Minář, H. de Riedmatten, C. Simon, H. Zbinden, and N. Gisin, "Phase-noise measurements in long-fiber interferometers for quantum-repeater applications," *Phys. Rev. A* **77**, 052325 (2008).

[90] D. L. Moehring, P. Maunz, S. Olmschenk, K. C. Younge, D. N. Matsukevich, L.-M. Duan, and C. Monroe, "Entanglement of single-atom quantum bits at a distance," *Nature* **449**, 68 (2007).

[91] R. Morris, "The dilogarithm function of a real argument," *Math. Comp.* **33**, 778 (1979).

[92] W. J. Munro, K. Nemoto, G. J. Milburn, and S. L. Braunstein, "Weak-force detection with superposed coherent states," *Phys. Rev. A* **66**, 023819 (2002).

[93] C. A. Muschik, K. Hammerer, E. S. Polzik, and J. I. Cirac, "Efficient quantum memory and entanglement between light and an atomic ensemble using magnetic fields," *Phys. Rev. A* **73**, 062329 (2006).

[94] Christine Muschik, private communication (2006).

[95] A. H. Myerson, D. J. Szwer, S. C. Webster, D. T. C. Allcock, M. J. Curtis, G. Imreh, J. A. Sherman, D. N. Stacey, A. M. Steane, and D. M. Lucas, "High-fidelity readout of trapped-ion qubits," *Phys. Rev. Lett.* **100**, 200502 (2008).

[96] J. S. Neergaard-Nielsen, B. Melholt Nielsen, C. Hettich, K. Mølmer, and E. S. Polzik, "Generation of a superposition of odd photon number states for quantum information networks," *Phys. Rev. Lett.* **97**, 083604 (2006).

[97] Jonas Schou Neergaard-Nielsen, *Generation of single photons and Schrödinger kitten states of light*, Ph.D. thesis, Niels Bohr Institute, University of Copenhagen (2008).

[98] M. A. Nielsen and I. L. Chuang, *Quantum Computation and Quantum Information* (Cambridge University Press, 2000).

[99] Z. Y. Ou and L. Mandel, "Violation of bell's inequality and classical probability in a two-photon correlation experiment," *Phys. Rev. Lett.* **61**, 50 (1988).

[100] A. Ourjoumtsev, F. Ferreyrol, R. Tualle-Brouri, and P. Grangier, "Preparation of non-local superpositions of quasi-classical light states," *Nature Physics* **5**, 189 (2009).

[101] A. Ourjoumtsev, H. Jeong, R. Tualle-Brouri, and P. Grangier, "Generation of optical 'Schrodinger cats' from photon number states," *Nature* **448**, 784 (2007).

[102] Alexei Ourjoumtsev, Rosa Tualle-Brouri, Julien Laurat, and Philippe Grangier, "Generating optical schrodinger kittens for quantum information processing," *Science* **312**, 83 (2006).

[103] Ho Ngoc Phien and Nguyen Ba An, "Quantum teleportation of an arbitrary two-mode coherent state using only linear optics elements," *Physics Letters A* **372**, 2825 (2008).

[104] S. G. Porsev, A. D. Ludlow, M. M. Boyd, and J. Ye, "Determination of sr properties for a high-accuracy optical clock," *Physical Review A (Atomic, Molecular, and Optical Physics)* **78**, 032508 (2008).

[105] J. Pottage, David Bird, T. Hedley, J. Knight, T. Birks, P. Russell, and P. Roberts, "Robust photonic band gaps for hollow core guidance in pcf made from high index glass," *Opt. Express* **11**, 2854 (2003).

[106] A. A. Radzig and B. M. Smirnov, *Reference data on atoms, molecules and ions* (Springer-Verlag, 1985).

[107] T. C. Ralph, A. Gilchrist, G. J. Milburn, W. J. Munro, and S. Glancy, "Quantum computation with optical coherent states," *Phys. Rev. A* **68**, 042319 (2003).

[108] P. St.J. Russell, "Photonic-crystal fibers," *IEEE/OSA Journal of Lightwave Technology* **24**, 4729 (2006).

[109] J. J. Sakurai, *Modern Quantum Mechanics* (Addison-Wesley, 1994), revised edn.

[110] N. Sangouard, R. Dubessy, and C. Simon, "Quantum repeaters based on single trapped ions," *arXiv* **quant-ph**, 0902.3127v1 (2009).

[111] N. Sangouard, C. Simon, H. de Riedmatten, and N. Gisin, "Quantum repeaters based on atomic ensembles and linear optics," *arXiv* **quant-ph**, 0902.2699v2 (2009).

[112] N. Sangouard, C. Simon, N. Gisin, J. Laurat, R. Tualle-Brouri, and P. Grangier, "Quantum repeaters with entangled coherent states," *arXiv* **quant-ph**, 0912.3871v1 (2009).

[113] N. Sangouard, C. Simon, J. Minář, H. Zbinden, H. de Riedmatten, and N. Gisin, "Long-distance entanglement distribution with single-photon sources," *Phys. Rev. A* **76**, 050301 (2007).

[114] N. Sangouard, C. Simon, B. Zhao, Y.-A. Chen, H. de Riedmatten, J.-W. Pan, and N. Gisin, "Robust and efficient quantum repeaters with atomic ensembles and linear optics," *Phys. Rev. A* **77**, 062301 (2008).

[115] R. Santra, E. Arimondo, T. Ido, C. H. Greene, and J. Ye, "High-accuracy optical clock via three-level coherence in neutral bosonic [sup 88]sr," *Physical Review Letters* **94**, 173002 (2005).

[116] E. Schrödinger, "Die gegenwärtige situation in der quantenmechanik," *Naturwissenschaften* **23**, 807, 823, and 844 (1935).

[117] J. F. Sherson, Krauter H., R. K. Olsson, B. Julsgaard, K. Hammerer, I. Cirac, and E. S. Polzik, "Quantum teleportation between light and matter," *Nature* **443**, 557 (2006).

[118] P. W. Shor, "Algorithms for quantum computation: discrete logarithms and factoring," in "SFCS '94: Proceedings of the 35th Annual Symposium on Foundations of Computer Science," (IEEE Computer Society, Washington, DC, USA, 1994), pp. 124–134.

[119] C. Simon, H. de Riedmatten, M. Afzelius, N. Sangouard, H. Zbinden, and N. Gisin, "Quantum repeaters with photon pair sources and multimode memories," *Phys. Rev. Lett.* **98**, 190503 (2007).

[120] C. Simon, Y.-M. Niquet, X. Caillet, J. Eymery, J.-P. Poizat, and J.-M. Gérard, "Quantum communication with quantum dot spins," *Phys. Rev. B* **75**, 081302 (2007).

[121] M. W. Sørensen and A. S. Sørensen, "Three-dimensional theory for light-matter interaction," *Phys. Rev. A* **77**, 013826 (2008).

[122] D. A. Steck, "Cesium D line data," Tech. Rep. revision 2.1, University of Oregon (2008), URL `http://steck.us/alkalidata`.

[123] D. A. Steck, "Rubidium 87 D line data," Tech. Rep. revision 2.1, University of Oregon (2008), URL `http://steck.us/alkalidata`.

[124] M. Stobińska, H. Jeong, and T. C. Ralph, "Violation of Bell's inequality using classical measurements and nonlinear local operations," *Phys. Rev. A* **75**, 052105 (2007).

[125] R. Stock, N. S. Babcock, M. G. Raizen, and B. C. Sanders, "Entanglement of group-ii-like atoms with fast measurement for quantum information processing," *Phys. Rev. A* **78**, 022301 (2008).

[126] H. Takahashi, K. Wakui, S. Suzuki, M. Takeoka, K. Hayasaka, A. Furusawa, and M. Sasaki, "Generation of large-amplitude coherent-state superposition via ancilla-assisted photon subtraction," *Physical Review Letters* **101**, 233605 (2008).

[127] T. Takano, M. Fuyama, R. Namiki, and Y. Takahashi, "Spin squeezing of a cold atomic ensemble with the nuclear spin of one-half," *Phys. Rev. Lett.* **102**, 033601 (2009).

[128] Y. Takeno, M. Yukawa, H. Yonezawa, and A. Furusawa, "Observation of -9 dB quadrature squeezing with improvement of phasestability in homodyne measurement," *Opt. Express* **15**, 4321 (2007).

[129] M. Takeoka and M. Sasaki, "Conditional generation of an arbitrary superposition of coherent states," *Phys. Rev. A* **75**, 064302 (2007).

[130] I. Teper, G. Vrijsen, J. Lee, and M. A. Kasevich, "Backaction noise produced via cavity-aided nondemolition measurement of an atomic clock state," *Phys. Rev. A* **78**, 051803 (2008).

[131] James K. Thompson, Jonathan Simon, Huanqian Loh, and Vladan Vuletic, "A high-brightness source of narrowband, identical-photon pairs," *Science* **313**, 74 (2006).

[132] W. Tittel, J. Brendel, H. Zbinden, and N. Gisin, "Violation of Bell inequalities by photons more than 10 km apart," *Phys. Rev. Lett.* **81**, 3563 (1998).

[133] C. H. van der Wal, M. D. Eisaman, A. Andre, R. L. Walsworth, D. F. Phillips, A. S. Zibrov, and M. D. Lukin, "Atomic memory for correlated photon states," *Science* **301**, 196 (2003).

[134] S. J. van Enk and O. Hirota, "Entangled coherent states: Teleportation and decoherence," *Phys. Rev. A* **64**, 022313 (2001).

[135] P. van Loock, T. D. Ladd, K. Sanaka, F. Yamaguchi, Kae Nemoto, W. J. Munro, and Y. Yamamoto, "Hybrid quantum repeater using bright coherent light," *Phys. Rev. Lett.* **96**, 240501 (2006).

[136] P. van Loock and N. Lütkenhaus, "Simple criteria for the implementation of projective measurements with linear optics," *Phys. Rev. A* **69**, 012302 (2004).

[137] G. Weihs, T. Jennewein, C. Simon, H. Weinfurter, and A. Zeilinger, "Violation of Bell's inequality under strict Einstein locality conditions," *Phys. Rev. Lett.* **81**, 5039 (1998).

[138] G. Woan, *The Cambridge Handbook of Physics Formulas* (Cambridge University Press, 2000).

[139] W. K. Wootters and W. H. Zurek, "A single quantum cannot be cloned," *Nature* **299**, 802 (1982).

[140] X. Xu, T. H. Loftus, J. L. Hall, A. Gallagher, and J. Ye, "Cooling and trapping of atomic strontium," *J. Opt. Soc. Am. B* **20**, 968 (2003).

[141] M. Yasuda and H. Katori, "Lifetime measurement of the $^3P_2$ metastable state of strontium atoms," *Phys. Rev. Lett.* **92**, 153004 (2004).

[142] Z.-S. Yuan, Y.-A. Chen, S. Chen, B. Zhao, M. Koch, T. Strassel, Y. Zhao, G.-J. Zhu, J. Schmiedmayer, and J.-W. Pan, "Synchronized independent narrow-band single photons and efficient generation of photonic entanglement," *Phys. Rev. Lett.* **98**, 180503 (2007).

[143] Z.-S. Yuan, Y.-A. Chen, B. Zhao, S. Chen, J. Schmiedmayer, and J.-W. Pan, "Experimental demonstration of a BDCZ quantum repeater node," *Nature* **454**, 1098 (2008).

[144] B. Yurke and D. Stoler, "Generating quantum mechanical superpositions of macroscopically distinguishable states via amplitude dispersion," *Phys. Rev. Lett.* **57**, 13 (1986).

[145] B. Zhao, Z.-B. Chen, Y.-A. Chen, J. Schmiedmayer, and J.-W. Pan, "Robust creation of entanglement between remote memory qubits," *Phys. Rev. Lett.* **98**, 240502 (2007).

[146] M. Żukowski, A. Zeilinger, M. A. Horne, and A. K. Ekert, "'event-ready-detectors' bell experiment via entanglement swapping," *Phys. Rev. Lett.* **71**, 4287 (1993).